The Dissertation Committee for Songyang Tong
Certifies that this is the approved version of the following dissertation:

Improvement of Fracture Conductivity through Study of Proppant Transport and Chemical Stimulation

Committee:

Kishore K. Mohanty, Supervisor

David DiCarlo

Mukul M. Sharma

Kamy Sepehrnoori

Charles Werth

Improvement of Fracture Conductivity through Study of Proppant Transport and Chemical Stimulation

by

Songyang Tong

Dissertation

Presented to the Faculty of the Graduate School of

The University of Texas at Austin

in Partial Fulfillment

of the Requirements

for the Degree of

Doctor of Philosophy

The University of Texas at Austin

May 2019

Dedication

Dedicated to my supportive parents and wife

Acknowledgements

I would like to acknowledge and express my deep gratitude to Dr. Kishore Mohanty for his constant support and guidance throughout my Ph.D. research. Besides the knowledge and skills I gained from him, his integrity, humbleness and caring for others all inspired me and would guide me through my future endeavors. It was a great honor for me to have him as my Ph.D. advisor. In addition, I would like to thank my committee members: Dr. DiCarlo, Dr. Sharma, Dr. Sepehrnoori and Dr. Werth for spending their time to evaluate my work and provide insightful and constructive feedback, which significantly improved the quality of my dissertation.

My greatest appreciation for my parents who always encouraged and supported me. I am grateful to my mom and dad for their relentless prayers for my well-being. I owe a great debt of gratitude to my wife, Jiaying for her love and support. Her sacrifice, companion and caring nature helped me to conquer all the difficulties. Thank you, Jiaying, and I am extremely fortunate to have you as my wife!

I also would like to thank the department staff at UT PGE, especially Daryl Nygaard for his exceptional skills and responsive attitude, Glen Baum, Gary Miscoe and Amy Stewart. In addition, I highly appreciate Barbara Messmore for her administrative support to our research group.

Many thanks to my friends Yifei Xu, Pengpeng Qi, Hongtao Yang, Ke Xu, Runqi Han, Zhuang Sun and Peng Zhang. I would also like to express my gratitude to my group fellows in Dr. Mohanty's research group for their help, guidance and research collaborations, especially Ming, Peila, Robin, Shashvat, Himanshu, Pinaki, Bochao, Tongzhou, Eric, Krishna, and Chammi.

Finally, I would like to acknowledge the Statoil Doctoral Fellowship (2014-2017) which financially supported me throughout most of my Ph.D. study.

Abstract

Improvement of Fracture Conductivity through Study of Proppant Transport and Chemical Stimulation

Songyang Tong, PhD

The University of Texas at Austin, 2019

Supervisor: Kishore Mohanty

During hydraulic fracturing treatments, proppants – usually sand – are placed inside fractures to improve fracture conductivity. However, a large portion of the generated hydraulic fractures often remain unpropped after fracturing treatments. There are two primary reasons for this poor proppant placement. First, proppants settle quickly in common fracturing fluids (e.g., slickwater), which results in unpropped sections at the tip or top of the fracture. Second, a large number of the microfractures are too narrow to accommodate any common commercial proppant. Such unpropped fractures hold a large potential flow capacity as they exhibit a large contact area with the reservoir. However, their potential flow capacity is diminished during production due to closing of unpropped fractures because of closure stress.

In this study, fractures are categorized as wider fractures, which are accessible to proppant, and narrower fractures, which are inaccessible to proppant. For wider fractures, proppant transport is important as proppant is needed for keeping them open. For narrower fractures, a chemical formulation is proposed as there is less physical restriction for fluids

to flow inside across them. The chemical formulation is expected to improve fracture conductivity by generating roughness on fracture surfaces.

This dissertation uses experiments and simulations to investigate proppant transport in a complex fracture network with laboratory-scale transparent fracture slots. Proppant size, injection flow rate and bypass fracture angle are varied and their effects are systematically evaluated. Based on experimental results, a straight-line relationship can be used to quantify the fraction of proppant that flows into bypass fractures with the total amount of proppant injected. A Computational Fluid Dynamics (CFD) model is developed to simulate the experiments; both qualitative and quantitative matches are achieved with this model. It is concluded that the fraction of proppant which flows into bypass fractures could be small unless a significant amount of proppant is injected, which indicates the inefficiency of slickwater in transporting proppant.

An alternative fracturing fluid – foam – has been proposed to improve proppant placement because of its proppant carrying capacity. Foam is not a single-phase fluid, and it suffers liquid drainage with time due to gravity. Additionally, the existence of foam bubbles and lamellae could alter the movement of proppants. Experiments and simulations are performed to evaluate proppant placement in field-scale foam fracturing application. A liquid drainage model and a proppant settling correlation are developed and incorporated into an in-housing fracturing simulator. Results indicate that liquid drainage could negatively affect proppant placement, while dry foams could lead to negligible proppant settling and consequently uniform proppant placement.

For narrower fractures, two chemical stimulation techniques are proposed to improve fracture conductivity by increasing fracture surface roughness. The first is a nanoparticle-microencapsulated acid (MEA) system for shale acidizing applications, and the second is a new technology which can generate mineral crystals on the shale surface to

act as in-situ proppants. The MEA could be released as the fracture closes and the released acid could etch the surface of the rock locally, in a non-uniform way, to improve fracture conductivity (up to 40 times). Furthermore, the in-situ proppant generation technology can lead to crystal growth in both fracking water and formation brine conditions, and it also improves fracture conductivity (up to 10 times) based on core flooding experiments.

Table of Contents

List of Tables

List of Figures

Chapter 1: Introduction

1.1 Background and Motivation

US domestic production has witnessed a significant growth thanks to the shale revolution. The success of hydrocarbon production from unconventional shale can be attributed primarily to the combination of horizontal drilling and hydraulic fracturing stimulations. Hydraulic fracturing is a technique to generate highly conductive conduits and enhanced stimulated reservoir volume (SRV) by cracking the formation with a pressurized fluid mixed with proppants. Proppants (usually sands) are solid particles preventing the created fractures from closing as the effective closure stress increases during production. Additionally, the short-cycle investment nature of shale wells has been proved to be competitive in a low crude price environment, and it has dramatically transformed the oil and gas industry.

A typical hydraulic fracturing treatment consists of the following steps. (1) An initial fluid injection without any proppant (pad) is pumped to generate the fracture. (2) A proppant-laden fluid is pumped downhole to finish the main stage of the treatment. (3) Finally, a tail-flush without proppant is followed to complete the fracturing job. The function of the tail-flush is to push remaining proppant-slurry in the near wellbore region into the fracture. Generally, a primary hydraulic fracture, which intersects various types of secondary fractures, is generated. Proppants could remain inside the fractures and support the aperture and conductivity of the fractures. The formation of such a fracture network can significantly increase the contact area and lead to better SRV. The commonly used

fracturing fluids are either gelled fluids, which favor wider but shorter fractures, or slickwater fluids, which promote longer but narrower fractures (Biot et al., 1986). For shale reservoirs, the most desirable fracture geometry is long and skinny in shape. Thus, slickwater gained lots of popularity because it can generate a large SRV at a relatively lower cost (Warpinski et al., 2009). In addition, benefits like simple facilities and low gel residues are also favorable in field operations. However, because of its lower viscosity, conventional proppants settle down fast to the bottom of the propagating fracture and lead to poor proppant placement.

Fractures could be categorized as either propped or unpropped. Fractures filled with proppants are considered to be propped fractures. Closed fractures without any proppants are considered unpropped fractures. Fractures remain unpropped either because they are too narrow to accommodate any proppants (less than 200 μm), or because the proppants cannot be effectively placed inside the fractures due to poor proppant transport.

During production, the fluid pressure inside the fracture network decreases gradually, which leads to fracture closure because of increasing effective closure stress imposed on the fractures. The closure stress is usually several thousand psi at reservoir conditions, and fracture conductivity loss is expected during production. The existence of proppant inside fractures could significantly prevent conductivity reduction. Thus propped fractures act as conductive pathways for hydrocarbon to flow from the reservoir to the wellbore. Conductivity of propped fracture has been widely investigated in the literature (Palisch et al., 2007; Zhang et al., 2014), and its conductivity is reported to have a wide range between 10 to 1000 mdft under elevated closure stress.

However, even fractures with proppants, a large portion of fractured surface at the top of the fracture could be unpropped because of the severe settling of proppants (Kern et al., 1959). Proppants tend to settle in the near wellbore region and form a proppant bed at the bottom of the fracture. At the top of the fracture, a clear fluid zone is formed and this zone could lead to an unpropped zone when the fracturing treatment stops. This distribution is also reported as proppant arch (Warpinski, 2009) by some researchers. Additionally, proppants have difficulty entering natural fractures and induced micro-fractures generated during the shear or tensile failure of the rock, which leads to a different type of unpropped fractures during fracturing treatments.

In order to maximize the benefits of fracturing jobs, an optimal utilization of the fractured surface is important. For fractures having wider apertures, it is important to understand vertical proppant transport inside large fractures. Extensive research study have been reported on proppant transport within a single fracture (Blyton et al., 2015; Liu and Sharma, 2005; Patankar et al., 2002; Shiozawa and McClure, 2016; Woodworth and Miskimins, 2007). Transparent Hele-Shaw slot have been widely used to visualize and investigate proppant transport in lab experiments (Liu and Sharma, 2005; Malhotra et al., 2014; Malhotra and Sharma, 2012; Sahai et al., 2014; Zhou et al., 2015). A Hele-Shaw slot provides two primary benefits: (1) Simplicity of the system and (2) Convenience of observation and tracking of proppant movement. However, it also has some limitations including: (1) Elevated pressure is not easy to achieve. (2) Fracture geometry is pre-defined, which means dynamic fracture propagation and leak-off effects are ignored. (3) Scale of the slot is much smaller than that of the fracture in field conditions.

Recently, proppant transport in slickwater within a complex Hele-Shaw slot has been investigated (Li et al., 2017; Sahai et al., 2014). Low viscosity fracturing fluids cannot suspend proppants very well, which could lead to poor proppant placement and partial utilization of created fractures. This less favorable proppant distribution would lead to a large portion of fracture surfaces and network unpropped or sealed after stimulation (Warpinski, 2009). Usually, viscous fracturing fluid is used to slow down proppant settling to achieve better proppant placements. There are usually two methods to viscosify the fracturing fluid. The first approach is to add polymers, such as guar gum, to form liner or crosslinked gel fluid. These gelled fluids could offer viscosities ranging from 10 to 1000 cp based on the polymer concentration and crosslink state (Barati and Liang, 2014). However, due to the ultra-low permeability of shale rocks, a polymer filter-cake can build up on the fracture surface because of fracturing fluid leak-off (Xu et al., 2011). This filter-cake could plug the pore spaces and adversely affect production. The second approach is to use foam fluids (Faroughi et al., 2018; Gu and Mohanty, 2014; Harris, 1989; Ribeiro and Sharma, 2013). Foam is a mixture of gas and liquid, and the typical foam quality (gas volume fraction) applied in field fracturing treatment is within the range of 70% to 85%. Theoretically, a cellular bubble structure is formed when foam quality is beyond the threshold value of 64%, which comes from the closely pack of monomodal bubbles in a hexagonal structure (Faroughi et al., 2018). This cellular structure promises outstanding proppant carry capacity because of both viscous and elastic forces (Jing et al., 2016). Foam fluid also provides additional benefits over slickwater: less water usage, reduced water blockage, better leak-off control, and fast clean-up efficiency. However, the requirements

of stronger pumping system, sophisticated facilities and gas logistics all add cost to the application of foam (Wanniarachchi et al., 2015).

For fractures having narrower apertures which remained unpropped after hydraulic fracturing, a chemical technique is usually used. For example, acidizing is widely used for well stimulation in conventional carbonate reservoirs because it creates wormholes and increases the productivity index of wells (Daccord et al., 1989; Wei et al., 2017). Recently, the feasibility of acid stimulation in shale formations has been investigated (Tripathi and Pournik, 2014; Wu and Sharma, 2017a). In the presence of calcite and mineral heterogeneity, acid can etch fracture surfaces unevenly to create surface roughness (Wu and Sharma, 2017b), which is supposed to enhance the conductivity of unpropped fractures. However, the so-called uneven surface etching is tricky and unoptimized acidizing could be detrimental. Since the strength and integrity of some shales largely depends on the calcite framework, surface etching can lead to rock softening with excessive mud generation, which could lead to severe conductivity loss (Tripathi and Pournik, 2014). Recently, injecting polymer based solutions into fractures to form polymeric particles as in-situ proppants has been proposed (Chang et al., 2015). However, polymer-based particles could be too deformable to prop the fractures at the reservoir conditions.

1.2 Objective and Methodology

The main goal of this dissertation is to enhance the utilization of fractured surface through optimizing proppant transport and enhanced fracture conductivity of unpropped fracture by chemical stimulation.

The proppant transport study focuses on two aspects: (1) proppant transport from a primary fracture into an intersecting secondary fracture, (2) proppant transport in foam based fracturing fluid. A lab scale Hele-Shaw slot is used to visualize and track the movement of proppants. For the slickwater cases, a Computational Fluid Dynamic (CFD) model has been established to match the lab results. For foam fluid cases, because of the existence of foam bubbles and foam drainage effects (Weaire et al., 2007), treating foam as a single-phase fluid is no longer valid (Tong et al., 2018). Therefore, an empirical proppant settling correlation and a foam drainage model are developed and incorporated into a field scale fracturing simulator to evaluate the performance of foam fracturing.

The chemical stimulation study focuses on two aspects: (1) nanoparticle-encapsulated acids for shale acidizing application. (2) in-situ proppant generation through a hydro-thermal reaction. For the encapsulated acid, the objective is to evaluate its effect on the conductivity of fractured shale core samples. For the in-situ proppant generation study, the objective is to investigate the feasibility of forming hydroxyapatite crystals to act as proppants to maintain fracture conductivity.

1.3 Outline of Dissertation

Chapter 1 introduces the background and motivation, the objective and methodology, and the structure of the discussion.

Chapter 2 focuses on the experimental study of proppant transport from a primary fracture into a secondary fracture. This study is first-of-its-kind to quantify the amount of proppant that flow into a secondary fracture from a primary fracture. Parameters including proppant size, injection rate and secondary fracture angle have been studied

systematically. A linear relationship is observed which predicts that the more the proppant injected, the larger the ratio of proppant would flow into secondary fractures.

Chapter 3 focuses on the study of visualizing proppant transport in foam fluid. Foam is usually simplified as a single-phase fluid in fracturing studies, and proppant settling velocity is typically calculated with the effective viscosity of foam. However, due to the existence of foam bubbles and foam drainage process, proppant settling in foam fluid is much more complex. In this study, dynamic proppant settling velocity in foam was measured for the first time, and several interesting flow behaviors were also observed and discussed. This study clearly shows that the internal microstructure of foam could significantly alter the movement of proppant.

Chapter 4 focuses on the development of a Computational Fluid Dynamics (CFD) model for simulating the lab results in chapter 2. The model is called Dense Discrete Phase Modelling (DDPM). It groups multiple particles(proppants) into a single parcel to save computation time, and then applied the Kinetic Theory of Granular Flow (KTGF) to account for the particle-particle interactions. The simulation of proppant transport from a primary fracture into a secondary fracture has been rarely investigated before this study, and this model is also the first-of-its-kind to successfully match lab results in such a fracture geometry.

Chapter 5 focuses on the development of a foam drainage model and a proppant settling correlation in foam based on lab results in chapter 3. This study is first-of-its-kind to consider foam as a two-phase fluid. The proppant settling velocity in foam was found to have no direct relationship with foam effective viscosity. Instead foam drainage could significantly alter the proppant placement. These two modules were then incorporated into an in-house fracturing modelling to evaluate proppant placement in field-scale.

Chapter 6 focuses on the evaluation of chemical stimulation techniques to utilize microfractures which are too narrow to accommodate any proppants. Two approaches are proposed: nanoparticle-encapsulated acids and in-situ proppant generation. Shale acidizing is expected to generate uneven fracture surface etching for improved fracture conductivity. However, aqueous acid could cause shale softening and excess mud generation with loss of fracture conductivity. Encapsulated acids can unevenly release the acids to successfully generate rough surface etching. In-situ proppant generation through a hydro-thermal reaction is first proposed in this study, and this reaction has been widely investigated in medical research for human bone substitution material generation. Both batch reaction and reactive flow experiments have been conducted, and proppant-size crystals and improved fracture conductivity were observed in the lab study.

Chapter 7 summarizes major conclusions and contributions from this dissertation and provides recommendations for future work.

Chapter 2: Experimental Study of Proppant Transport in Fractures with Intersections

2.1 SUMMARY

For naturally fractured reservoirs, the presence of secondary fractures increases the possibility of generating complex fracture networks. The investigation of proppant transport in these complex systems is still limited, and the efficiency of proppant placement into these subsidiary fractures is poorly understood.

The purpose of chapter 2 is to experimentally evaluate and quantify proppant transport in complex fracture systems at ambient condition. A series lab scale fracture slots with a bypass slot intersecting at the center of the main slot were build. Different proppant size, bypass slot angle and injection rate were systematically investigated.

Our results show that a straight-line relationship could be used to quantify the fraction of proppant that flows into secondary fractures with the total amount of proppant injected. In addition, this relationship indicates that the more the proppant injected, the larger the fraction of proppant would occupy the secondary fractures. However, at the junction of primary fracture and secondary fractures, severe proppant settling is expected because of the slowdown of fluid velocity. Therefore, slickwater slurry system cannot lead to optimal proppant placement.

This chapter is based on (Tong and Mohanty, 2016). Dr. Mohanty supervised the project.
Tong, S., Mohanty, K.K., 2016. Proppant transport study in fractures with intersections. Fuel 181, 463–477

2.2 INTRODUCTION

Due to the existence of natural fractures and weak planes in shale formations, the hydraulically induced primary fractures can intersect with these secondary fractures to create a complex fracture network (Gale et al., 2014, 2007; Olson et al., 2012). These secondary fractures vary significantly in size: the big ones could be as wide as 2 mm, and the small ones could be narrower than 0.1 mm. The narrow secondary fractures are usually unpropped after fracturing job since they are too small to accommodate any commonly available proppants. For proppant-accessible secondary fractures, the understanding of proppant transport from primary fracture into secondary fractures is important for optimizing the completion design.

Proppant transport in a single planar fracture geometry has been experimentally investigated by many previous researchers with a transparent Hele Shaw slot setup (Kern et al., 1959; Liu and Sharma, 2005; Patankar et al., 2002; Woodworth and Miskimins, 2007). Typically, a slurry (water and proppant) is injected into a single vertical slot with constant height and width. Although these studies were all performed at simplified conditions and suffered some limitations of the Hele Shaw slot design, they were still useful for visualizing the movement of proppant within a fracture geometry.

A typical proppant transport pattern could be described as shown in Figure 2.1. For a vertical planar slot geometry, the proppant settles down and accumulates to form a proppant bed near the entrance because of the poor proppant-carrying capacity of slickwater. The proppant bed reaches an equilibrium state, after which newly injected proppant moves deeper into the slot along with some fluidized proppant and deposits

downstream to elongate the proppant bed. This implies that during fracturing, the proppant injected earlier settles down near the perforation hole, and the proppant injected later flows deeper into the fracture. At the top of the fracture, a clear fluid zone exists because of proppant settling, and this region could seal when the fluid pressure dissipates (Warpinski, 2009).

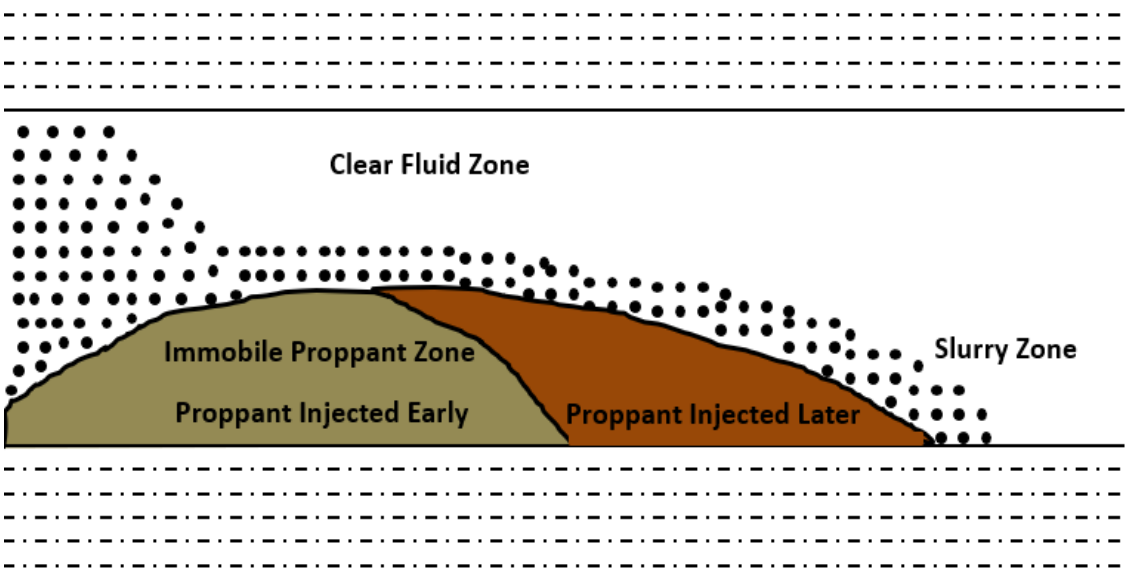

Figure 2.1: Schematic figure of proppant transport in a vertical planar fracture

Typically, three types of proppant motion have been reported: (1) traction motion, (2) saltation motion, and (3) suspended motion (Mack et al., 2014). During the traction motion, the force of a flowing fluid exerted on a proppant slightly exceeds the threshold value for initiation of motion, and the proppant starts to creep upon the proppant bed. During the saltation motion, the proppants start to resuspend as the fluid flows faster. In this stage, proppants resuspended by turbulence could also fall back to the proppant bed quickly. The transport mechanism of rolling, sliding and saltating is commonly known as

the bed-load transport (Biot and Medlin, 1985). Finally, as the turbulence of fast flowing fluid becomes strong enough, the proppants will move in a suspended manner. Medlin et al. (1985) stated that bed-load transport and the formation of a proppant bed may not occur in field condition because the laboratory-scale experimental results do not scale-up with fracture height. However, for a fracture network system, the secondary fractures could be much shorter (vertically) compared to the primary fracture due to geological constraints. In addition, the fluid diverted into the bypass fractures is also very limited (Tong and Mohanty, 2017), which could lead proppant to settle quickly at the junction of fractures. Therefore, the formation of a proppant bed and the concept of bed-load transport may still be valid for the secondary fractures.

Recently, proppant transport in a complex Hele Shaw slot were studied to investigate how proppant could transport from a primary fracture into the secondary fractures (Alotaibi and Miskimins, 2018; Li et al., 2017; Sahai et al., 2014). Sahai et al. (2014) created a primary fracture slot intersecting to a 90 degree secondary fracture bypass and investigated proppant flow from the main slot into the bypass. They evaluated and compared parameters like pump rate, proppant loading and proppant size. They observed a threshold pump rate above which proppants flow into the bypass; otherwise proppants only roll into the bypass under the bed-load transport mechanism. Alotaibi et al. (2018) extended this work and highlighted the mechanism of proppant transport during proppant bed development. They further included friction loss and proposed a scalable correlation for 30/70 brown sand proppants to estimate equilibrium proppant bed height for different flow rates and proppant loadings. Li et al. (2017) built a more complex fracture slot with

30, 60 and 90 degree bypass slot angles. They found the bypass angels would alter the proppant bed height in the primary fracture, but not the proppant bed height in the bypass secondary fractures.

Unlike proppant transport in a single fracture geometry, which has been comprehensively studied, the understanding of proppant transport in 3-D fracture networks is still very limited. So far, no robust data is reported to quantitatively describe the amount of proppant flow into bypass fractures. In chapter 2, we conducted a lab-scale experimental study that aims to quantify the amount of proppant flowing into a secondary fracture from a primary fracture. Parameters like proppant size, proppant loading, injection rate, bypass angle and injection time are systematically evaluated.

2.3 METHODOLOGY

Lab-scale proppant transport experiments were conducted with Hele Shaw slot. The objective of this experimental study was to improve our understanding of proppant transport in complex fracture networks. Slickwater slurries were injected into a set of lab-scale fracture slots, which were designed to mimic intersections of natural fractures with hydraulic fractures. The amount of proppant flowed into the secondary fractures were quantified the first time. A detailed description of the experimental setup, test procedure, results and analysis are included in this chapter.

2.3.1 Fracture Slots with Bypass

Transparent fracture slots, as shown in Figure 2.2, with bypass slot angles 45˚, 90˚ and 135˚ were constructed to mimic intersections of natural fractures with hydraulic

fractures. The inlet is on the left, and the outlet is on the right. The length, height and width of the main slot were 15’’, 3’’ and 0.08’’, respectively. The bypass slot was 7.5’’ in length, and had the same height and width as that of the main one. Usually, the secondary fractures tend to be thinner than the primary fractures in fields. However, common commercial proppants are typically in the range of 200 to 800 um in diameter, and a narrow fracture aperture is very likely to cause jam and screen out. In this study, we focused on the secondary fractures that could accommodate commercial proppants with negligible jamming. Therefore, we set the width of primary and secondary fractures to be the same, 2mm.

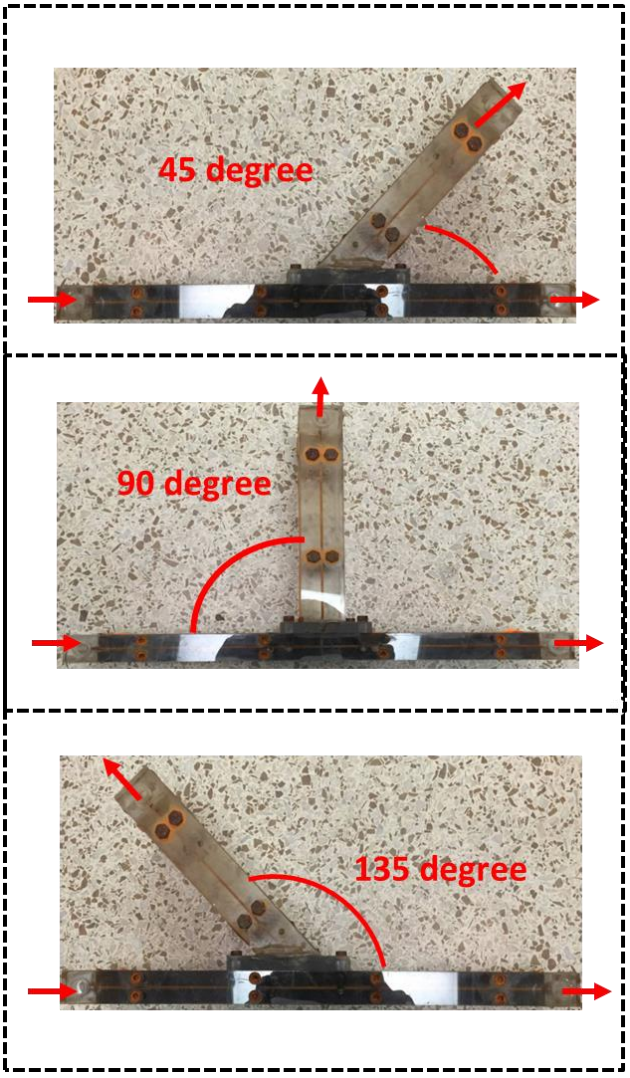

Figure 2.2: Fracture slots with different bypass angles, top view

Figure 2.3 shows the geometry of the main slot. The inlet and outlet were cylindrical holes of 0.5” diameter to distribute fluid and maintain uniform injection. The top and bottom plates were attached to the slot (unlike the figure). The inlet of the bypass slot was placed at the half-way of the main slot.

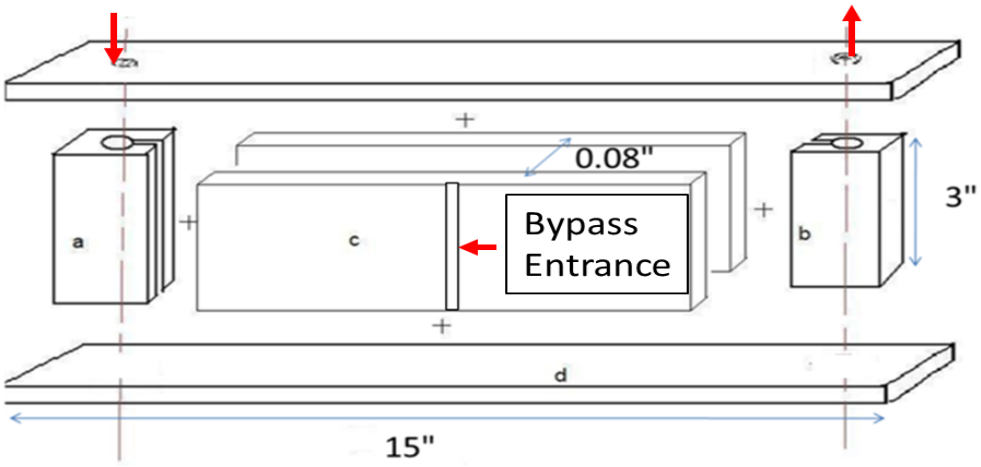

Figure 2.3: Design of the main fracture slot, side view

2.3.2 Experimental Setup

The whole experimental setup consisted of a transparent fracture slot, a water tank, a progressive cavity pump, a proppant funnel, a variable frequency driver (VFD) and two cameras. Water was injected into the slot via the pump at various rates by the VFD controller, and the proppant funnel was adapted to feed proppant at different rates. By changing the ratio of the water injection rate and the proppant feeding rate, the proppant loading could be varied. The proppant transport was recorded with the cameras. Figure 2.4 represents a schematic diagram of the whole system.

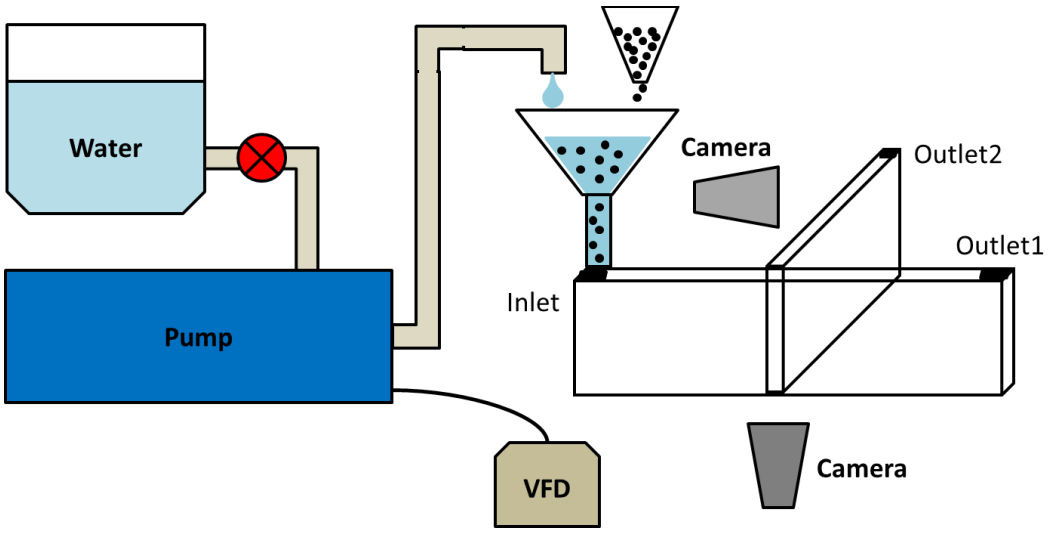

Figure 2.4: Schematic of the experimental setup

2.3.3 Proppant Slurry

Two different sizes of sand proppant with specific gravity of 2.65 were used in this study. Proppant was mixed with tap water to form the slickwater slurry, and no chemical additives were included in the water system. Because the outlet size of the proppant funnel was kept constant, therefore the proppant feeding rate remained constant for a specific type of proppant. Thus, the proppant loading was different for different water flow rates. Proppant loading was calculated by dividing the proppant-feeding rate by the water-pumping rate. The loading rate of 0.29 lb/gal to 1.02 lb/gal, which is within the typical range of field applications (Sahai et al., 2014), was achieved in these experiments.

2.3.4 Experimental Matrix

Proppant sizes, intersection angles, and shear rates were varied. Three bypass intersection angles were used: 45, 90 and 135 degrees. Two proppant mesh sizes were used:

20/40 and 40/70. 20/40 mesh proppant ranges within 420 to 840 um in diameter; 40/70 mesh proppant ranges within 210 to 420 um in diameter. According to the vendor's specification, the 20/40 proppant has 0.7-0.8 roundness (angularity) and 0.8 sphericity; the 40/70 proppant has 0.6-0.7 roundness (angularity) and 0.7-0.8 sphericity.

The typical shear rates of field slickwater fracturing treatments are around 100 s^{-1} to 1000 s^{-1} and the lab experiments were conducted at 300, 600 and 900 s^{-1}. Shear rate in a rectangular channel is calculated as

$$\gamma = \frac{6q}{w^2 h} \tag{2.1}$$

where q is the flow rate in the channel, w is the width (the shorter side of the cross section) and h is the height (the longer side). Therefore, shear rate is proportional to pump rate. This shear rate is a nominal shear rate, not an actual local shear rate because the proppant forms a proppant bed and the fluid flows mainly in the gap at the top of the proppant bed.

Table 2.1 lists the experimental conditions and some important dimensionless numbers. Re_f, Re_p, Re_g and St represent average fluid Reynolds number, particle Reynolds number, gravity Reynolds number and Stokes number, respectively. These dimensionless numbers are defined in Eqs. (2.2) – (2.5) with the slurry injection velocity v_i. ρ_f is the fluid density; μ_f is the fluid viscosity. ρ_s is the proppant density and d_s is the proppant diameter. The fluid Reynolds number indicates the ratio of inertial force to viscous force; the gravity Reynolds number comes from incorporating the sedimentation velocity into Eq. (2.3). A particle with a low Stokes number stays in viscous regime and follows the fluid flow,

whereas a particle with a high Stokes number stays in inertia regime and moves along the initial trajectory.

$$Re_f = \frac{\rho_f v_i D_h}{\mu_f} \tag{2.2}$$

$$Re_p = \frac{\rho_f v_i d_s}{\mu_f} \tag{2.3}$$

$$Re_g = \frac{\rho_f |\rho_s - \rho_f| g d_s^3}{\mu_f^2} \tag{2.4}$$

$$St = \frac{\rho_s d_s^2 v_i}{18 w \mu_f} \tag{2.5}$$

$$D_h = \frac{2wh}{w + h} \tag{2.6}$$

The ranges of Re_p, Re_g and St in this work are similar to those in Sahai's work (Sahai et al., 2014), but Re_f is lower. The Re_g is 3500 and 440 for 20/40 and 40/70 proppants, respectively. Re_f, Re_p and St are listed in Table 2.1.

Table 2.1. List of experiments and parameters

Case #	Bypass Angle (degree)	Proppant (mesh size)	Shear Rate (1/s)	Loading (lb/gal)	Re_f	Re_p	St
2.1	45	20/40	300	0.84	390	60	1.36
2.2	45	20/40	600	0.43	780	120	2.72
2.3	45	20/40	900	0.29	1170	180	4.08
2.4	45	40/70	300	1.02	390	30	0.34
2.5	45	40/70	600	0.52	780	60	0.68
2.6	45	40/70	900	0.35	1170	90	1.02
2.7	90	20/40	300	0.84	390	60	1.36
2.8	90	20/40	600	0.43	780	120	2.72
2.9	90	20/40	900	0.29	1170	180	4.08
2.10	90	40/70	300	1.02	390	30	0.34
2.11	90	40/70	600	0.52	780	60	0.68
2.12	90	40/70	900	0.35	1170	90	1.02
2.13	135	20/40	300	0.84	390	60	1.36
2.14	135	20/40	600	0.43	780	120	2.72
2.15	135	20/40	900	0.29	1170	180	4.08
2.16	135	40/70	300	1.02	390	30	0.34
2.17	135	40/70	600	0.52	780	60	0.68
2.18	135	40/70	900	0.35	1170	90	1.02

2.4 RESULTS AND DISCUSSION

The proppant distribution in the slot and the bypass are shown in Figures 2.5-2.7 for five times 20 s, 30 s, 40 s, 50 s and 60 s for the three shear rates; the time is displayed in the left top corner in seconds. For each time, there are two panels separated by a thick red line; the left panel shows the proppant distribution in the main slot and the right panel shows the bypass slot. The slurry was injected from the left side of the slot. The observations in Figures 2.5-2.7 are described below.

2.4.1 Effect of Shear Rate

Figure 2.5 shows the proppant distribution in the fracture model for case 2.7 (listed in Table 2.1) at 20 s, 30 s, 40 s, 50 s and 60 s at a shear rate of 300 s^{-1}. Proppant settled down quickly in the slot due to low water viscosity and low shear rate; a proppant bed formed immediately near the entrance region. A dotted black line has been added to the pictures to show the boundary of the proppant bed. The equilibrium height of the proppant bed was about 85% of the slot height which was established before 40 s. The large proppant bed height led to a high water velocity at the top gap which carried the newly injected proppant past the proppant bed. This proppant settled down on the downstream slope of the proppant bed where the water velocity decreased and this process extended the length of the proppant bed. The proppant bed in the main slot reached the bypass around 30s. A proppant bed started forming in the bypass at about 30 - 40 s. The proppant settled in the bypass came mainly from the proppant eroded from the top of the proppant bed in the main slot through the bed-load transport mechanism.

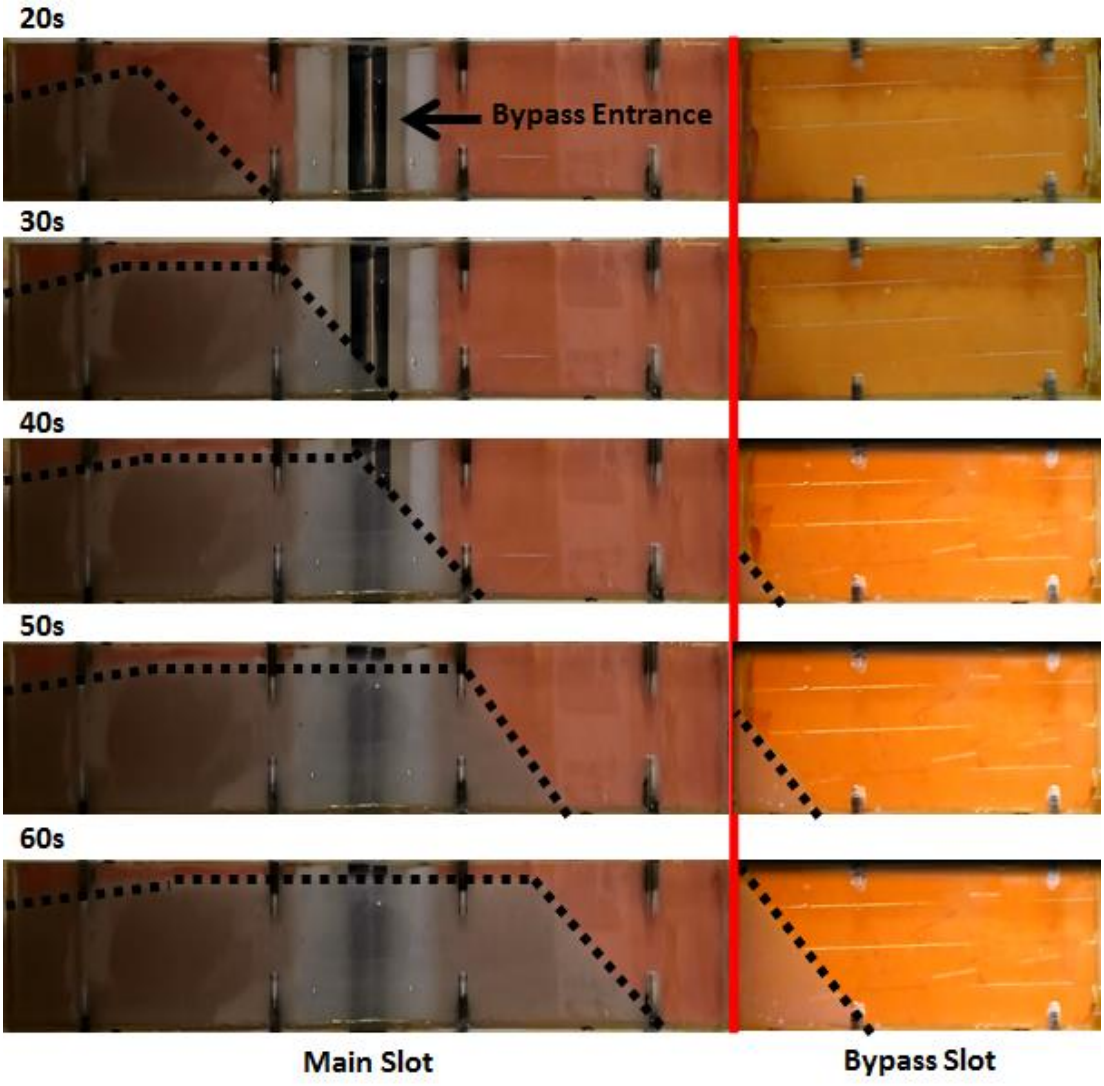

Figure 2.5: Proppant bed in the main slot (left of the red line) and bypass slot (right of the red line), 20/40 proppant, 300 s^{-1} shear rate and 90˚ bypass; the dotted black line shows the boundary of the proppant bed

As the shear rate increased, the proppant bed was formed further away from the entrance (Figure 2.6, case 2.8, at 600 s^{-1}). The equilibrium proppant bed height decreased. The water velocity was large enough to transport the proppant to the bypass before settling and some proppant could flow into the bypass. In this case, the proppant bed appeared in the bypass at 20 s. The height of the proppant bed in the bypass was slightly higher than

that in the main slot due to a smaller water velocity in the bypass. The length of the proppant bed in the main slot increased faster in this case than in the lower shear rate case. The same trend continued as the shear rate was further increased to 900 s^{-1} (Figure 2.7, case 2.9).

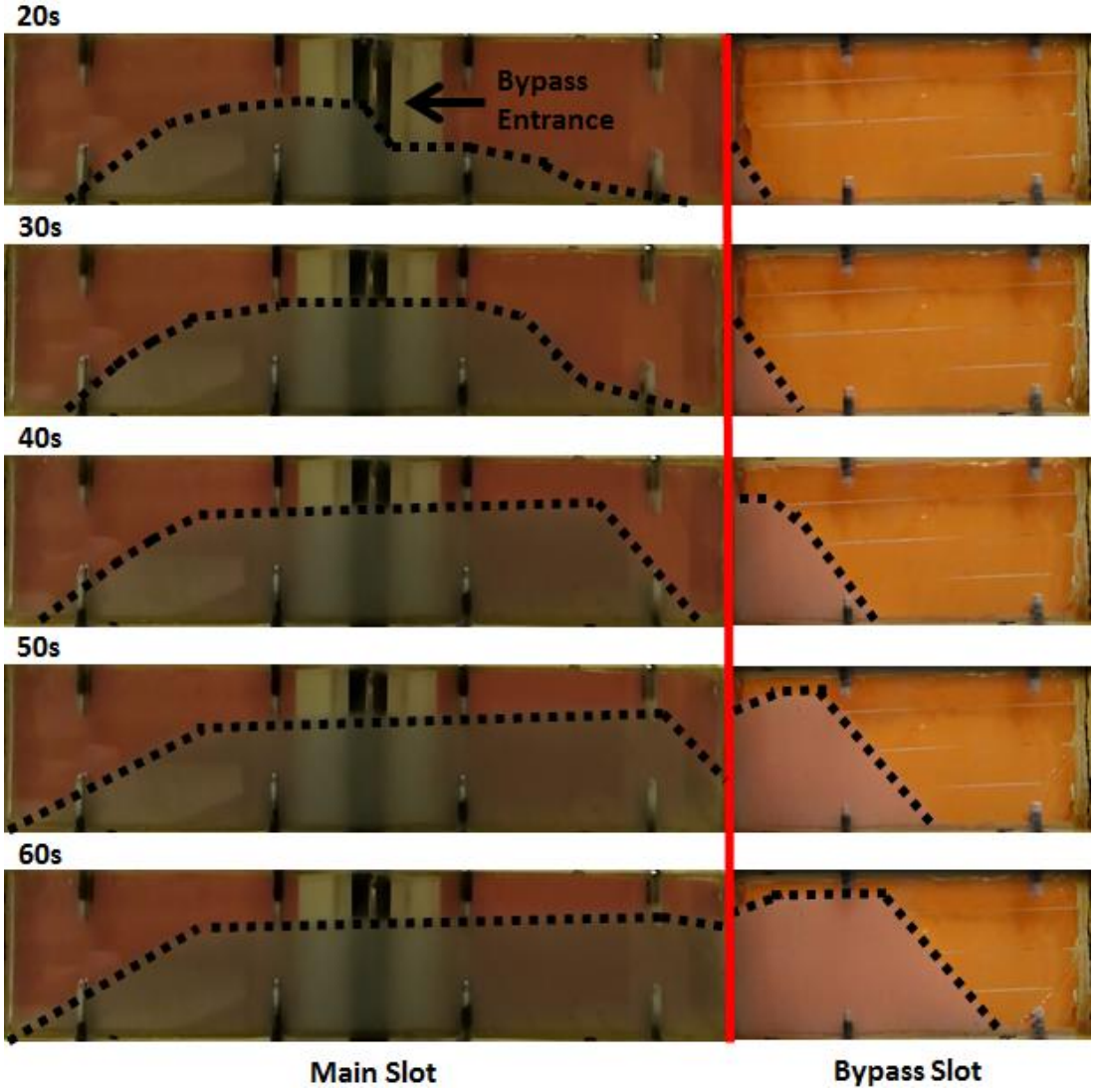

Figure 2.6: Proppant bed in the main slot (left of the red line) and bypass slot (right of the red line), 20/40 proppant, 600 s^{-1} shear rate and 90˚ bypass; the dotted black line shows the boundary of the proppant bed

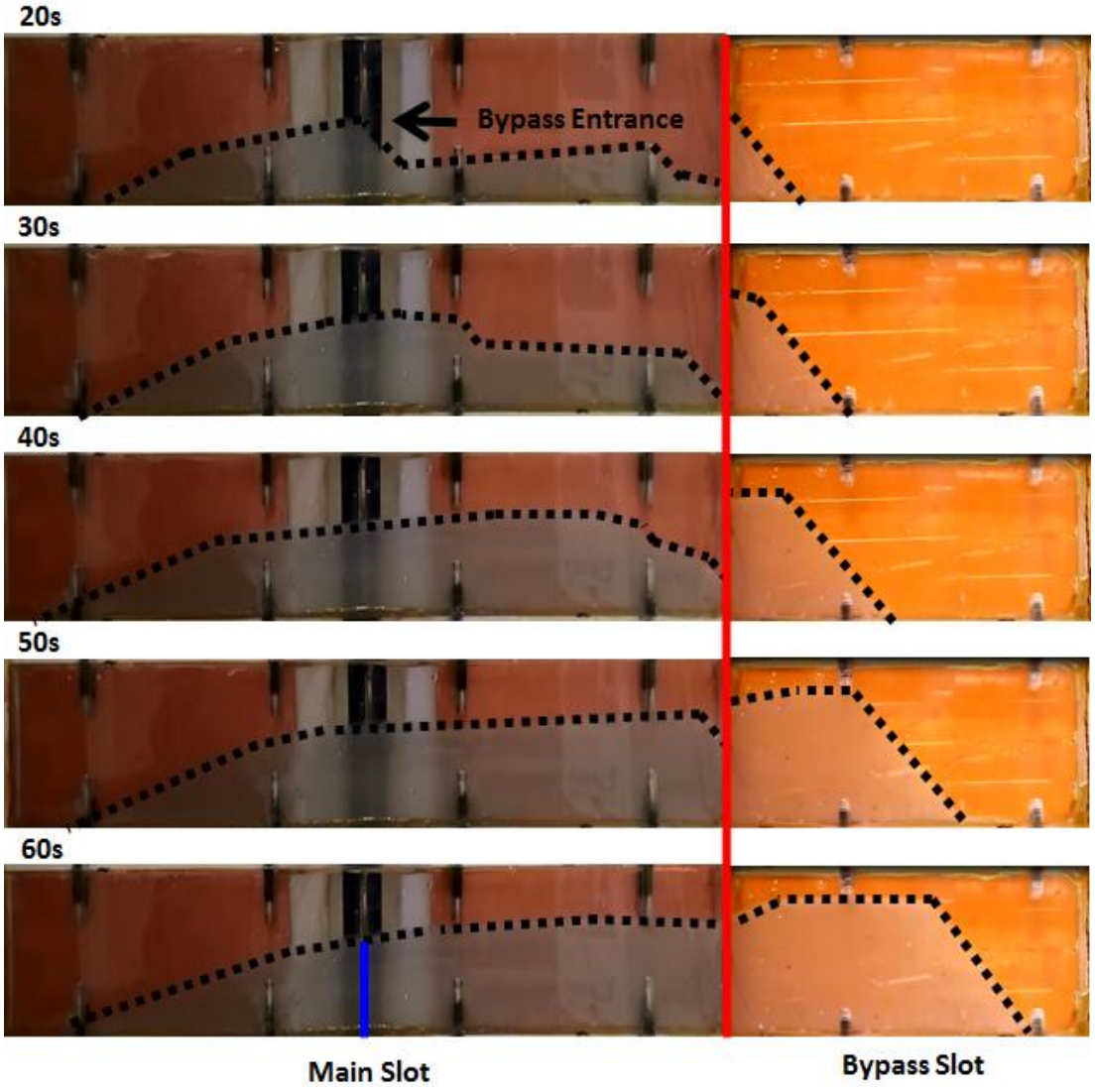

Figure 2.7: Proppant bed in the main slot (left of the red line) and bypass slot (right of the red line), 20/40 proppant, 900 s^{-1} shear rate and 90˚ bypass; the dotted black line shows the boundary of the proppant bed

The proppant bed shape reached equilibrium in the main slot before 60 s for all the cases, and the proppant bed height at the intersection of the bypass was measured (e.g. blue line in Figure 2.7). This height was normalized with the slot height, and then plotted against shear rates in Figure 2.8. As the nominal shear rate increases, the height decreases. This implies that the propped length would increase, but propped height would decrease as shear

rate increases. Figure 2.8 shows that at a low shear rate (300 s^{-1}), the proppant size does not affect the height of the proppant bed. However, at higher shear rates, the proppant bed height decreases as the proppant size decreases. As the proppant size decreases, the velocity to fluidize the proppant decreases; thus the gap (the proppant bed free region at the top of the slot) needed to achieve that velocity increases and thus the proppant bed height decreases. For 45˚ and 135˚ cases, the normalized proppant bed heights are very similar at 900 s^{-1} shear rate (in the circle), and are higher than that of the 90˚ cases. The equilibrium proppant bed height is controlled by the local geometry of the intersection instead of the bypass angle.

Empirical correlations (Wang et al., 2003) have been proposed to estimate the equilibrium proppant bed height H_1. The correlation is described by Eqs. (2.7) and (2.8) as,

$$\frac{h - H_1}{w} = \frac{-0.23\ln(R_G) + 2.92}{1000} R_f{}^{1.2-1.26\times10^{-3}\lambda_f{}^{-0.428}[15.2-\ln(R_G)]} R_p^{[-0.0172\ln(R_g)-0.120]} \tag{2.7}$$

$$\lambda_f = \frac{\mu_f/\rho_f}{w^{3/2}\sqrt{g}} \quad , \tag{2.8}$$

where h and w are the height and width of the slot, respectively. λ_f is the gravity Reynolds number for the fluid, as defined in Eq. (2.8). The definition of R_p and R_f in Eq. (2.7) are based on the width of the slot, w, unlike the definitions in Eqs. (2.2) and (2.3). Figure 2.9 compares the estimated proppant bed height with the experimental values for the 90 degree bypass cases. The correlation overestimates the equilibrium height by 10% to 40%; the overestimation increases as the shear rate increases. The correlation estimates the

equilibrium height of the bed in a long slot. In our study, because the slot is short (only 7.5” long before the bifurcation), the proppant bed does not reach the equilibrium height at the bypass intersection.

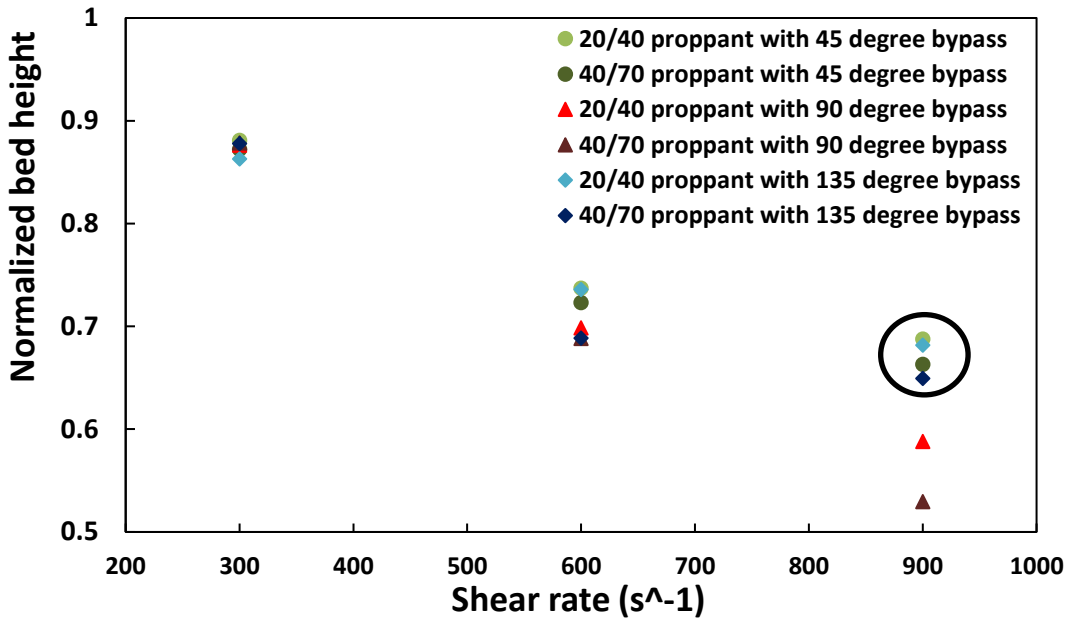

Figure 2.8: Equilibrium proppant bed height at the intersection of bypass for all the cases; the legend denotes the proppant size and the bypass angle

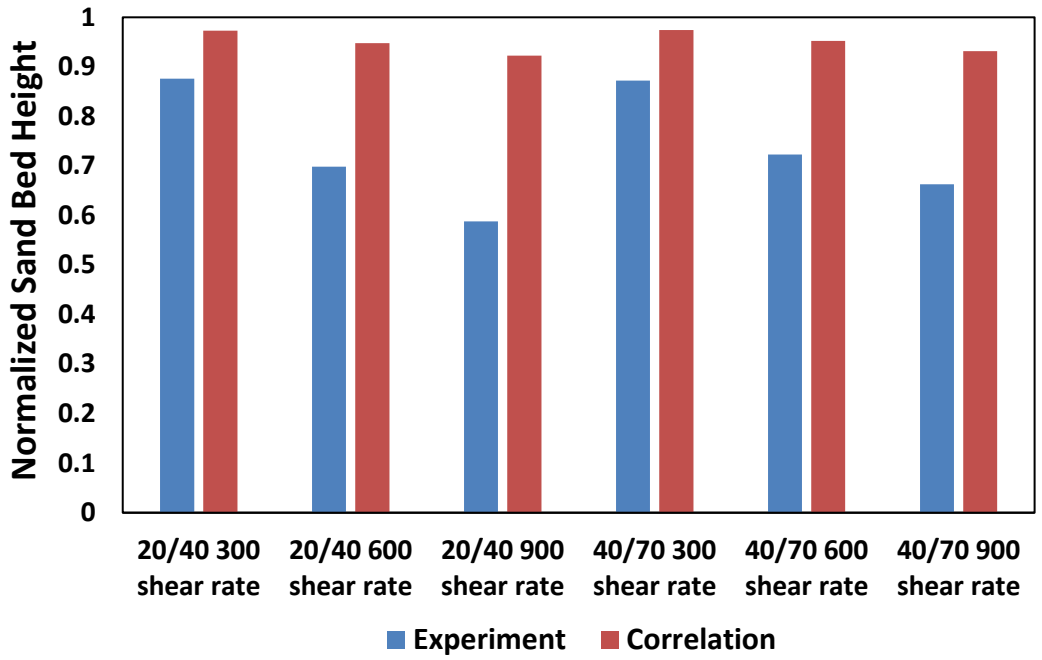

Figure 2.9: Comparison of proppant bed height from experiment and correlation (90 degree cases)

The amount of proppant in the bypass was calculated from the area of the proppant bed (from image analysis via ImageJ, which is an image processing program available from the National Institutes of Health (https://imagej.nih.gov/ij/), assuming that most of the proppant in the bypass fell down to form the proppant bed. The total amount of proppant injected was calculated from the proppant injection rate. Figure 2.10 shows the ratio of proppant in the bypass to the injected as a function of total amount of proppant injected for cases 2.7, 2.8 and 2.9. The proppant size is 20/40 mesh and the bypass angle is 90˚. This figure indicates that as more proppant is injected, the bypass/total ratio increases almost linearly except towards the end of the experiments at the highest shear rate. Moreover, the bypass/total ratio increases with increasing shear rates. This ratio for other bypass angles

and proppant sizes are listed in Table 2.2. At the highest rate, the proppant bed in the bypass reaches the bypass outlet (as shown in Figure 2.11), and some of the proppant flows out of the bypass, which leads to a deviation from the straight-line relationship. For all the cases listed in Table 2.2, as a general trend, the proppant placement in the bypass increases with the shear rate.

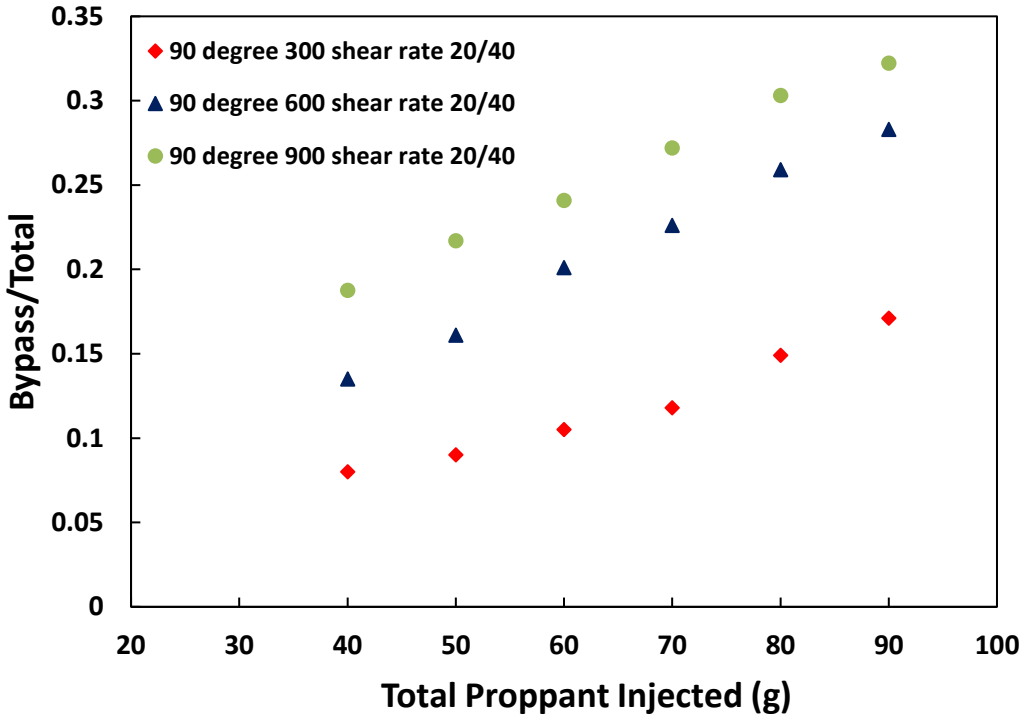

Figure 2.10: Effect of shear rate on the fraction of proppants in the bypass for 90 degree bypass cases

Figure 2.11: Proppant bed in the bypass for case 2.12; 20/40 proppant, 900 s^{-1} shear rate and 90˚ angle at 70 s; the dotted black line shows the boundary of the proppant bed

2.4.2 Effect of Bypass Angle

Figure 2.12 shows the proppant bed build-up in cases 2.2, 2.8, and 2.14. The bypass angle is varied from 45˚ to 135˚ in these cases while the amount of proppant injected, proppant size and shear rate are kept the same. The proppant bed shapes in the main slot are similar. However, for the bypass slot, the proppant bed length is the largest in the 45˚ case and the smallest in the 135˚ case. The blue bar shows the length of the proppant bed in the bypass for the 45˚ case; it is placed for comparison with the other cases. Figure 2.13 shows the effect of the bypass angle on proppant placement in the bypass. The proppant placement in the bypass decreases slightly as the bypass angle increases. The water velocity in the bypass decreases as the bypass angle increases which leads to less proppant transport into the bypass. For all the cases listed in Table 2.2, as a general trend, the smaller bypass angle is better for proppant placement.

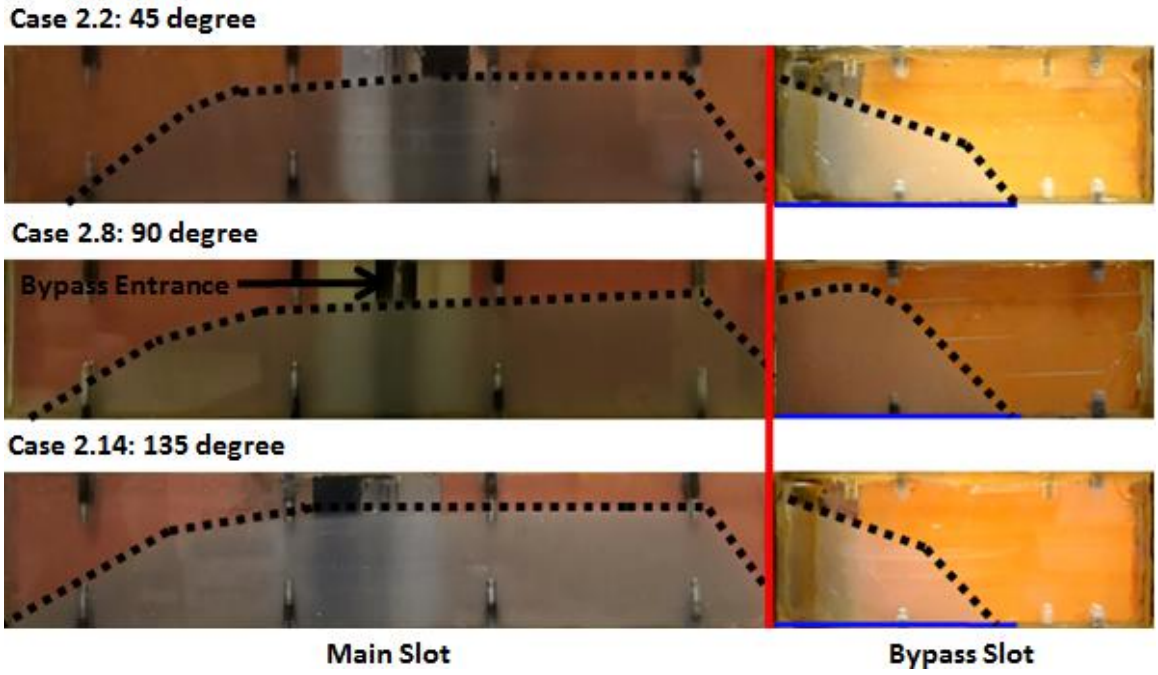

Figure 2.12: Effect of bypass angle on proppant bed for 20/40 proppant at 600 s^{-1} shear rate, 50 s; the dotted black line shows the boundary of the proppant bed

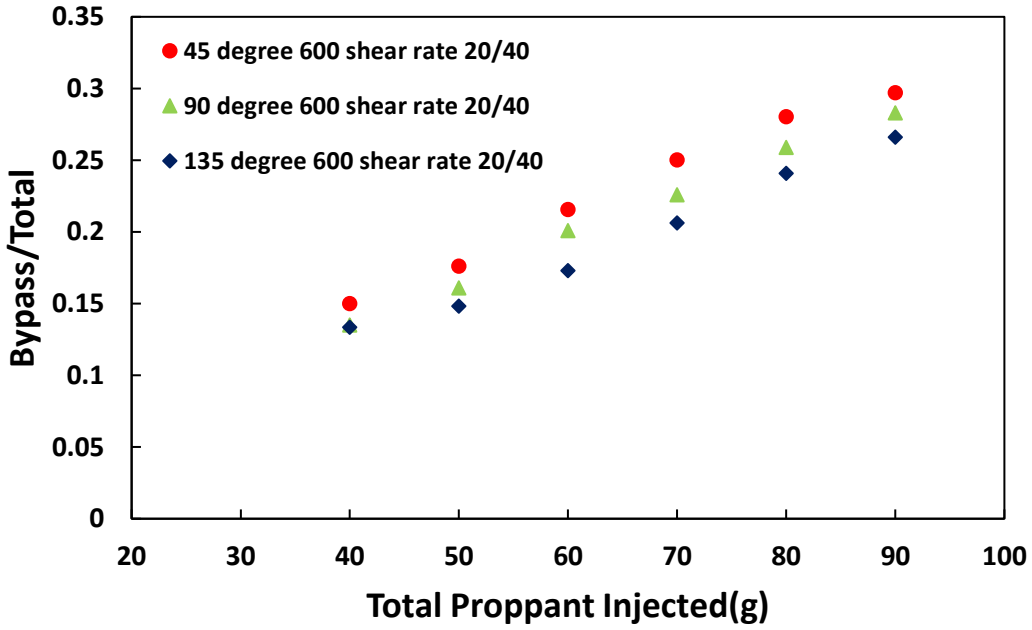

Figure 2.13: Effect of bypass angle on the fraction of proppant in the bypass for 600 s-1 shear rate cases, 20/40 proppant

2.4.3 Effect of Proppant Size

Figure 2.14 shows the proppant bed build-up in cases 2.8 (20/40 proppant) and 2.11 (40/70 proppant). Both cases are compared at the same amount of proppant injected, 600 s^{-1} shear rate and 90˚ bypass. The proppant bed lengths in both the main and the bypass slots are longer for the 40/70 proppant. It is easier to carry the smaller proppant further. The proppant bed height is shorter for the 40/70 proppant. Thus the gap at the top is larger for the smaller proppant, which leads to a smaller velocity at the top gap. That velocity is large enough to carry the smaller proppant. In the case of the smaller proppant, there is a depression in the proppant bed height near the bifurcation. A vortex appears at the bifurcation of the bypass slot, and it can significantly erode the proppant bed if the proppant size is small. Figure 2.15 shows the effect of the proppant size on proppant placement in the bypass. At higher shear rates (600 and 900 s^{-1}), 20/40 proppant has a better placement performance than 40/70 proppant; at low shear rate (300 s^{-1}), the effect of proppant size is not significant. This is valid for all the cases listed in Table 2.2. The proppant placement is calculated from the area of the proppant bed in the bypass, which directly relates to the area of the propped fracture. The proppant placement should not be compared in terms of mass because the density of the proppant bed is likely different for the two proppants and this issue has not been taken into account in this analysis.

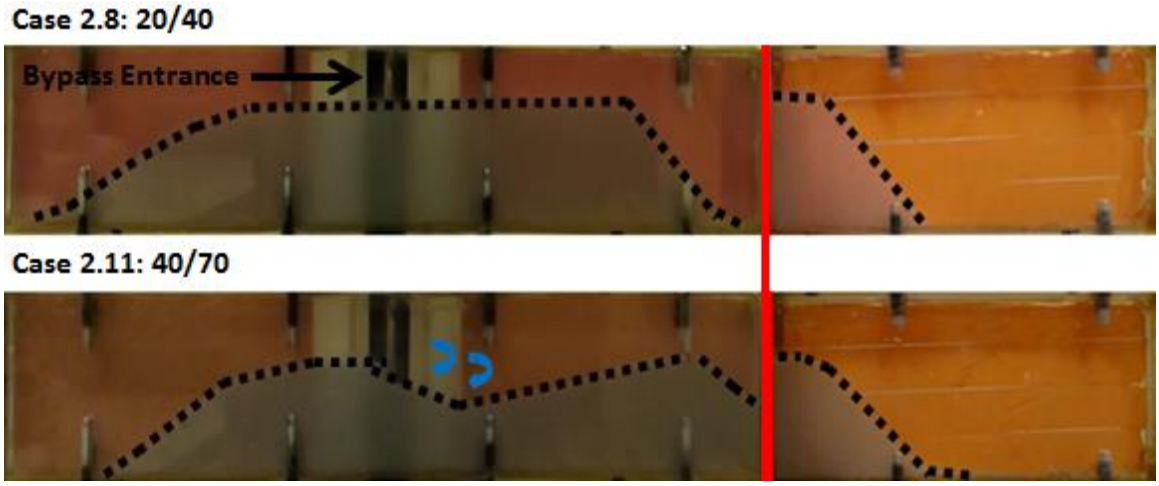

Figure 2.14: Effect of proppant size on proppant bed; 600 s^{-1} shear rate and 90 degree bypass; the dotted black line shows the boundary of the proppant bed

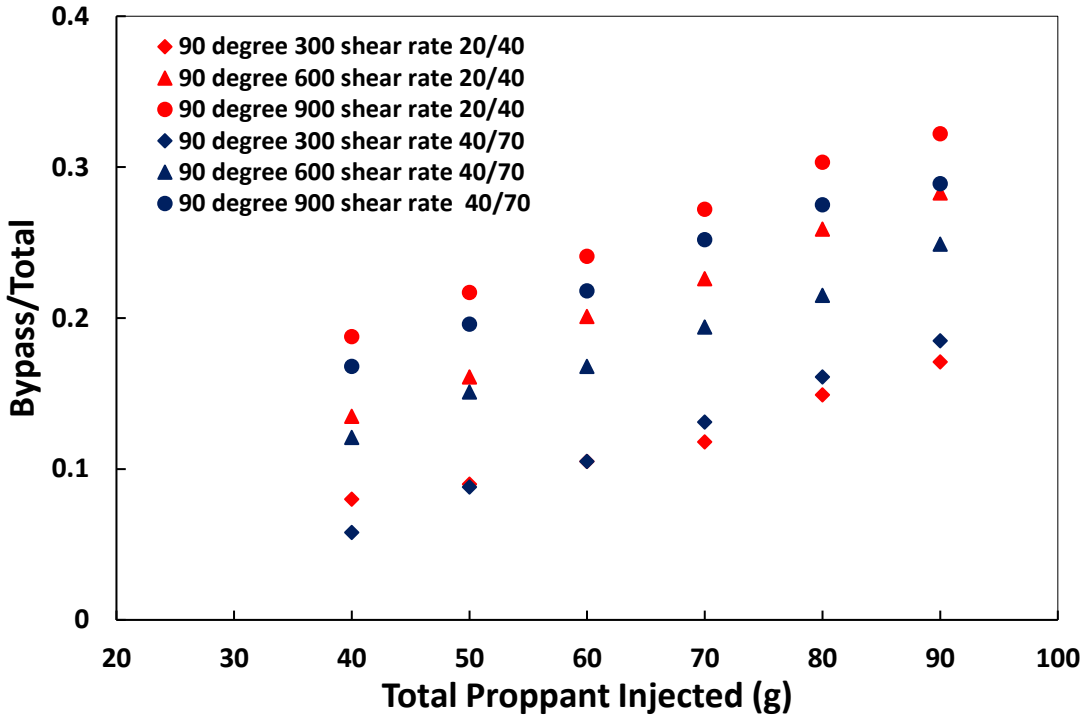

Figure 2.15: Effect of proppant size on the proppant deposited in the bypass for 90˚ bypass

Table 2.2. Experimental values of proppant deposited in the bypass as a fraction of proppant injected

Total Proppant Injected (g)	Bypass/Total					
	40	50	60	70	80	90
Case 2.1	0.125	0.143	0.162	0.181	0.203	0.223
Case 2.2	0.150	0.176	0.216	0.250	0.280	0.297
Case 2.3	0.244	0.261	0.287	0.32	0.354	0.376
Case 2.4	0.127	0.142	0.162	0.179	0.212	0.238
Case 2.5	0.162	0.163	0.172	0.206	0.239	0.273
Case 2.6	0.191	0.223	0.254	0.283	0.303	0.310
Case 2.7	0.081	0.092	0.105	0.118	0.149	0.171
Case 2.8	0.135	0.161	0.201	0.226	0.259	0.283
Case 2.9	0.188	0.217	0.241	0.272	0.303	0.322
Case 2.10	0.058	0.088	0.105	0.131	0.161	0.185
Case 2.11	0.121	0.151	0.168	0.194	0.215	0.249
Case 2.12	0.168	0.196	0.218	0.252	0.275	0.289
Case 2.13	0.07	0.088	0.106	0.121	0.134	0.145
Case 2.14	0.133	0.148	0.173	0.206	0.241	0.266
Case 2.15	0.188	0.216	0.228	0.247	0.269	0.287
Case 2.16	0.085	0.096	0.108	0.125	0.147	0.167
Case 2.17	0.106	0.138	0.167	0.189	0.209	0.226
Case 2.18	0.126	0.146	0.170	0.201	0.228	0.250

Even though the laboratory study was conducted in a fixed fracture geometry with simplified boundary conditions, it serves to improve the understanding of proppant transport in a fracture network geometry with proppant bed formation. In addition, it also helps to generate the first quantified data for bypasses in the literature. Such experimental data could be used to validate proppant transport models, and a well validated model could be coupled with geomechanical fracturing models to simulate more realistic fracturing processes with proppant transport features.

2.5 CONCLUSIONS

This chapter studied the effects of proppant size, bypass angle and injection rate on the placement of proppant in a lab-scale fracture slot model. In addition, the amount of proppant flow into the bypass slot was quantified for the first time. A straight-line relationship is observed between the total amount of proppant injected and the fraction of proppant that flows into bypass secondary fractures. Moreover, the proppant bed length in the downstream of the main slot is always longer than that in the bypass slot for all the cases. This is because the fluid velocity flowing into the secondary slot is small, and most of the proppant would settle down at the junction of the primary and the secondary slot due to the low viscosity of water. The main conclusions obtained are the following:

1. For the first time, the amount of proppant flowing into a bypass fracture was quantified in a lab-scale study. As more proppant is injected, a larger portion of the proppants flow into the bypass fracture.

2. Large proppant, such as 20/40 mesh size, is not suspended easily by low-viscosity slickwater fluid, and this leads to a fast buildup of proppant bed near the entrance of the fracture slot.

3. The orientation of bypass fracture could affect the placement of proppant in secondary fractures. Based on lab-scale experiments, a smaller bypass angle only leads to slightly better placements of proppant in secondary fractures.

4. Bed-load transport is one of the main mechanisms in proppant transport in lab-scale study. Therefore, a faster injection rate would result in a greater bed-load transport process, and consequently a larger bypass/total ratio.

5. The existence of secondary fractures could significantly slow down the liquid velocity inside fractures. Therefore, for low viscosity fluid, severe proppant settling could be expected at the junctions of the primary fracture and the secondary fractures. As a result, low viscosity fluid would lead to an uneven proppant placement in secondary fractures.

NOMENCLATURE

Re	Reynolds number
St	Stokes number
γ	Shear rate (s^{-1})
p	Pressure (Pa)
$\vec{g}$	Gravitational vector (m/s^2)
d	Diameter (m)
w	Slot width (m)
h	Slot height (m)
D_h	Hydraulic Diameter
H	Proppant equilibrium height
ρ	Density (kg/m^3)
v_i	Nominal injection velocity (m/s)
μ	Viscosity (kg/(m·s)
λ_f	Fluid Gravity Reynolds Number (dimensionless)

Chapter 3: Experimental Study of Proppant Transport in Foam Fluid

3.1 SUMMARY

As discussed in chapter 2, low-viscosity fluid has a poor proppant-carry capacity, which often leads to a poor proppant placement. Deeper and higher fractured surfaces are very likely to remain closed after the release of the fluid pressure. Viscous fluids, like gel or foam fluids, could be used to slow down proppant settling and achieve greater proppant coverage.

So far, the understanding of proppant transport in foam fluid is very limited, and most of the previous studies only report proppant settling in a static foam column. However, the property of a dynamic foam is very different from a static foam. The purpose of chapter 3 is to visualize dynamic proppant transport in foam fluid in a lab-scale Hele Shaw slot. Foam quality, injection rate and proppant loading are systematically investigated.

Our results show that foam drainage plays an important role in proppant transport. Dry foams with little liquid drainage lead to outstanding proppant transport performance; wet foams with severe liquid drainage lead to poor proppant transport performance. In addition, the absolute value of shear rate does not have a simple relationship to the settling of proppants. The foam microstructure dominates proppant settling in addition to the effective viscosity of the foam fluid. The observations of foam finger protrusions and proppants moving against gravity support this hypothesis.

This chapter is based on (Tong, Singh, and Mohanty, 2018). Singh helped with the experiments and Dr. Mohanty supervised the project.

Tong, S, Singh, R., Mohanty, K.K., 2018. A visualization study of proppant transport in foam fracturing fluids. Journal of Natural Gas Science and Engineering 52, 235–247.
https://doi.org/10.1016/j.jngse.2018.01.030

3.2 INTRODUCTION

For unconventional shale exploitation, the most popular completion design is slickwater fracturing treatment. In a typical slickwater fracturing job, a large volume of slickwater mixed with fine proppant (e.g. 40/70 to 100 mesh) is pumped at a high pumping rate. Slickwater fracturing gains its popularity because it can economically create large, complex fracture networks. However, due to the low viscosity of slickwater fluids, common commercial proppants (such as sand) tend to fall down very quickly to the bottom of the fracture after travelling a short distance away from the perforation hole, leaving lots of upper and deeper fractured surfaces sealed and consequently lower production of the well (Kern et al., 1959; Sahai et al., 2014; Shiozawa and McClure, 2016; Tong and Mohanty, 2017, 2016; Warpinski et al., 2009).

The movement of a particle in a carrier fluid is primarily determined by the gravitational force and the drag force exerted on the particle by the carrier fluid. Hence, there are two common methods to transport the proppants deep into the fractures. The first method is to use ultra-light weight proppants (ULWP) (Gaurav et al., 2012; Gu et al., 2015). ULWPs usually have a specific gravity of 1.08 – 2.0 (which lies between the specific gravity of water and sand). Based on Stoke's Law, ULPWs have significantly smaller settling velocity compared to that of sand. However, ULWPs typically are not very strong and can only offer a lower conductivity compared to conventional proppants (Rickards et al., 2006). Additionally, ULWPs could suffer from flowback issues because of their low density, and this could lead to poor proppant placement and severe abrasion of the infrastructures. The second method is to use viscous fracturing fluid. The most common way of viscosifying is to add polymer, such as guar gum, to the fracturing fluids (Barati and Liang, 2014). Polymerized fracturing fluid can carry the proppants well, but it can potentially plug the tiny pores in low permeability shales and damage the productivity of

the fractures (Ribeiro and Sharma, 2012; Yang and Balhoff, 2017). Recently, Zhou (2015) included guar-based polymeric particles in the fracturing fluid, and these particles could take the space between the proppants and prevent proppants from settling. After cleaning, no gel or filter cake damage was found, and the fracture could regain 91% of its conductivity. However, these polymeric particles could occupy a large portion of the fractured volume, and could also lead to a poor utilization of the fractured surface.

Another alternative approach is to use foam fluids to achieve high viscosity. Foams are usually generated from a base fluid consisting of a surfactant, a polymer stabilizer such as guar and other additives (Yekeen et al., 2018). Usually, foam is a dispersion of gas bubbles in a liquid and is typically characterized by the gas volume fraction ϕ_g, as shown in Figure 3.1 (Faroughi et al., 2018). The maximum volume fraction of monomodal gas bubbles that are closely packed whether hexagonally or randomly is defined as the wet limit, ϕ_t, and it is between 0.64 - 0.74. When ϕ_g is smaller than ϕ_t, the mixture is defined as "energized fluid" in the petroleum literature. In our study, we focused on the foam regime (theoretically $\phi_g > 0.64$) because it possesses several benefits including—reduced water consumption, enhanced proppant transport, minimal fluid leakage and accelerated fluid clean-up (McAndrew et al., 2017; Wanniarachchi et al., 2015; Xu et al., 2017).

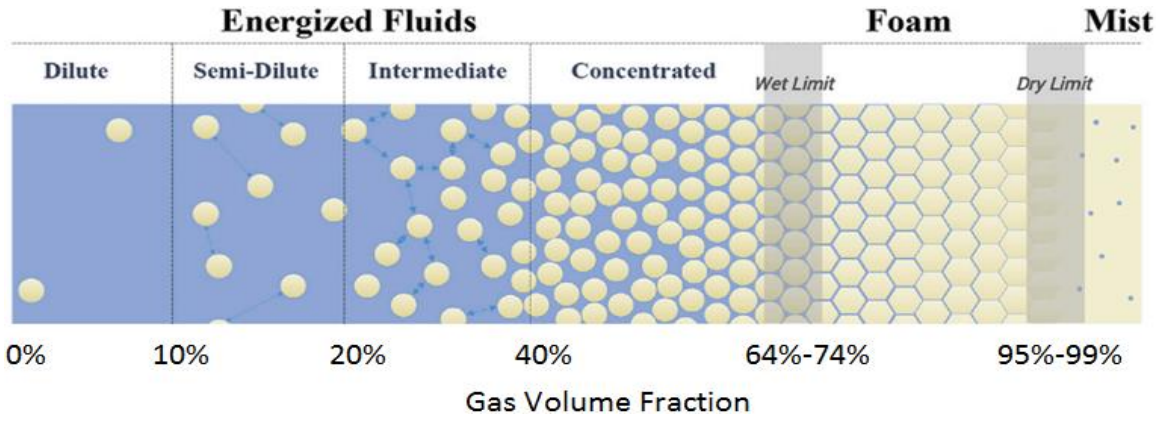

Figure 3.1: 2D illustration of common classification of gas-liquid mixture according to gas volume fraction. Here the dispersed phase is assumed to be monomodal (Faroughi et al., 2018)

Foam fluid has been widely investigated by previous researchers (Reidenbach et al., 1986; Harris and Reidenbach, 1987; Harris, 1989, 1995). Foam structure is not stable, and there are three mechanisms causing foam destabilization (Bhakta and Ruckenstein, 1997; Koehler et al., 2000; Verbist et al., 1996; Voorhees, 1985): liquid drainage in lamellae, bubble coalescence, and Ostwald ripening. The first two are the dominating mechanisms in destabilizing foam during a hydraulic-fracturing treatment. Drainage is induced by gravity and capillary force, which could be minimized by increasing the foam quality and viscosifying the liquid portion with polymers or nanoparticles (Singh and Mohanty, 2014). Bubble coalescence is caused by lamella thinning and perturbation in liquid firms, which depend on surfactant types, concentrations and contact to hydrocarbons (Schramm, 1994).

Static foam tests are one of the most common bulk foam stability experiments which are extensively used in the literature for screening foaming formulations (Andrianov et al., 2012; Singh and Mohanty, 2016; Vikingstad et al., 2005). A standard qualitative test is the foam half-life (HL) test, which monitors the decay of a static foam column to half of

its original height. HL test is simple and easy to conduct for evaluating foam stability with different chemical additives such as polymers and nanoparticles. Additionally, foam stability could also be evaluated dynamically (Harris and Reidenbach, 1987; Harris, 1995), and usually a foam loop (Gu and Mohanty, 2015) is used to mimic shear and HPHT (High pressure high temperature) condition in a field fracturing treatment.

In addition to foam stability, foam rheology is an important parameter for fracturing treatment, and it is found to depend on foam quality, foam bubble texture, foaming surfactant, viscosity of external phase, internal phase, pressure and temperature. Based on numerous literature study, foam fluid is usually a shear-thinning Non-newtonian fluid (Faroughi et al., 2018; Gu and Mohanty, 2015; Harris, 1995; Tong et al., 2017; Tong et al., 2018), which means the foam viscosity decreases as the foam flows faster. Generally, a Herschel-Bulkley model or a power-law model was used to describe the rheological behavior of foams (Reidenbach et al., 1986) with key parameters such as foam consistency index, K, foam behavior index, n, and yield stress γ_0.

Even though foam fluid has been extensively investigated for fracturing purpose, the studies exclusively focuses on proppant-free foams under dynamic conditions. Unlike single-phase fluid, the microstructure of foam fluid could significantly affect the settling behavior of proppant (Jing et al., 2016) as the proppant could experience the existence of the bubbles. In chapter 3, we conducted a lab-scale experimental study that aims to visualize and quantify dynamic proppant settling in a single Hele Shaw slot at ambient pressure and temperature. Parameters like proppant loading, injection rate and foam quality are systematically evaluated.

3.3 METHODOLOGY

3.3.1 Materials

A C14-16 alpha-olefin sulfonate (AOS) anionic surfactant (39% active) was used in this study. This surfactant is an effective foaming agent and has been reported in foam fracturing and EOR studies (Singh and Mohanty, 2017). A partially (30%) hydrolyzed polyacrylamide polymer with a molecular weight of 8 million Dalton was added into the solution as a viscosifier. Sodium chloride was used as received. 20-40 mesh size black ceramic proppant (specific gravity: 3.36) was selected in this study for better visualization (Kadhim et al., 2017). The foam fluid was prepared with 0.5 wt% surfactant in 1.0 wt% NaCl brine with 100 ppm polymer. Foam rheology was quantified with a power-law model based on pipe rheometry measurements. Measurement details could be found elsewhere in the literature (Enzendorfer et al., 1995).

3.3.2 Fracture Slot

A transparent Hele-Shaw slot was used to mimic hydraulic fractures, and it is 30'', 6'' and 0.08'' in length, height, and width, respectively. This slot was designed to visualize the process of proppant transport in foam. Figure 3.2 shows the schematic figure of the slot design. The inlet is on the left, and the outlet is on the right. The inlet and outlet holes were 0.5'' in diameter which run along the height of the slot (components a and b in Figure 3.2). Note that this diameter (0.5") is very large as compared to the width of the slot (0.08"); therefore, the holes also act as a fluid distributor which minimizes the entrance effects. Both top and bottom plates were attached to the slot (unlike the figure). Foam-proppant

slurry was mixed in a blender at a fixed rpm to form a homogeneous mixture of proppant-laden foam. This mixture was injected in the slot using a peristaltic pump running at a constant flow rate, as shown in Figure 3.3. The movement of proppant was recorded with cameras, and the trajectory of proppant was tracked in a video analysis software. The bubble texture of the foam in the Hele-Shaw cell was characterized using a Nikon optical microscope equipped with a high-resolution camera. The image processing was done using the open-source Fiji software. The pressure drop across the cell was measured using a Rosemount differential pressure transducer.

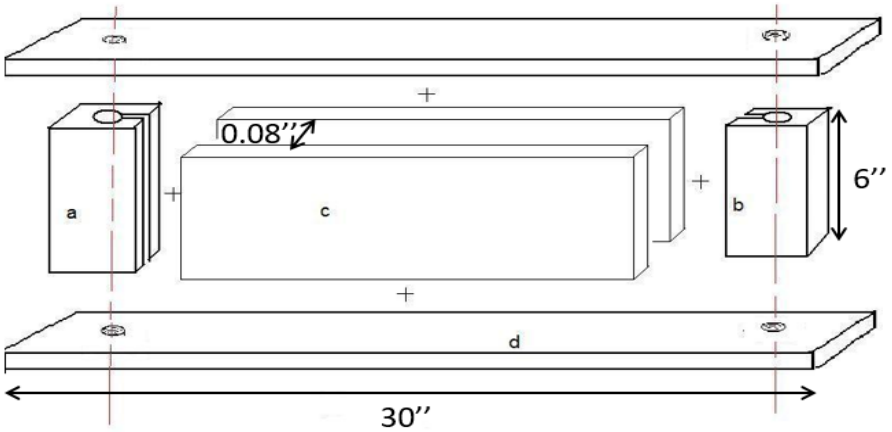

Figure 3.2: Dimensions of the slot (hele-shaw slot) used in the study

Figure 3.3: Experiment setup

3.3.3 Experimental Conditions

Black-colored, 20/40 ceramic proppant (specific gravity: 3.36) was used for better visualization (compared to sand). This proppant is large and heavy, and could be regarded as the worst scenario in field applications. Effects of proppant loading and shear rate were investigated. The concentration of proppant varied from 2.5 vol% to 10.0 vol% (around 0.6 – 2.4 ppg sand loading), which is within the range of typical field applications. Due to the limitation of the pump, the maximum injection velocity and corresponding shear rate were 0.0467 m/s and 140 s^{-1}, respectively. The nominal shear rate (γ) in a rectangular channel is defined as

$$\gamma = \frac{6q}{w^2 h} \tag{3.1}$$

where q is the volumetric flow rate in the channel, w is the width (the shorter dimension of the channel), and h is the height. This shear rate is not an actual local shear rate because the formation of proppant bed can significantly affect the flow of the fluid.

The experimental matrix is listed in Table 3.1. 80% quality foam was studied comprehensively, and several experiments were conducted with the 70% quality foam for comparison. Foam quality is defined as the volume percentage of gas in the foam. Experiments were performed at common shear rates observed in the field applications (Ouyang et al., 2012). Proppant loading is the volume% of proppant in the slurry. Equivalent Sand Loading (ESL) is the lbs of sand proppant per gallon of slurry if sand is used as the proppant at the same volume %. It is calculated by multiplying sand density

(lb/gallon) and proppant volume concentration. ESL is another way to express proppant loading.

Table 3.1 Experimental Matrix

Case #	Foam quality	Nominal shear rate (1/s)	Nominal velocity (cm/s)	Proppant Loading (vol%)	ESL (ppg)
3.1	80%	42	1.39	2.5	0.6
3.2	80%	42	1.39	5.0	1.2
3.3	80%	42	1.39	7.5	1.8
3.4	80%	42	1.39	10.0	2.4
3.5	80%	84	2.78	2.5	0.6
3.6	80%	84	2.78	5.0	1.2
3.7	80%	84	2.78	7.5	1.8
3.8	80%	84	2.78	10.0	2.4
3.9	80%	140	4.67	2.5	0.6
3.10	80%	140	4.67	5.0	1.2
3.11	80%	140	4.67	7.5	1.8
3.12	80%	140	4.67	10.0	2.4
3.13	70%	42	1.39	2.5	0.6
3.14	70%	84	2.78	2.5	0.6
3.15	70%	140	4.67	2.5	0.6
3.16	70%	140	4.67	5.0	1.2
3.17	70%	140	4.67	7.5	1.8

3.4 Results and Discussion

3.4.1 Static Foam Test

Static foam tests (SFT) are one of the most common bulk foam stability experiments which are extensively used in the literature for screening foaming formulations (Andrianov et al., 2012; Singh and Mohanty, 2016; Vikingstad et al., 2005). In this study, SFT were conducted to investigate the effect of polymer and foam quality on the bulk foam stability. Static foam tests were conducted for 70% and 80% foam with and

without 100 ppm polymer. The decay of foam column height was monitored up to 48 hours. These tests were performed at room condition. Figure 3.4a shows the normalized foam height against the decay time in hours. Half-life, which is the time that the foam takes to decay to half of its original height, could be obtained from the figure. Figure 3.4b shows the decay profile of the first 2 hours, which is a timeframe of a typical fracturing application. There are two main foam destabilization mechanisms which govern the bulk foam stability: Ostwald ripening and liquid drainage in lamellae. The addition of polymer increases the viscosity of the liquid phases which reduces the rate of liquid drainage process. Figure 3.4a shows that the foam decay profile for the cases of 80% foam with polymer is much slower than 80% foam without polymer, especially during late times (>12 hours) when foam lamellae are very thin.

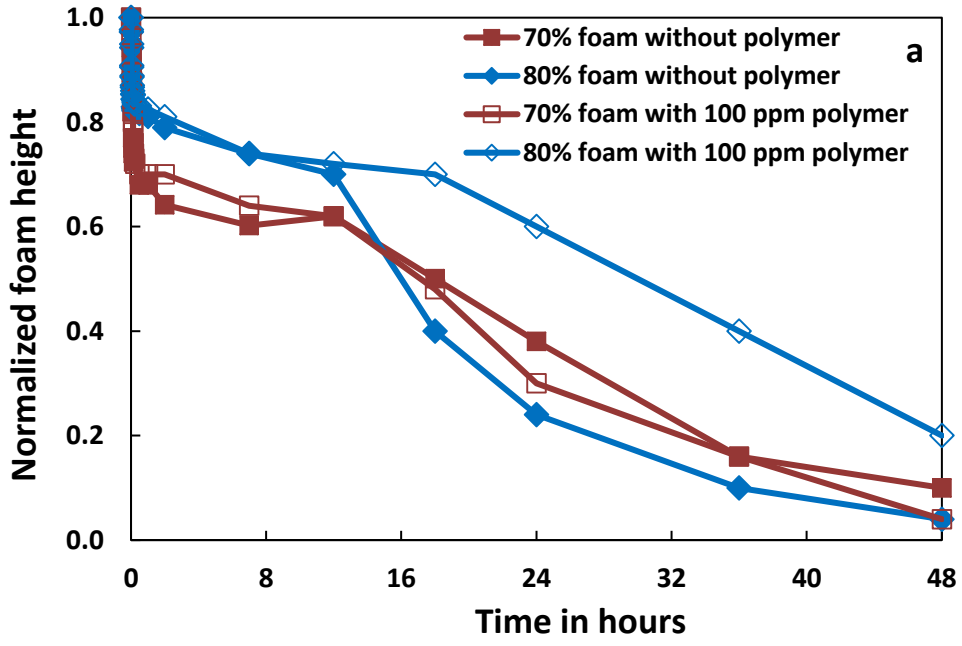

Figure 3.4: Normalized foam height (a) for 48 hours (b) for the first 2 hours

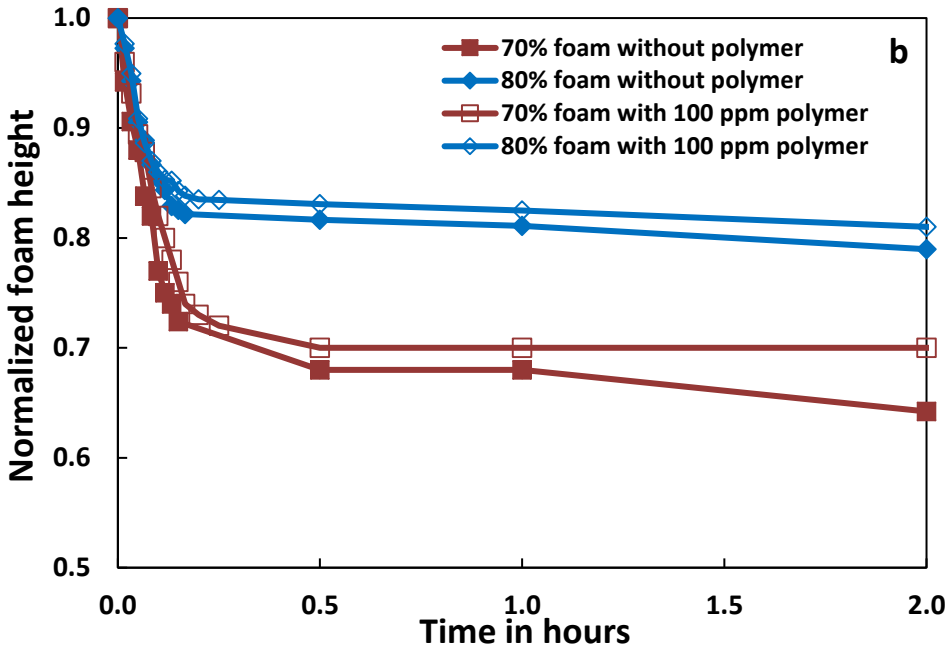

Figure 3.4: Continued

3.4.2 Foam Rheology

A pipe viscometer was used to quantify the foam rheology. The length (L) and inner diameter (d) of the pipe are 2 ft and 0.25 inch, respectively. Different injection rates were applied for different shear rates, and pressure drop (ΔP) was measured along the pipe. The apparent wall shear rate is calculated as

$$\gamma_{wa} = \frac{32q}{\pi d^3} \tag{3.2}$$

and the wall shear stress τ_w is calculated as

$$\tau_w = \frac{d\Delta P}{4L} \tag{3.3}$$

where q is the volumetric foam injection rate in the pipe. A power-law model was used in this study to describe the foam rheology:

$$\tau = K\gamma^{n} \tag{3.4}$$

where K is the consistency index and n is the flow behavior index. γ_{wa} should be converted to intrinsic shear rate γ_{wi} in Eq. (3.4) if τ is the wall shear stress τ_w (Enzendorfer et al., 1995). The conversion could be done as follows:

$$\gamma_{wi} = \frac{3n' + 1}{4n'}\gamma_{wa} \tag{3.5}$$

where n' is defined as

$$n' = \frac{d\ \ln(\tau_w)}{d\ \ln(\gamma_{wa})}. \tag{3.6}$$

According to Enzendorf (1995), the relationship between n and n' could be expressed as

$$n\ = \frac{n'}{1 - \frac{1}{3n' + 1}\frac{dn'}{d(l\,n(\tau_w))}} \tag{3.7}$$

For power-law behavior fluid, $\frac{dn'}{d(l\,n(\tau_w))} = 0$, therefore $n = n'$.

The consistency index, K could be found by

$$K = \frac{K'}{(\frac{3n' + 1}{4n'})^{n'}} \tag{3.8}$$

where K' is the wall shear stress τ_w at $\gamma_{wa} = 1\ s^{-1}$. Finally, the apparent viscosity of the foam at different shear rates could be calculated as:

$$\mu_a = K{\gamma_{wi}}^{n-1} \tag{3.9}$$

Figure 3.5a shows the log-log plot of γ_{wa} vs. τ_w, and the apparent viscosity of the foam could be given by the equations in Figure 3.5b. Based on the measured data, the foam behaves like a shear-thinning fluid.

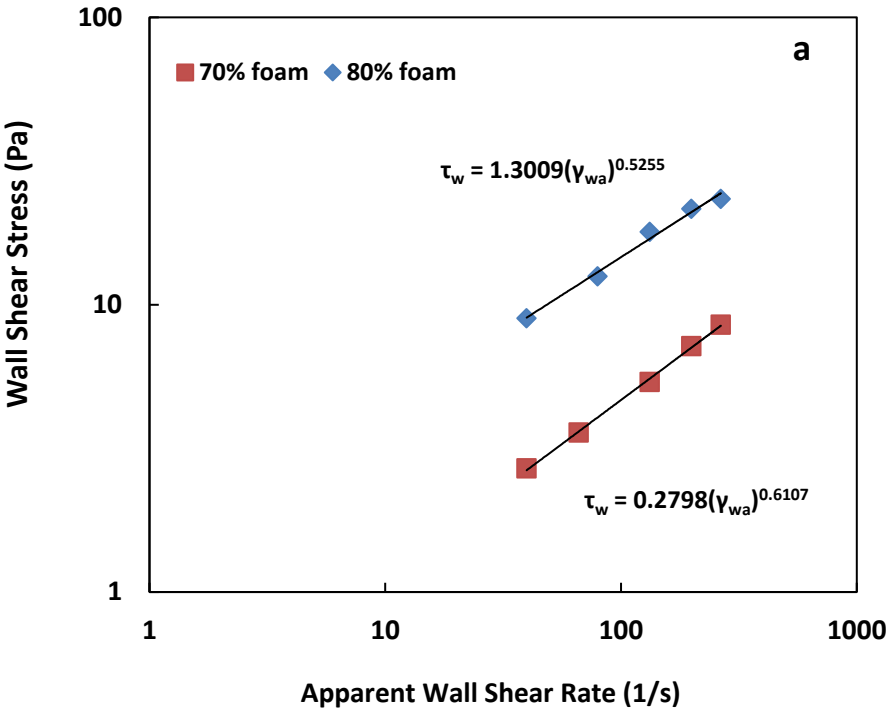

Figure 3.5: Foam rheological data (a) wall shear stress and (b) apparent viscosity

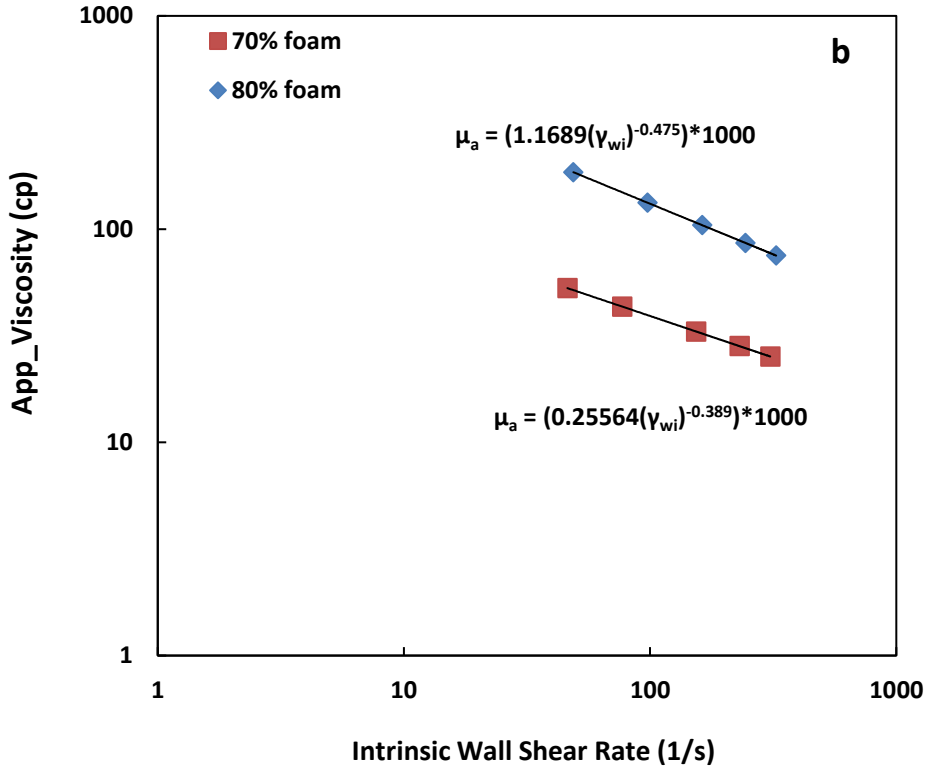

Figure 3.5: Continued

3.4.3 Characterization of Foam-Flow in Hele-Shaw Cell

3.4.3.1 Bubble Texture Analysis

Foam texture or the bubble size distribution is one of the most important parameter that governs the foam rheology in both bulk and porous media. Several studies have shown that smaller bubbles (often referred as 'finer bubbles') lead to larger flow resistance during flow through porous media (Friedmann and Jensen, 1986; Kovscek and Radke, 1994). Proppant-free foam was injected in the Hele-Shaw cell at two different qualities (70% and 80%) and the flow was stopped once the cell was completely filled with foam. Then, optical micrographs of the foams were captured at dimensionless slot length at $\bar{X}$ = 0.25 and $\bar{X}$ =

0.75. Figure 3.6 shows the bubble texture for 70% foam. Figure 3.6a, c show the snapshots at $\bar{X}$ = 0.25, and Figure 3.6b,d show the snapshots at $\bar{X}$ = 0.75. The average bubble size was quantified using image analysis via Fiji software. For 70% quality, it was 1258±71 microns and 1399±608 microns at $\bar{X}$ = 0.25 and $\bar{X}$ = 0.75, respectively. It can be seen that only a small change in bubble texture was observed between foam near inlet and outlet. It was expected as the permeability of the cell is high and the expected pressure drop across the cell is low. (The same was confirmed by pressure drop measurements and is discussed in subsequent section). Similarly, foam of 80% quality was injected in the cell and bubble morphology was studied. Figure 3.7a,c and Figure 3.7b,d show the bubble texture at $\bar{X}$ = 0.25 and $\bar{X}$ = 0.75, respectively. The corresponding average bubble diameter was found to be 966±539 microns and 1149±585 microns. Note that, similar to the 70% quality case, in this case also minimal change in the bubble texture was observed spatially because of very small pressure drop. Also, the bubble size in 70% case was found to be bigger than that of 80% case indicating relatively weaker foam in the former case as shown in Table 3.2.

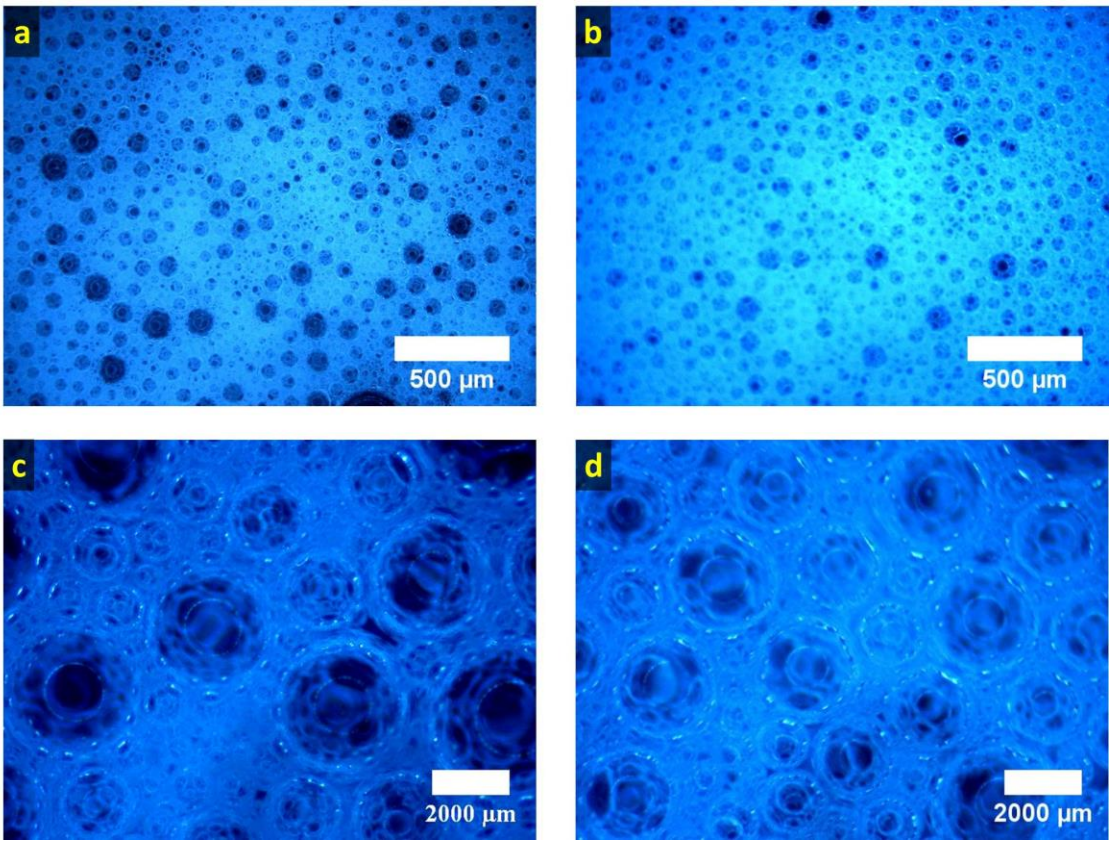

Figure 3.6: Foam texture of 70% quality foam at (a,c) $\bar{X}$ = 0.25 and (b,d) $\bar{X}$ = 0.75

Table 3.2 Average bubble diameter of the foam of different quality in the Hele-Shaw cell

Foam quality	Bubble diameter at $\bar{X}$ = 0.25 in microns	Bubble diameter at $\bar{X}$ = 0.75 in microns
70%	1258±711	1399±608
80%	966±539	1149±585

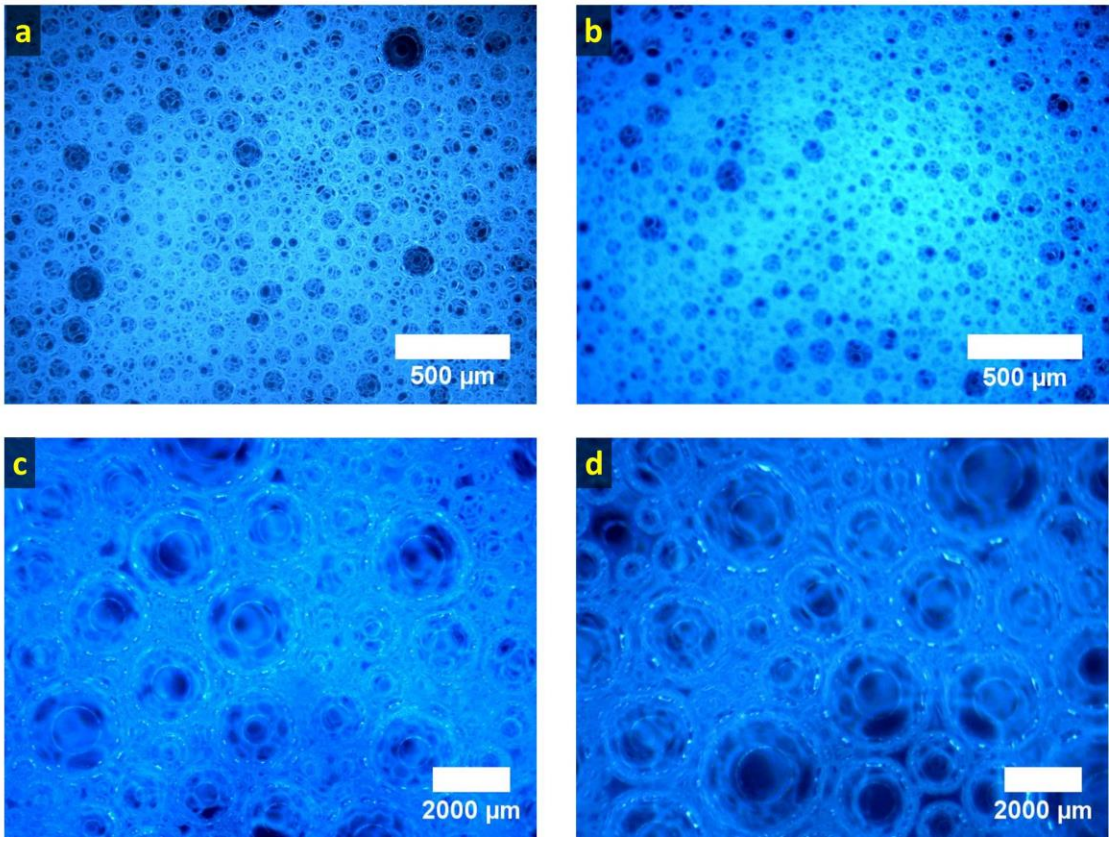

Figure 3.7: Foam texture of 80% quality foam at (a,c) $\bar{X}$ = 0.25 and (b,d) $\bar{X}$ = 0.75

3.4.3.2 Pressure Drop Analysis

Foam rheology in both bulk and porous media is a strong function of the pressure (Holt et al., 1996). In this study, proppant-free foams of different qualities were injected with different injection rate and steady-state pressure drop across the cell was measured. Table 3.3 lists the results of these different cases. As expected, the observed pressure drop across the cell was very low and was less than 0.6 psi and 2 psi for 70% and 80% cases, respectively. Note that pressure drops due to pipe fittings and valves also contribute to

these values. Since these pressure values are very low, they were not used for quantifying and comparing foam rheologies of different cases.

Table 3.3 Entrance pressure for proppant free tests

Foam Quality	Injection Rate (ml/min)	Nominal Shear Rate (1/s)	Pressure Drop (psi)
70%	250	42	0.3
70%	500	84	0.5
70%	840	140	0.6
80%	250	42	0.8
80%	500	84	1.5
80%	840	140	2.0

3.4.3.3 Injection Rate Validation

Foam is a compressible fluid and thus injection rate could vary with the injection pressure conditions. However, since the expected pressure drops (Table 3.3) were low in the present study, it could be treated as an incompressible fluid. To further validate this, foam was injected from the left in the cell at two different qualities using the peristaltic pump at 250 ml/min injection rate (equivalent to 42 s^{-1} shear rate) and the foam front was tracked using a video camera. Figure 3.8a and b shows the contour of foam fronts at different times for 70% and 80% quality, respectively. The x- and z-axis are the normalized slot length in x and z direction. The volume of foam injection was calculated by the area coverage of the foam in the slot using Fiji software, and the data were plotted in Figure 3.9. The slopes, which will give the average injection rates, were found to be 256 ml/min and 249 ml/min for 70% and 80% cases, respectively. These rates were very close to injection rate of the pump i.e. 250 ml/min. This shows that the pump could inject the foam at

specified rates. The same was validated for the other injection rates used in the present study.

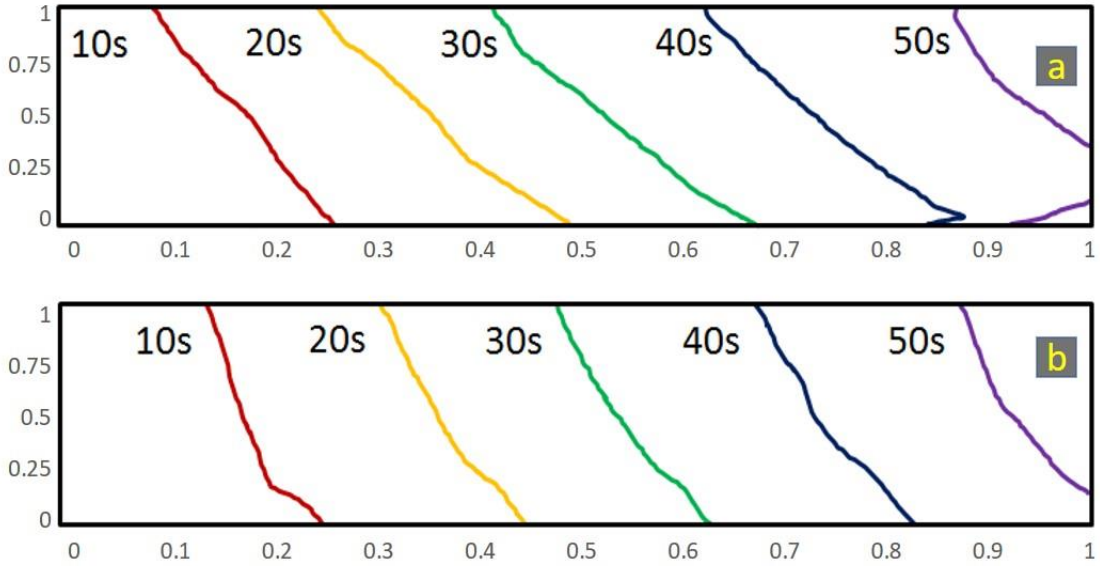

Figure 3.8: Contours of foam front at different injection times for (a) 70% quality foam, (b) 80% quality foam

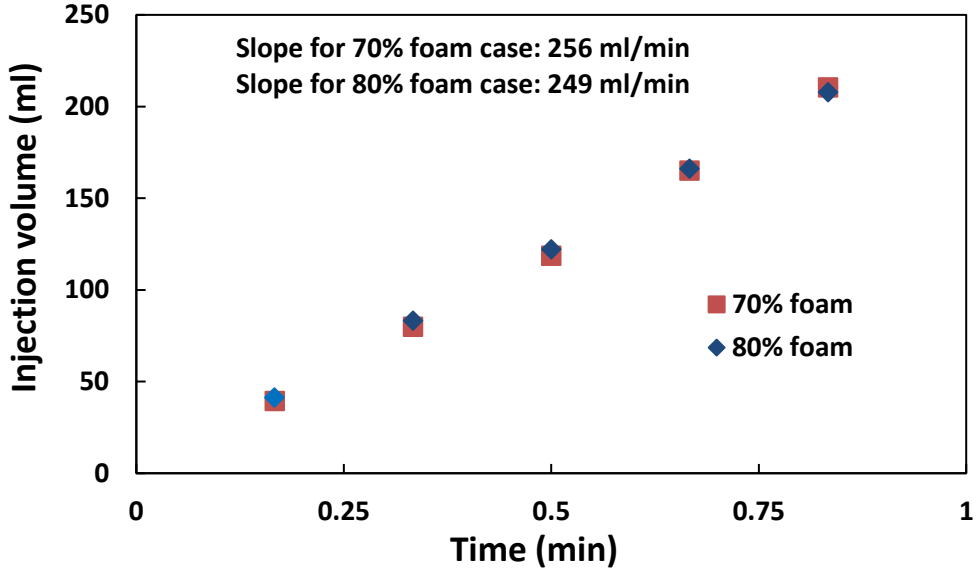

Figure 3.9: Plot of injection volume (based on image analysis of foam in the Hele-Shaw cell) vs. time

3.4.4 Proppant Transport

In this study, 80% quality foam is considered as the base case, and a typical proppant transport pattern in 80% quality foam is shown in Figure 3.10. Four zones are generally observed in the slot during proppant transport in foam: a thin proppant-lean zone at the top due to proppant settling, a proppant-rich foam zone in the middle, a foam-rich (proppant lean) zone towards the bottom and a thin settled-proppant bed zone at the very bottom of the fracture. The bottom foam-rich (proppant lean) zone tends to migrate upward in the form of fingers into the proppant-rich foam zone due to gravitational forces. As the fingers move upward, the proppant surrounding them are pushed away similar to immiscible displacements. The proppant on top of the fingers could move upward, and the proppant along the two sides of the fingers would settle faster compared to those in the finger-free zone. There are possibly two causes for finger generation. First, a foam-rich layer at the bottom is formed due to liquid separation at the inlet. Second, as proppants drop out of the slurry to form a proppant bed at the bottom of the fracture slot, the excess foam would merge to form fingers. This phenomenon could generate pillars of proppant-free zones (Gomaa et al., 2016).

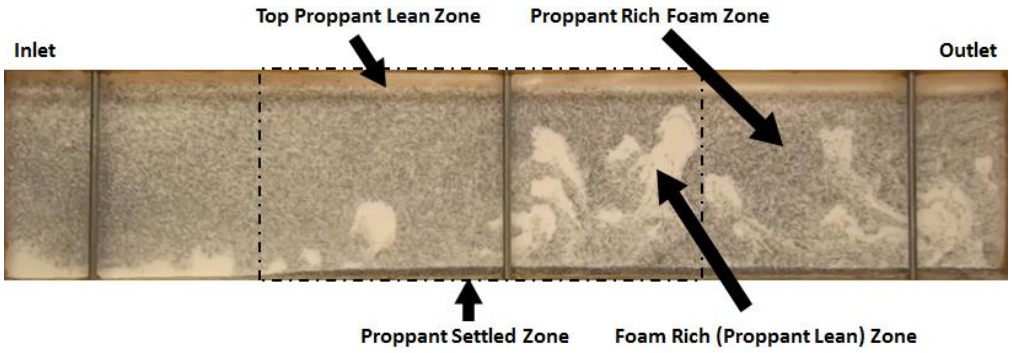

Figure 3.10: Typical proppant transport pattern in 80% quality foam

Proppant trajectories were tracked in a video analysis software, and their velocity was calculated. The tracked proppants were chosen in the center region of the slot (dashed line region in Figure 3.10) to avoid entrance and outlet effects. In all cases, the slurry at the bottom of the slot moved faster than those in the top and middle section. Therefore, the proppants were selected from the middle to the bottom of the slot to better understand the velocity variation due to sampling positions. Additionally, proppants around the fingers were avoided because their velocity could vary significantly due to the movement of the fingers. Figure 3.11 shows typical movements of a tracked proppant in horizontal (x) and downward vertical (z) directions, and it shows that both proppant x and z velocities are approximately constant with respect to time. In all 80% foam cases, foam significantly decreased gravity settling of proppants compared to that of water. Unlike a continuum non-Newtonian fluid, the force exerted on the proppant by the foam could be categorized into two components: a drag force due to the bulk movement of the fluid and an elastic force due to foam compressibility and lamella movement. Therefore, foam is more effective than continuum viscous fluids in terms of carrying proppants.

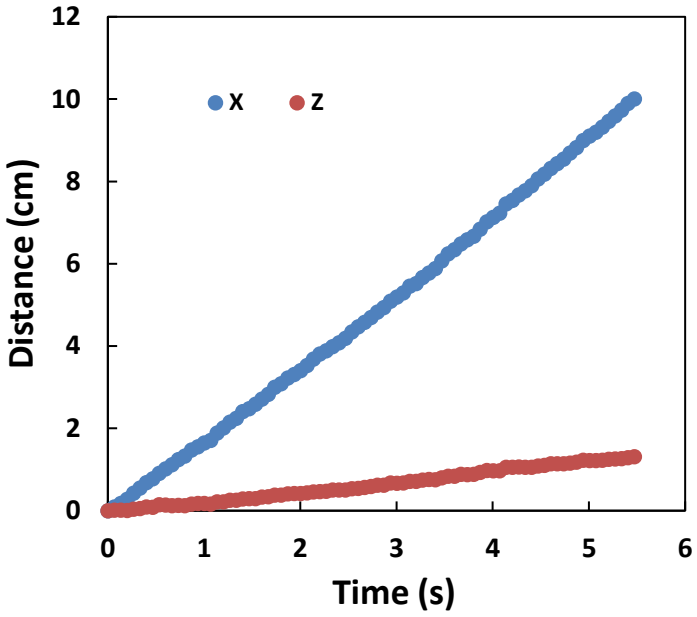

Figure 3.11 Proppant movement in 80% quality foam

3.4.4.1 Effect of Foam Quality

As the foam quality increases, the viscosity of the foam increases (as shown in Figure 3.5) and the lamella structure changes. Both affect proppant settling. When foam is dry, the liquid lamellas are better defined, and proppant could be nicely trapped by these microstructures with negligible settling. When foam is wet, the liquid portions in between the gas bubbles get bigger, some of the proppants do not interact with interfaces and settle faster. Figure 3.12 shows the proppant distribution at the end of injection for cases 3.1, 3.13, 3.9 and 3.15. Cases 3.1 and 3.13 were conducted at a low shear rate, but have the same parameters except for the foam quality. Cases 3.9 and 3.15 were conducted at a high shear rate, with the same parameters except for the foam quality. For dry foam (80% quality) cases (cases 3.1 and 3.9), very little proppant settled down and most of the proppant

flowed out of the slot. For wet foam (70% quality) cases (case 3.13 and 3.15), proppant settled very quickly and formed a proppant bed at the inlet entrance, which is very similar to that of slickwater slurry (Woodworth and Miskimins, 2007). Additionally, clear foaming solution accumulated near the outlet, which is partly due to severe liquid draining at the outlet well when the foam is wet. The local foam quality was smaller than 70% at the lower section of the slot, which could lead to lower foam viscosity and faster proppant settling.

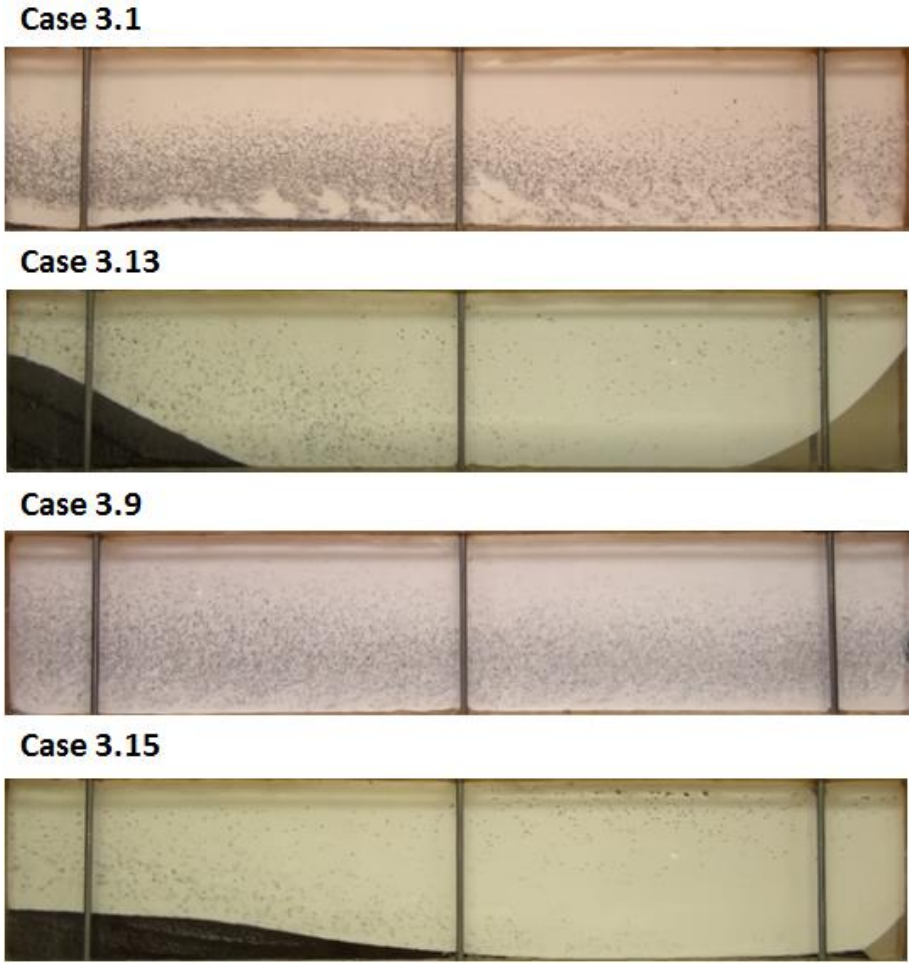

Figure 3.12 Effect of foam quality for cases with 2.5 vol% proppant loading: low shear rates (Case 3.1: 42 s-1 in 80% foam vs. Case 3.13: 42 s-1 in 70% foam), high shear rates (Case 3.9: 140 s-1 in 80% foam vs. Case 3.15: 140 s-1 in 70% foam)

3.4.4.2 Effect of Shear Rate

Figure 3.13 shows the proppant distribution in the fracture slot for cases 3.1, 3.5 and 3.9. All parameters are kept constant except for the shear rate. The slurry was injected from the left in the empty slot filled with air. Two interesting observations were made from Figure 3.13. First, more fingers were observed at lower shear rate (case 3.1). This is because there is more time for fingers to grow. Second, at the lowest shear rate, a small proppant bed forms; there are no proppant beds at the higher shear rates. There could be two possible reasons for these phenomena. First, as the foam moves faster, proppants have less time to settle before flowing out of the slot. Additionally, greater drag force is exerted on the proppants with faster foam, and this force can mobilize settled proppants and limit the size of the proppant bed. Second, as the fingers move upward, proppants along the two sides of the fingers tend to settle down faster. Therefore, in low shear rate scenario (case 3.1), the greater size and number of these fingers could result in more settling of proppants and consequently a larger proppant bed.

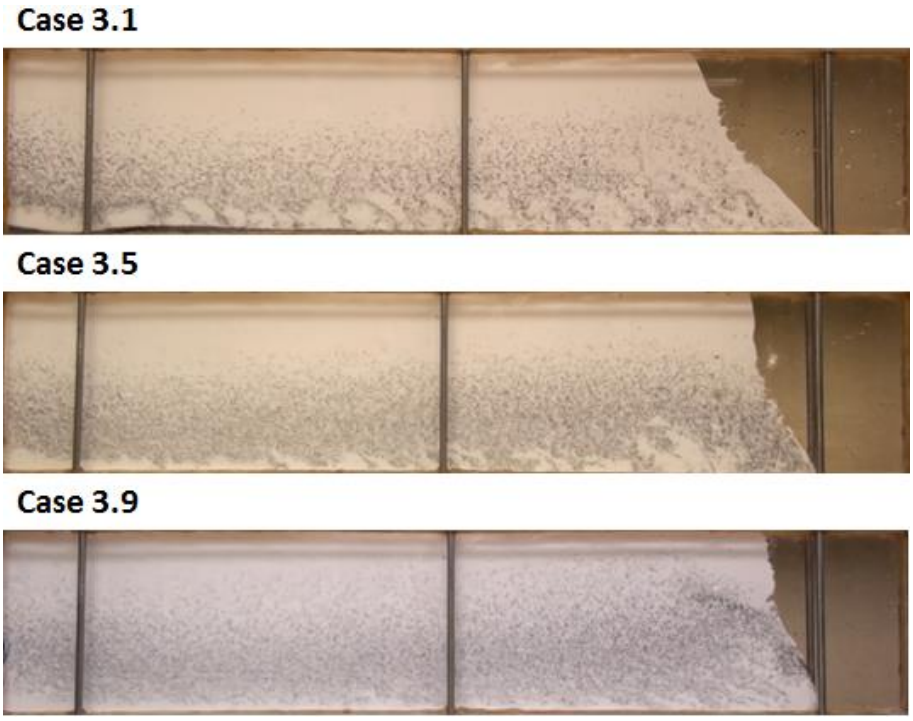

Figure 3.13: Proppant settling in 80% foam with 2.5 vol% proppant; Case 3.1: 42 s-1 shear rate, Case 3.5: 84 s-1 shear rate, and Case 3.9: 140 s-1 shear rate

Figures 3.14a and 14b show the proppant settling velocity (V_z) and normalized proppant x-velocity (Vx/Vx_Foam), respectively, against the normalized height of the slot for cases 3.1, 3.5 and 3.9. V_x is the x-velocity of the proppant, and Vx_Foam is the nominal x-velocity of the foam (injection rate / cross-sectional area). No data is shown in the upper section of the slot because the proppants seldom settle down when the normalized height is greater than 0.5. Based on all experiments data (including all loading cases), at the same normalized height, the normalized proppant x-velocity gets smaller as the shear rate increases. Generally, the foam moves faster at the bottom of the slot probably due to lower local foam quality; thus the proppants also flow a little faster at the bottom. In the upper section of the slot, Vz is almost zero and proppants do not settle. The proppants are carried

by the foam lamella very effectively. In the lower section of the slot, most proppants settle (negative Vz). In addition, proppant settles faster as the shear rate decreases as shown in Figure 3.14b. For some proppants, the settling velocity is slightly positive, which means some proppants move slightly upward. Proppants moved upwards due to the complex flow pattern created by the foam fingers and the foam drainage process. To illustrate this, a few snapshots are shown in Figure 3.15. As the liquid phase drains down, the foam bubbles move upward and could drag the proppant upward. Figure 3.16a shows V_z as a function of the normalized proppant x-velocity. It could be observed when the normalized proppant x-velocity is less than 0.9, proppants settle very slowly or even move upward. If we assume the proppant x-velocity is equal to the local foam x-velocity, then we could calculate the local apparent viscosity with the correlations shown in Figure 3.5. In Figure 3.16b, it indicates proppant settles slower if the nominal shear rate is higher, and there are two possible mechanisms for this phenomena. First, a faster foam limits the growth of the foam fingers which could lead to greater settling to adjacent proppant; second, the foam quality is more uniform in a faster (or higher shear rate) foam due to less time for drainage process.

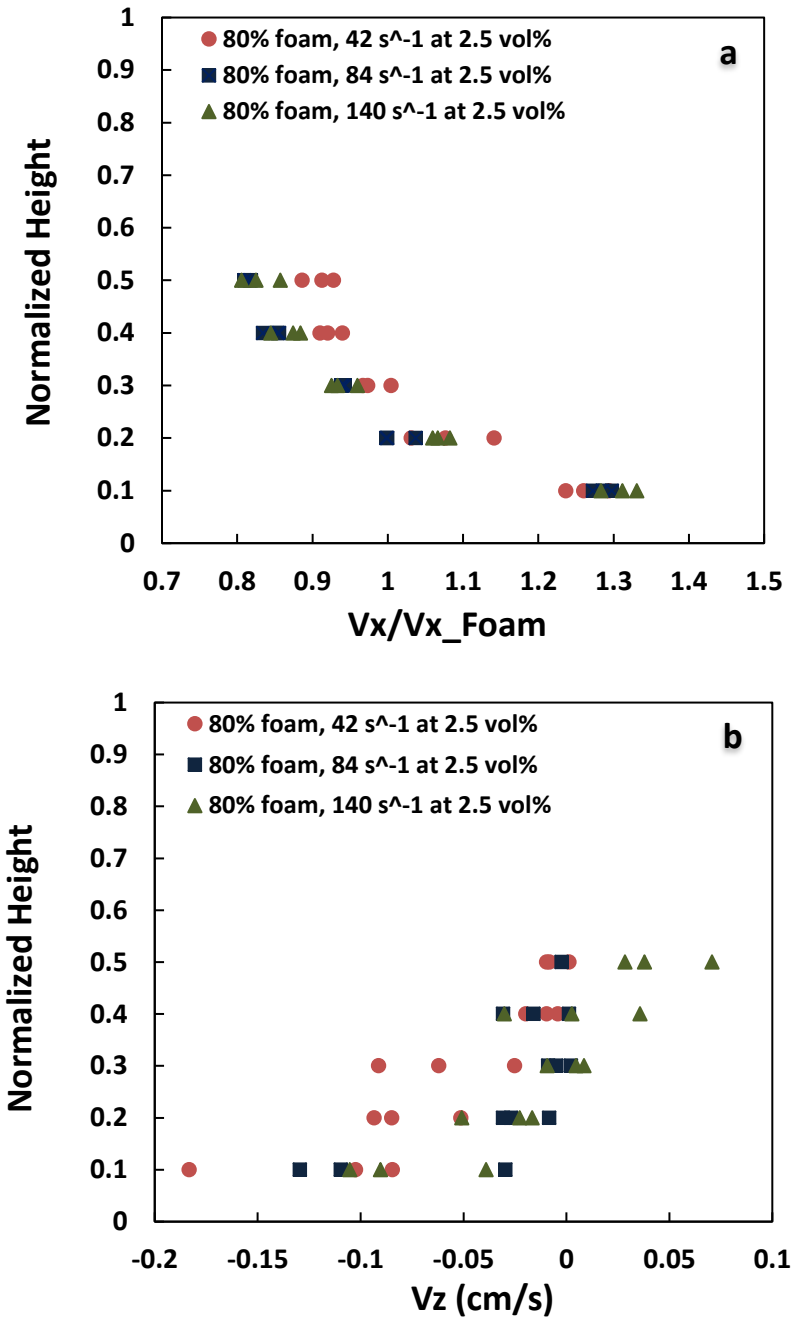

Figure 3.14: Effect of nominal shear rate on proppant settling velocity in 80% foam with 32.5 vol% proppant (a) normalized horizontal velocity, (b) vertical velocity

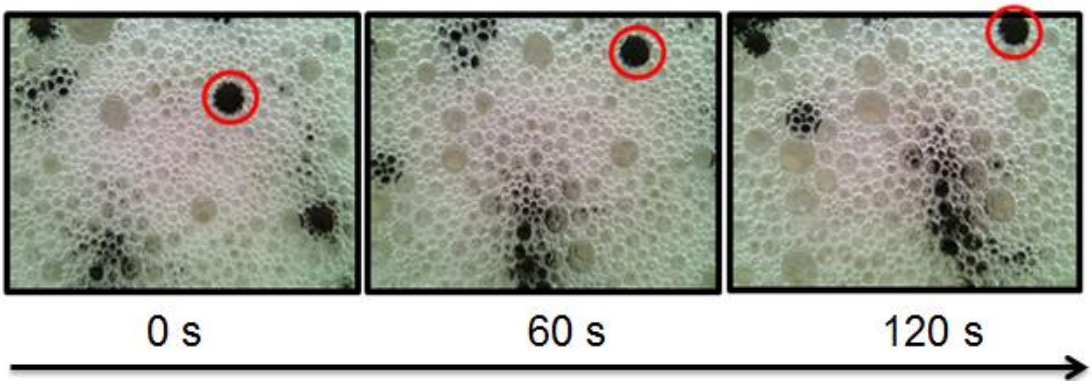

Figure 3.15: Upward proppant movement due to liquid drainage

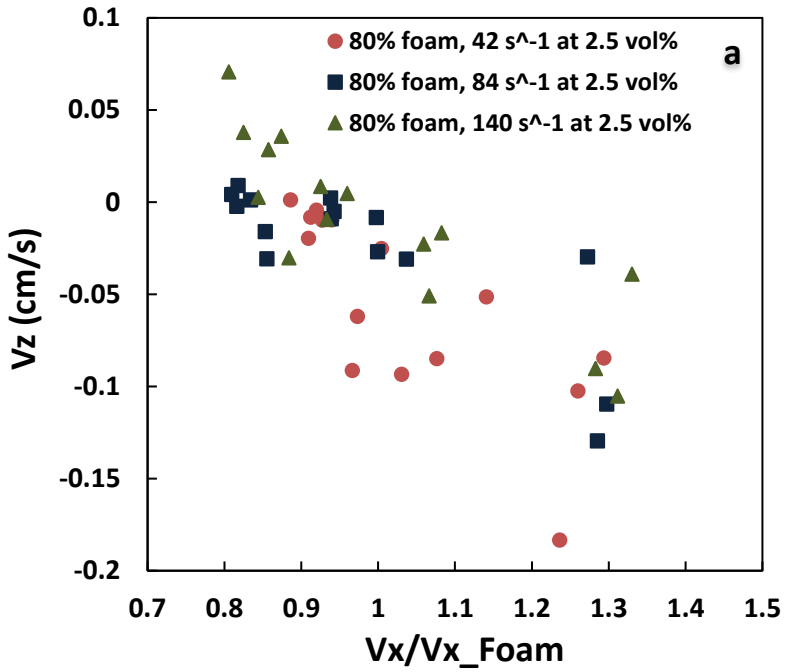

Figure 3.16: Effect of nominal shear rate on proppant settling velocity in 80% foam with 2.5 vol% proppant (a) Vz vs. normalized Vx, (b) Vz vs. nominal foam viscosity

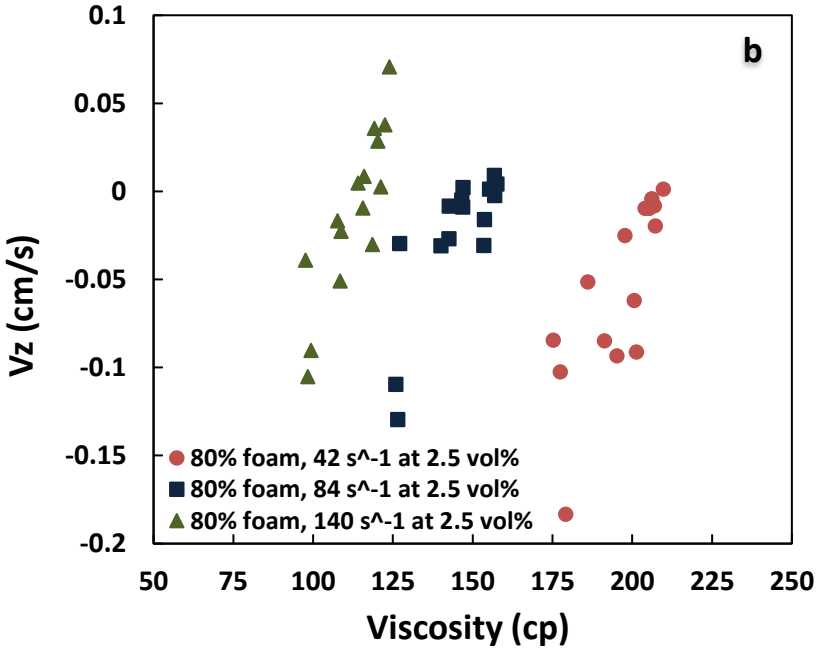

Figure 3.16: Continued

Figure 3.17 shows the proppant distribution at the end of injection for 70% quality foam cases 3.13 – 3.15. As shear rate increases, the proppant bed gets shorter (in height) and longer. The surfactant water drains slowly towards the bottom of the slot and lowers the foam quality. Proppants settle in a way similar to slick water at the bottom. Figure 3.18 shows the vertical and horizontal velocities of some of the proppants not yet settled into the proppant bed. The settling velocity ranges from 0.8 cm/s to 2.1 cm/s, and these values are significantly larger than those in 80% foam cases. It was difficult to measure the velocity value against normalized height because proppant bed formed very quickly during the experiments.

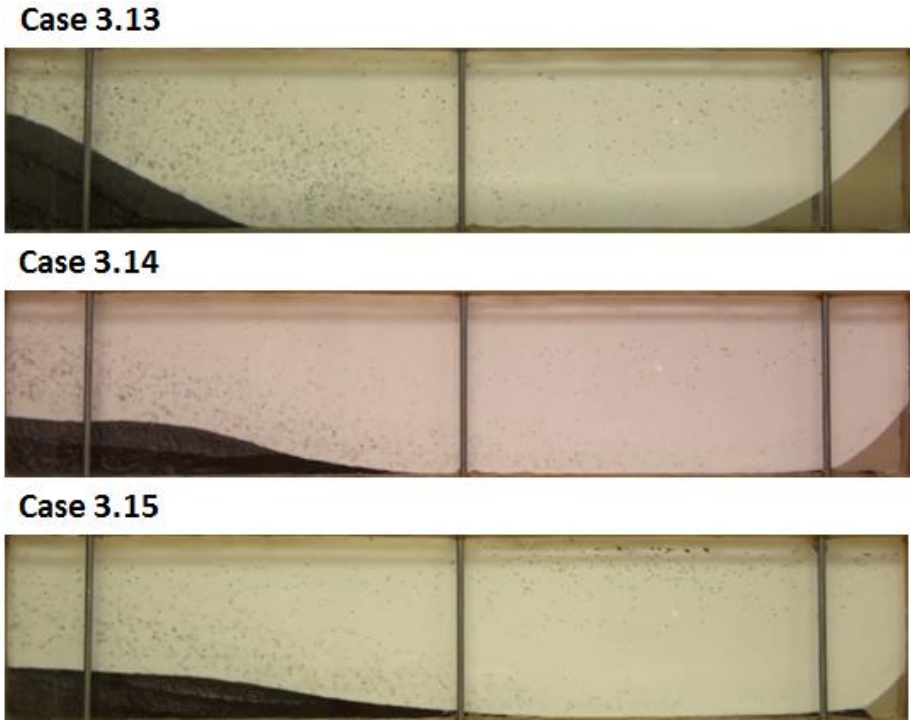

Figure 3.17: Proppant settling in 70% foam with 2.5 vol% proppant; Case 3.13: 42 s-1 shear rate, Case 3.14: 84 s-1 shear rate, and Case 3.15: 140 s-1 shear rate

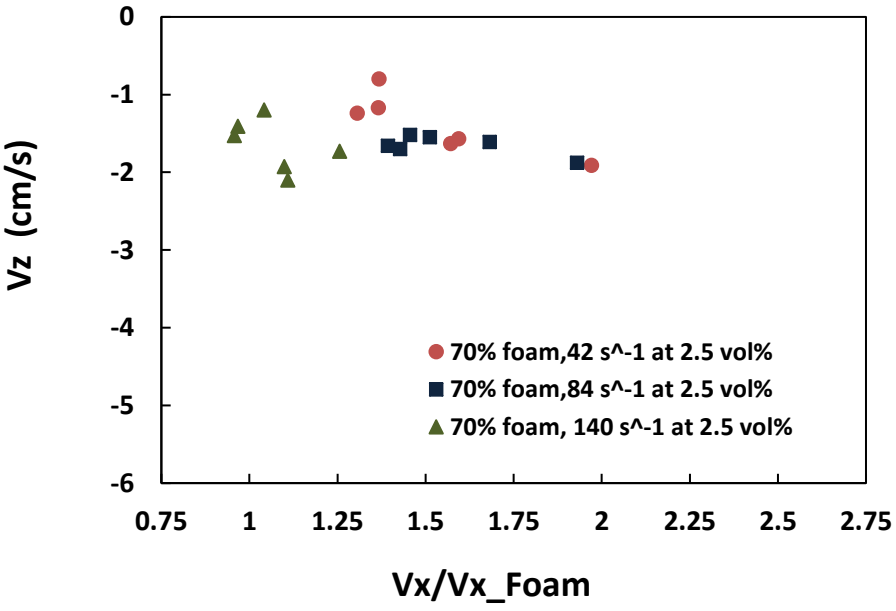

Figure 3.18: Effect of nominal shear rate on proppant settling velocity in 70% foam with 2.5 vol% proppant

3.4.4.3 Effect of Proppant Loading

Figure 3.19a and 19b show the proppant settling velocity (Vz) and normalized proppant horizontal velocity against normalized height for cases 3.5 to 3.8, respectively. Proppant loading is varied keeping other parameters constant. According to Figure 3.19a, the proppant loading does not have a significant impact on the normalized proppant x-velocity profile. According to Figure 3.19b, in the middle of the slot, the settling velocity is almost zero; there is no settling of proppants. In the bottom of the slot, the settling velocity magnitude and its variations are larger for the dilute proppant loading cases (2.5 and 5.0 vol%) than those of dense cases (7.5 and 10.0 vol%). This indicates that as proppant loading increases (below a threshold value above which proppants significantly damage the microstructure of the foam), the foam microstructure and adjacent proppants hinder proppant settling. Figure 20a shows V_z as a function of the normalized proppant x-velocity. It could be observed in Figure 20a, as the normalized proppant x-velocity increases, proppant settles faster with a larger variation in settling velocity magnitude. According to Figure 20b, at the same apparent foam viscosity, proppant settles slower with a smaller variation in settling velocity magnitude as the loading increases. Based on these observations, at typical field proppant loading range, the foam could effectively carry the proppants at 80% quality.

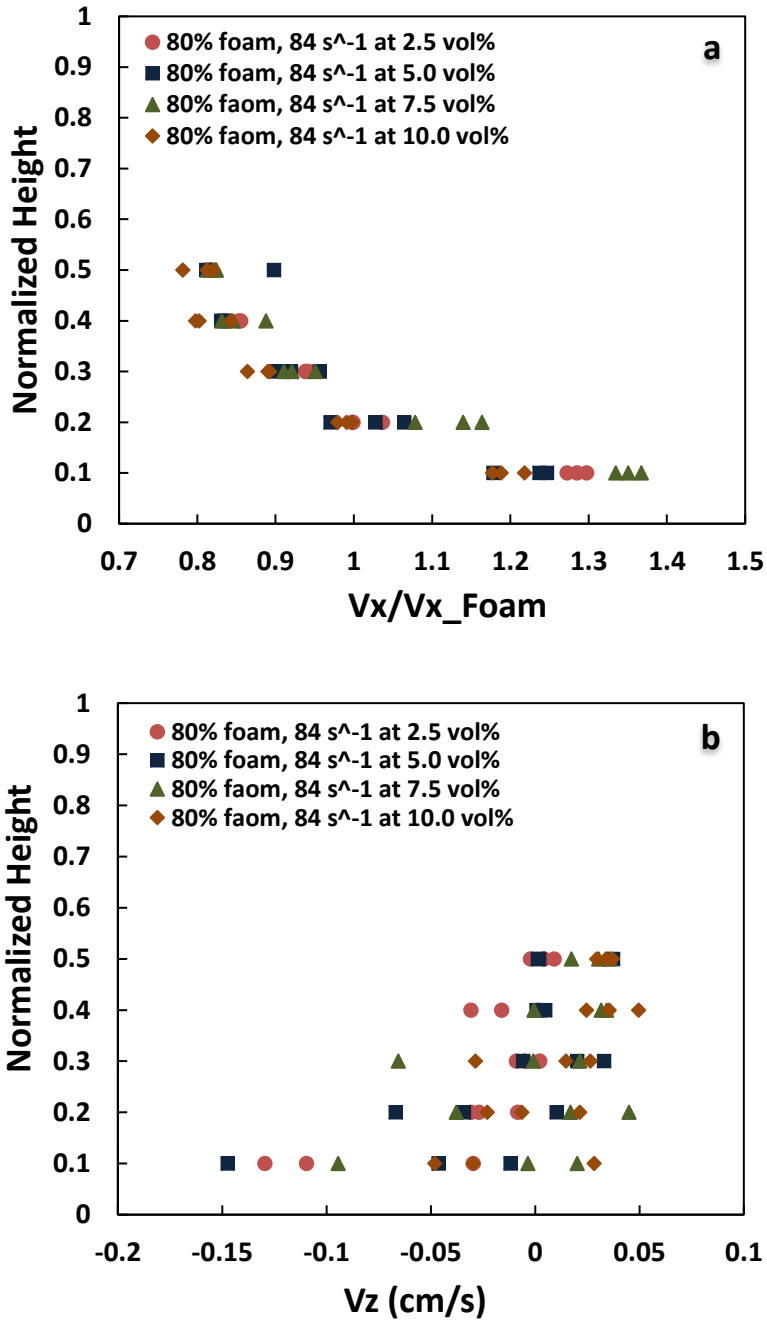

Figure 3.19: Effect of proppant loading on proppant settling velocity in 80% foam at 84 s-1 (a) horizontal velocity (b) vertical velocity as a function of vertical position

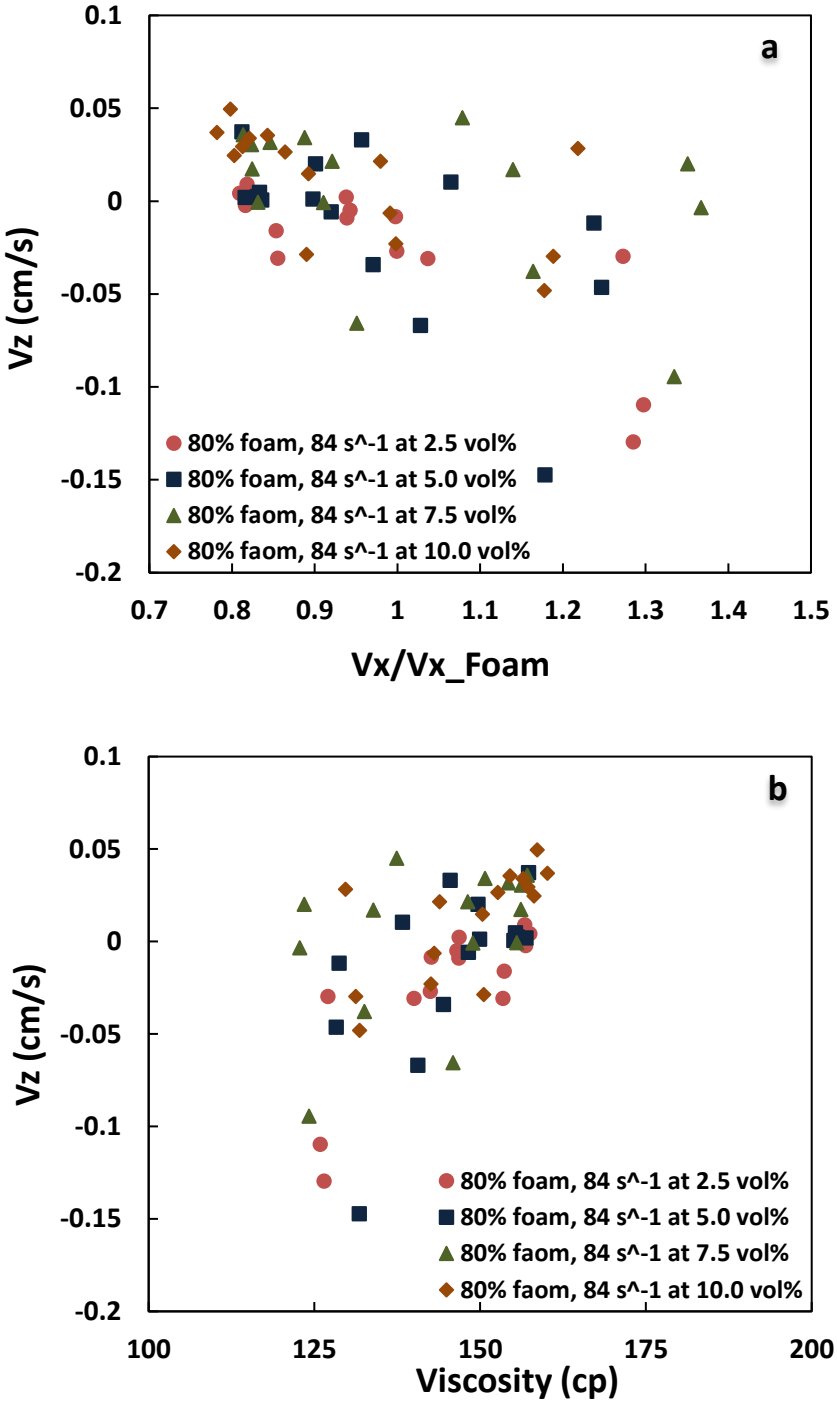

Figure 3.20: Effect of proppant loading on proppant settling velocity in 80% foam at 84 s-1 (a) Vz vs. normalized Vx, (b) Vz vs. nominal foam viscosity

Figure 3.21 shows the proppant distribution at the end of injection for 70% foam cases 3.15 – 3.17. As proppant loading increases, the proppant bed height grows. Figure 3.22 shows the velocity data for these three cases, and the existence of a big proppant bed leads to a larger value of Vx/Vx_Foam as less cross-sectional area is available for proppant and foam flow. The magnitude of settling Vz velocities are large (1-5 cm/s) compared to those in 80% quality foam cases (0.05 cm/s). Proppants settle slower when the loading increases.

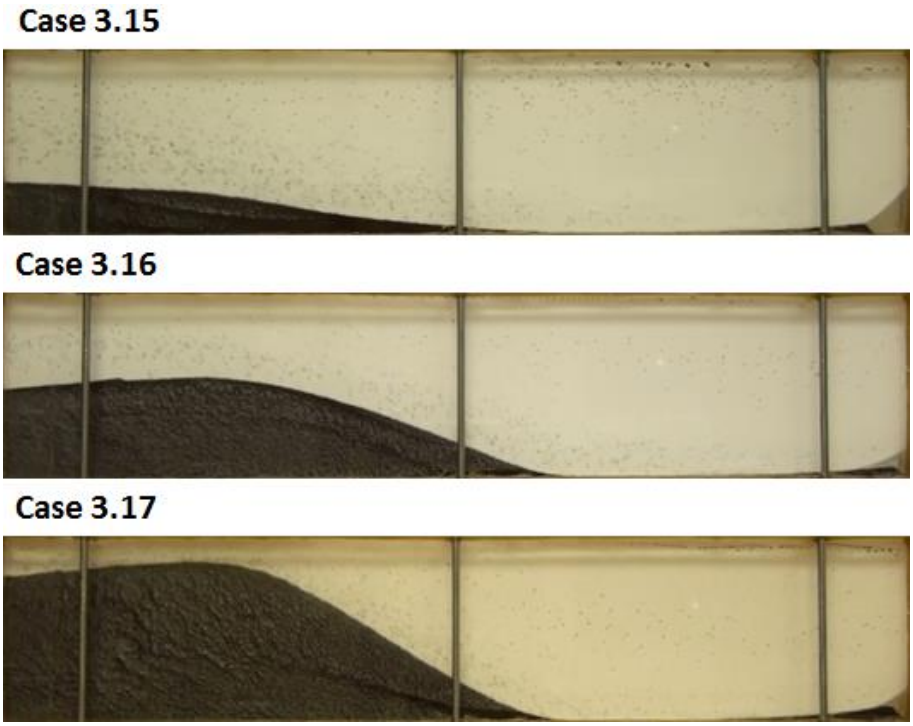

Figure 3.21. Comparison of proppant loading for 70% foam cases at 140 s-1 shear rate; Case 3.15: 2.5 vol%, Case 3.16: 5.0 vol%, and Case 3.17: 7.5 vol%

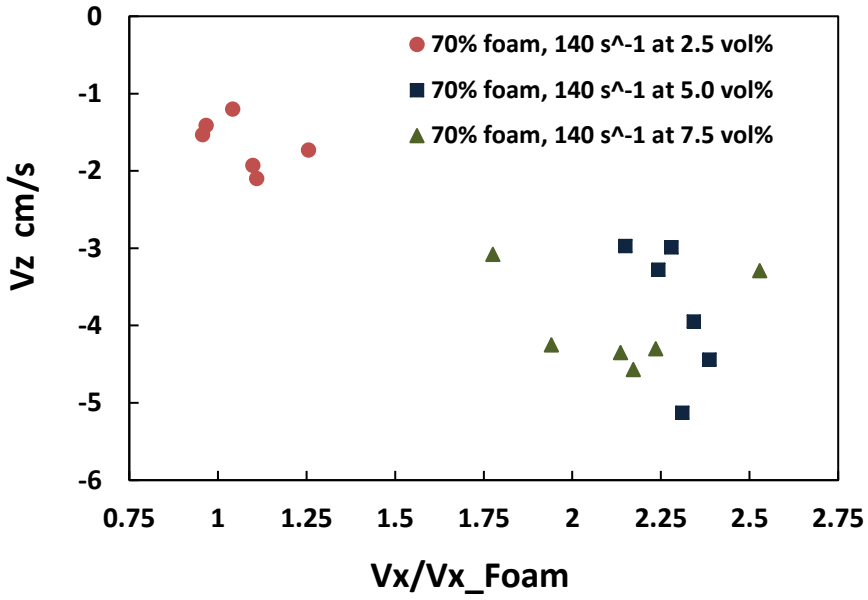

Figure 3.22. Effect of proppant loading on proppant settling velocity in 70% foam at 140 s-1: Vz vs. normalized Vx

Figure 3.23 compares the settling velocity for experimental proppant particles with the theoretical Stokes settling velocity. The symbols represent the experimental data. Velocities are directly measured; corresponding viscosities are estimated from the shear rate associated with the local foam velocity (which is approximated by the Vx of the proppant being studied). The red and dashed black curves represent the velocity estimated from Stokes equation,

$$Vz = \frac{d^2 g \Delta\rho}{18\mu}, \tag{3.10}$$

assuming that the proppant diameter is 600 μm (average size for 20-40 mesh) and the density of 80% and 70% quality foams, respectively. Note that the density difference of the two foams does not make a significant difference in the proppant settling velocity. The green dashed curve represents the Stokes velocity for the smallest proppant in the 20-40

mesh in 70% foam and the blue dashed curve for the largest proppant in the 20-40 mesh. It could be observed that all the experimental proppant velocities (the magnitudes) in the 80% foam are very small (mostly less than 0.1 cm/sec); these velocities are smaller than the calculated Stokes velocity for the average proppant in 80% foam; they do not follow Stokes law. However, the proppants in 70% foam do follow the Stokes law. This is because in dry 80% foams, a proppant is typically trapped between a set of bubbles, primarily moves with this set of bubbles with little vertical settling, and does not experience the effective viscosity of the foam. However, in 70% foam, proppants settle in the liquid between the bubbles while being hindered by many interfaces, and experience the effective viscosity of the foam.

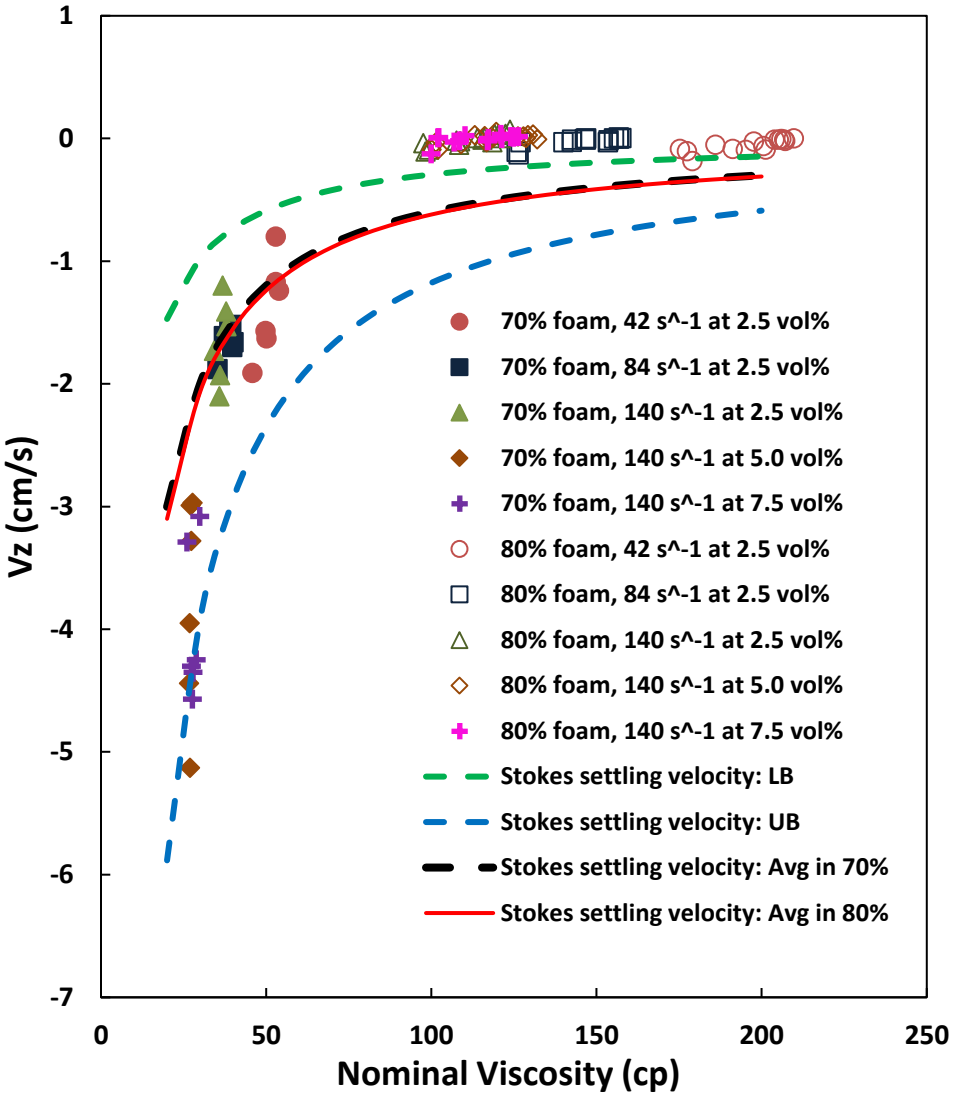

Figure 3.23: Comparison of vertical settling velocity of proppant particles with those from Stokes equation; velocity is shown for average particle size in 70% and 80% foams as well as the velocity for the smallest particle (LB) and the largest particle (UB)

3.5 CONCLUSIONS

In this chapter, proppant transport in foam-based fracturing fluid is visualized in a laboratory-scale fracture slot. Effects of parameters like foam quality, proppant loading,

and injection rate are systematically investigated. The following conclusions are reached in this chapter.

1. Strong liquid drainage happens in wet foams (70% nominal quality), and this leads to poor proppant placement and a proppant bed formation at the fracture entrance. The height of the proppant bed decreases as the shear rate increases and the proppant loading decreases.

2. Dry foams (80% nominal quality) can carry proppants between lamellas with little vertical settling. Proppants settle with a very low velocity only at the bottom of the fractures, and settling velocity of proppants is almost zero in the middle of the fractures.

3. Liquid drainage can alter local foam quality in the vertical direction, and this could lead to the generation of an x-velocity profile along the vertical direction.

4. In dry foams, higher shear rates do not lead to faster settling proppants. Indeed, the microstructures of dry foams dominate the settling of proppants other than the effective viscosity of the foam fluids. As the proppant loading increase, the proppant settles slower, and this is probably due to hindered settling.

5. Complex flow patterns are developed in dry foams due to protrusion of foam fingers into proppant laden foam. The formatin of the fingers indicate mechanical entrapment of proppants by surrouding bubbles.

NOMENCLATURE

w slot width, m

h slot height, m

d diameter of testing tube, m

L length of testing tube, m

q injection rate, m^3/s

γ shear rate, 1/s

μ viscosity, cp

ΔP pressure difference, pa

τ stress, pa

n power law index, no unit

K consistency index, Ns^n/m^2

Chapter 4: Dense Discrete Phase Modeling of Proppant Transport: A Computational Fluid Dynamics Approach

4.1 SUMMARY

Proppant transport in a single fracture has been widely simulated with different methods, and recently a Computational Fluid Dynamics (CFD) model was used to study proppant transport in fracture networks. However, there is no study on benchmarking a model against laboratory data. The objective of chapter 4 is to develop a fully 3D CFD model to match experimental cases studied in chapter 2. A hybrid Eulerian-Lagragian CFD model, Dense Discrete Phase Model (DDPM), has been developed in this chapter. This model can qualitatively match several key physical observations (shown in chapter 2) including: three-zone transport, proppant bed shape, proppant residence time and generation of vortex; it also quantitatively matches the values of bypass/total ratios observed in experiments. However, this model also has its limitations, as it works for dense, slow moving systems, but fails for dilute and fast-moving systems.

4.2 INTRODUCTION

Fracture propagation in naturally fractured shale reservoirs and the formation of complex fracture networks have been widely studied in the geomechanics field (Fu et al., 2012; McClure et al., 2015; Weng et al., 2011; Wu and Olson, 2015). However, the understanding of proppant transport into secondary fractures from a primary fracture is poorly understood. Generally, there are two main approaches to simulate particle-laden fluid flow: Eulerian-Eulerian (E-E) approach and Eulerian-Lagrangian (E-L) approach. The Eulerian before the hyphen indicates that a fixed coordinate is used to calculate the flow of the fluid. The Eulerian after the hyphen indicates a fixed coordinate is used to

This chapter is based on (Tong and Mohanty, 2016). Dr. Mohanty supervised the project.
Tong, S., Mohanty, K.K., 2016. Proppant transport study in fractures with intersections. Fuel 181, 463–477

calculate the movement of the particles. The E-E approach treats the particle phase as a pseudo-continuum fluid phase, and only the volume concentration of the particle phase is calculated. The Lagrangian after the hyphen indicates that a moving coordinate is used to track the movement of the particles. The E-L approach treats the particles as discrete elements or points and tracks the moving trajectories of the particles.

The E-E approach is the most widely used approach in the literature (Gu and Mohanty, 2014; Kong et al., 2016; Liu and Sharma, 2005; Ribeiro and Sharma, 2013; Shiozawa and McClure, 2016). Liu (2005) developed a correlation for two-dimensional (2-D) proppant flow with fracture roughness based on their lab results. An empirical factor called retardation factor was proposed to correct the horizontal and vertical velocity of proppants inside a fracture. Even though this pioneering work has been widely referenced and applied by other researchers (Gu and Mohanty, 2014; Ribeiro and Sharma, 2013), it is not able to handle a fully 3-D geometry such as a fracture network. Shiozawa (2016) incorporated a more sophisticated proppant transport model (Dontsov and Peirce, 2015) into a 3-D field scale complex fracturing simulator to simulate proppant distribution in a fracture network system (McClure et al., 2015). However, their simulator only tracks the proppant concentration profile in a 2-D manner without considering any inertial effect as the proppants flow across a junction between fractures. Hence, the proppant distribution is not accurate. To summarize, most of the commercial fracturing simulators fall into the E-E approach, and they generally use an effective viscosity of particle suspension to account for slurry rheology. However, they are too simplified and the effect of particles at concentrated conditions (such as reaching to packing limit and forming a proppant bed) is neglected.

Computational Fluid Dynamics (CFD) has been used widely to model particle transport in many applications (Armstrong et al., 2010; Lu and Agrawal, 2014). There are

two widely used multiphase models in CFD: Eulerian-Granular model which is an Eulerian-Eulerian approach, and Discrete Phase Model (DPM) which is an Eulerian-Lagrangian approach. The Eulerian-Granular model comes from incorporating the kinetic theory of granular flow (KTGF) for particle transport (Ding and Gidaspow, 1990). KTGF is one of the most significant theories for simulating particle flow. Granular temperature, which accounts for the random motion of particles, is the key concept of this theory. Energy dissipates during random collisions between particles. This approach treats all the phases as interpenetrating fluid continuums in an averaging scheme, and therefore it is also known as the two-fluid model (TFM). One advantage of this averaging scheme is the incorporation of a large number of particles because the computation cost does not correspond to the number of particles. Lu et al. (2014) adopted this approach to study sand erosion problems in multiphase-flow systems. They stated that the Eulerian-Granular model works from dilute to highly concentrated systems, and gives more accurate erosion prediction than the Eulerian-Lagrangian approach. The disadvantage of this model is three-fold. First, it cannot track individual particle trajectory due to the averaging scheme. Second, the particle-wall interaction is not well captured. Third, a uniform particle size is assumed.

The DPM approach assumes that particles do not interact with each other, and therefore it only can be employed if the volume fraction of the particles is low (less than 10%). It treats the carrier phase as a continuum by solving the Navier Stokes (N-S) equation and tracks the discrete phase as individual particles by coupling them with the flow field. Proppant transport and distribution in a single stage of plug-and-perf completion has been simulated with DPM and successfully matched against experimental data (Bokane et al., 2013; Zhang and Dunn-Norman, 2015). The DPM can include proppant size distribution and trajectory, but fails when proppants settle and form a bed.

The DPM (Eulerian-Lagragian) approach can be extended to a high solid phase loading if coupled with a Discrete Element Method (DEM) (Blyton et al., 2015; Kou et al., 2018; Mondal et al., 2016; Sun et al., 2016; Tomac and Gutierrez, 2013). In a DEM-CFD method, the motion of discrete particles is obtained by applying Newton's law of motion to all particles, therefore the inter-particle and particle-wall interactions are well captured. The flow of continuum fluid is described by the local averaged N-S equation in CFD module. Tomac et al. (2013) included lubrication forces into the DEM-CFD method, and simulated proppant flow in a thin fracture. They concluded the size ratio between proppant diameter and fracture width affects the flow significantly. Moreover, the lubrication effect plays a big role at larger proppant loadings, larger fluid viscosities and lower pressure gradients. This method treats the particles individually and therefore is more rigorous, which also results in high computational costs and limits its application for large-scale simulations.

Recently, a hybrid version of Eulerian-Lagrangian model, multi-phase particle-in-cell (MP-PIC) (Andrews and O'Rourke, 1996; Snider, 2001) has been proposed to simulate proppant transport (Tsai et al., 2013; Zeng et al., 2019). This method avoids the search of colliding particles by calculating particle−particle interactions based on a Eulerian particle stress model. In addition, MP-PIC lumps many particles into a single parcel for faster calculation. However, the stress model would lead to unphysical results and needs to be improved according to previous studies (Liang et al., 2014; Lu et al., 2017).

In this study, an improved version of MP-PIC, Dense Discrete Phase Model (DDPM), (Pirker et al., 2010) is adopted. In this model, the fluid phase is solved as a continuum on the Eulerian grid while the particle phase is tracked in a Lagrangian approach. However, the particle phase is mapped back to the Eulerian grid (Snider, 2001). DDPM groups particles in parcels and these parcels are treated as points without direct

inter-particle interactions. The concentration of the particles is calculated by mapping the volume occupied by all particles in a parcel onto the Eulerian grid and the particle-particle interactions are computed from the Kinetic Theory of Granular Flow (KTGF) in this approach (Ding and Gidaspow, 1990). Due to the Lagrangian tracking scheme in DDPM, it is possible to include a particle size distribution and the interaction between wall and particles.

4.3 METHODOLOGY

4.3.1 Model Equations

DDPM is a hybrid model of the discrete phase model (DPM) and the two-fluid model (TFM). In the standard DPM method, parcels (a group of particles) are tracked in a Lagrangian approach by applying Newton's law of motion to parcels. However, DPM assumes particle loading to be low and the volume fraction of particles is not considered. In DDPM, a set of conservation equations (Ding and Gidaspow, 1990) from TFM is solved to overcome this problem.

From mass conservation:

$$\frac{\partial}{\partial t}\left(\alpha_f \rho_f\right) + \nabla \cdot \left(\alpha_f \rho_f \overrightarrow{v_f}\right) = 0 \tag{4.1}$$

$$\frac{\partial}{\partial t}\left(\alpha_s \rho_s\right) + \nabla \cdot \left(\alpha_s \rho_s \overrightarrow{v_s}\right) = 0 \tag{4.2}$$

From momentum conservation:

$$\frac{\partial}{\partial t}\left(\alpha_f \rho_f \overrightarrow{v_f}\right) + \nabla \cdot \left(\alpha_f \rho_f \overrightarrow{v_f}\overrightarrow{v_f}\right) = -\alpha_f \nabla p + \nabla \cdot \bar{\bar{\tau}}_f + \alpha_f \rho_f \vec{g} + \beta(\overrightarrow{v_s} - \overrightarrow{v_f}) \tag{4.3}$$

$$\frac{\partial}{\partial t}\left(\alpha_s \rho_s \overrightarrow{v_s}\right) + \nabla \cdot \left(\alpha_s \rho_s \overrightarrow{v_s}\overrightarrow{v_s}\right) = -\alpha_s \nabla p + \nabla \cdot \bar{\bar{\tau}}_s + \alpha_s \rho_s \vec{g} + \beta(\overrightarrow{v_f} - \overrightarrow{v_s}) \tag{4.4}$$

In DDPM, Eq. (4.4) or the momentum conservation equation of the particle phase is not solved. Instead, particle properties are mapped to the Eulerian grid, and the interactions between flow and particles are computed on the grid. Then the computed properties are mapped back to the particles. The particle motion is computed as:

$$\frac{d\overrightarrow{v_s}}{dt} = \frac{\vec{g}\left(\rho_s - \rho_f\right)}{\rho_s} + F_D\left(\overrightarrow{v_f} - \overrightarrow{v_s}\right) + \vec{F}_{KTGF} \tag{4.5}$$

$$F_D = \frac{18\mu_f}{\rho_s d_s^2}\frac{C_D Re_s}{24} \tag{4.6}$$

$$\vec{F}_{KTGF} = -\frac{1}{\alpha_s \rho_s}\nabla \cdot \bar{\bar{\tau}}_s \tag{4.7}$$

The terms in the right-hand side of Eq. (4.5) come from the force of gravity, drag force, and particle collision from KTGF, respectively. Gidaspow drag model (Ding and Gidaspow, 1990), which works for both dilute and dense system, is adopted:

$$\beta = 150\frac{\alpha_s(1-\alpha_f)\mu_f}{\alpha_f d_s^2} + 1.75\frac{\alpha_s \rho_f \left|\overrightarrow{v_s} - \overrightarrow{v_f}\right|}{d_s}, \quad \text{for} \quad \alpha_s \geq 0.2 \tag{4.8}$$

$$\beta = \frac{3}{4}C_D\frac{\alpha_s \alpha_f \rho_f \left|\overrightarrow{v_s} - \overrightarrow{v_f}\right|}{d_s}\alpha_f^{-2.65}, \quad \text{for} \quad \alpha_s \leq 0.2 \tag{4.9}$$

$$Re_s = \frac{d_s \rho_f \left|\overrightarrow{v_s} - \overrightarrow{v_f}\right|}{\mu_f} \tag{4.10}$$

$$C_D = \frac{24}{\alpha_f Re_s}\left[1 + 0.15\left(\alpha_f Re_s\right)^{0.687}\right] \tag{4.11}$$

In KTGF, the solid shear viscosity (μ_s) includes kinetic ($\mu_{s,kin}$), collisional ($\mu_{s,col}$) and frictional components ($\mu_{s,fri}$), and the three terms correspond to dilute, intermediate and dense systems, respectively. Johnson's frictional viscosity model (Johnson and Jackson, 1987) is adopted in the present study. Bulk viscosity (λ_s) and radial distribution

function (g_o) represent the resistance of particles to deformation and the probability of inter-particle collisions, respectively. Both are calculated with the approach used by Lun (Lun et al., 1984). Solid pressure (p_s) arises from an analogy to kinetic theory of dense gas (Chapman et al., 1990), and it includes kinetic and collisional terms. The closure equations (Ding and Gidaspow, 1990) are listed in Eqs. (4.12) – (4.20).

$$\mu_s = \mu_{s,kin} + \mu_{s,col} + \mu_{s,fri} \tag{4.12}$$

$$\mu_{s,kin} = \frac{10 d_s \rho_s \sqrt{\Theta_s \pi}}{96 \alpha_s g_o (1+e)} \left[1 + \frac{4}{5} \alpha_s g_o (1+e)\right]^2 \tag{4.13}$$

$$\mu_{s,col} = \frac{4}{5} \alpha_s d_s \rho_s g_o (1+e) \left(\frac{\Theta_s}{\pi}\right)^{\frac{1}{2}} \tag{4.14}$$

$$P_{friction} = 0.1 \alpha_s \frac{(\alpha_s - \alpha_{s,min})^2}{(\alpha_{s,max} - \alpha_s)^3} \tag{4.15}$$

$$\mu_{s,fri} = \frac{p_{friction} sin\phi}{2\sqrt{I_{2D}}} \tag{4.16}$$

$$g_o = \left(1 - \left(\frac{\alpha_s}{\alpha_{s,max}}\right)^{\frac{1}{3}}\right)^{-1} \tag{4.17}$$

$$p_s = \alpha_s \rho_s \Theta_s + 2\alpha_s^2 \rho_s \Theta_s g_o (1+e) \tag{4.18}$$

$$k_\Theta = \frac{150 d_s \rho_s \sqrt{\Theta_s \pi}}{384 g_o (1+e)} [1 + \frac{6}{5} \alpha_s g_o (1+e)]^2 + 2\alpha_s^2 \rho_s d_s g_o (1+e) \left(\frac{\Theta_s}{\pi}\right)^{\frac{1}{2}} \tag{4.19}$$

$$\Phi = -3\,\beta \Theta_s \tag{4.20}$$

The phase stress tensors are calculated from:

$$\bar{\bar{\tau}}_f = \alpha_f \mu_f \left(\nabla \overrightarrow{v_f} + \nabla \overrightarrow{v_f}^T\right) - \frac{2}{3} \alpha_f \mu_f \left(\nabla \cdot \overrightarrow{v_f}\right) \bar{\bar{I}} \tag{4.21}$$

$$\bar{\bar{\tau}}_s = \mu_s\left(\nabla\overrightarrow{v_s} + \nabla\overrightarrow{v_s}^T\right) + (\lambda_s - \frac{2}{3}\mu_s)(\nabla \cdot \overrightarrow{v_s})\bar{\bar{I}} \tag{4.22}$$

In Eq. (4.23), the solid pressure term, shear viscous term and bulk viscous term are computed from KTGF according to the conservation of the kinetic energy of moving particles. This quantity is well known as the granular temperature (Θ_s), which has the following conservation equation:

$$\frac{3}{2}\left[\frac{\partial(\alpha_s\rho_s\Theta_s)}{\partial t} + \nabla\cdot(\alpha_s\rho_s\overrightarrow{v_s}\Theta_s)\right] = (-p_s\bar{\bar{I}} + \bar{\bar{\tau}}_s):\nabla\vec{v}_s - \nabla\cdot(k_\Theta\nabla\Theta_s) - \gamma + \Phi \tag{4.23}$$

Eq. (4.23) has a transient term and a convection term on the left, and a generation term due to solids stress, a diffusion term, two sink terms due to inelastic particle collisions and inter-phase damping on the right. In order to avoid calculation instability, Eq. (4.23) is only solved in its algebraic form by neglecting the convection and diffusion term. This is an acceptable approximation in dense, slow moving systems, but fails for dilute and fast moving systems (Cloete et al., 2012).

4.3.2 Geometry and Mesh

The computational geometry (Figure 4.1) is the same as the experimental fracture cells except for the inlet and outlets. The inlet is simplified as a rectangular opening, and the outlets are simplified as square wells. The domain is divided into small rectangular cells. Because the DDPM model assumes that the discrete phase is at least one order of magnitude smaller than the grid size; different meshes were used for 20/40 proppant and 40/70 proppant. The slot width was set as 2 grids for 20/40 proppant and 3 grids for 40/70 proppant, respectively. The mesh sizes in the height and length direction are identical for

both proppant. The mesh size was varied in the length and the height directions, and mesh independent solutions were achieved. For the base case, the smallest grid sizes in axial and height directions were both 1 mm.

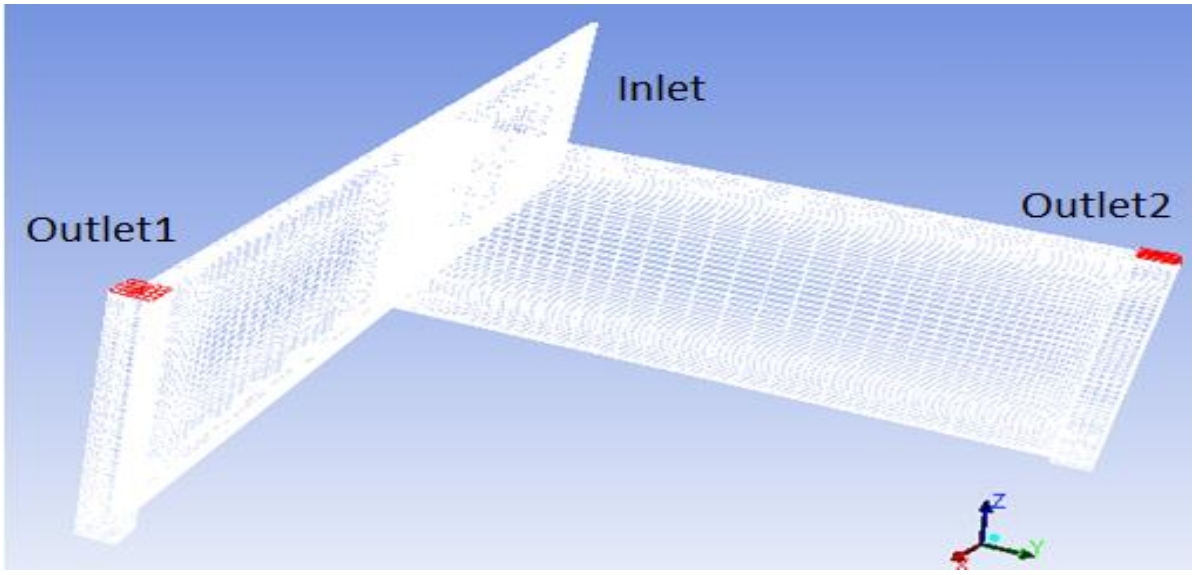

Figure 4.1: Computation geometry and mesh

4.3.3 Initial and Boundary Conditions

Different shear rates were imposed by varying the water injection rate. Proppant injection rates were the same as those in the experiments. The proppant size distribution was assumed to follow the Rosin rammler distribution; the cumulative distributions are shown in Figure 4.2. Friction packing limit is the solid volume fraction beyond which the frictional viscosity becomes dominant. Pressure at the outlet was set to be 0 gauge pressure. No-slip wall boundary condition was set for all phases. Table 4.1 lists all simulation parameters.

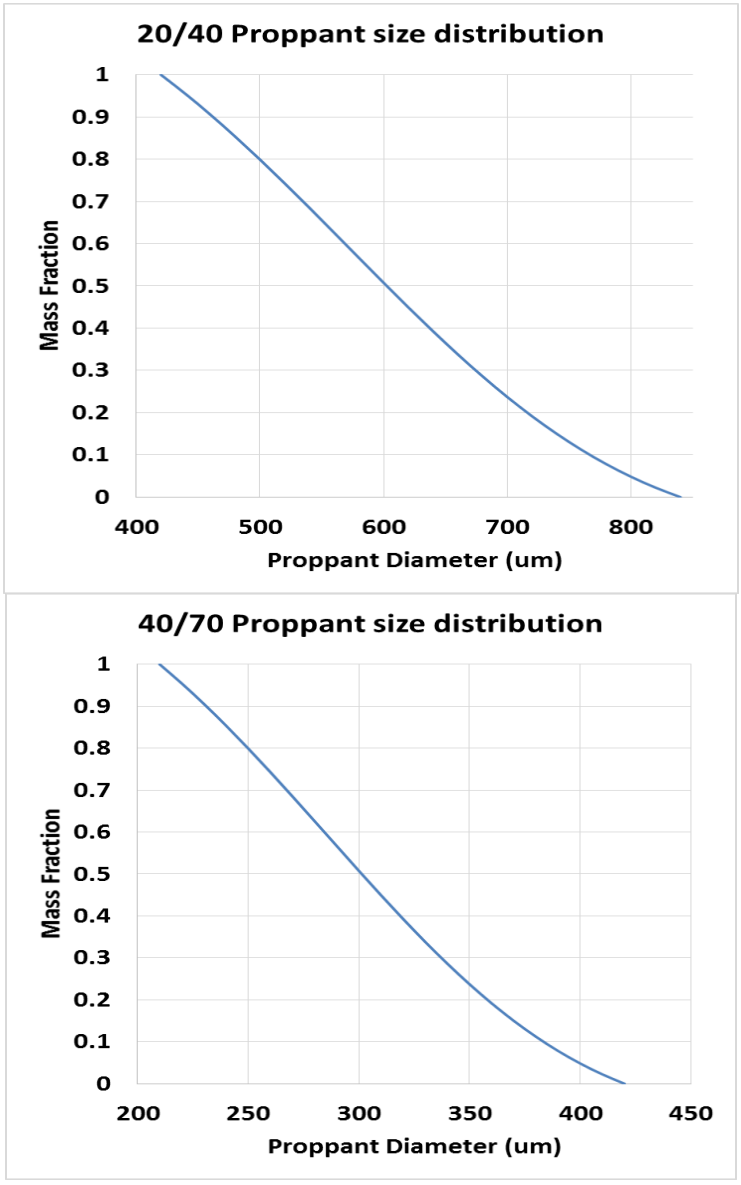

Figure 4.2: Cumulative particle size distribution of 20/40 and 40/70 proppant

Table 4.1. Simulation Parameters

Parameter	Symbol	Value(s)	Unit
Inlet fluid velocity	v_f	0.1,0.2 and 0.3	(m/s)
Inlet solid velocity	v_s	0.1,0.2 and 0.3	(m/s)
Fluid density	ρ_f	998.2	(kg/m^3)
Solid density	ρ_s	2650	(kg/m^3)
Solid diameter	d_s	20/40, 40/70 mesh	(um)
Fluid viscosity	μ_f	1	(cp)
Solid viscosity	μ_s	From KTGF	kg/(m·s)
Restitution coefficient	e	1	Dimensionless
Particle packing limit	$\alpha_{s,max}$	0.63	Dimensionless
Friction packing limit	$\alpha_{s,fri}$	0.61	Dimensionless
Internal friction angle	ϕ	30	Dimensionless

ANSYS FLUENT software was used for the simulation. The phase-coupled SIMPLE algorithm was applied for pressure-velocity coupling, gradient was discretized with the Green-Gauss node based method, and other variables were treated with the QUICK scheme. A node-based averaging scheme was used to distribute the parcel's effects to neighboring mesh nodes. This scheme reduces the grid dependency of DDPM simulations, since the parcel's effects on the flow solver are distributed more smoothly across neighboring cells.

4.4 Results and Discussion

4.4.1 Proppant Concentration and Velocity Profile

Figure 4.3 shows the simulated proppant concentrations for the experiment with 20/40 proppant at 600 s^{-1} shear rate with the 90˚ bypass (case 2.8). The red color corresponds to a high proppant concentration; the green color corresponds to an

intermediate proppant concentration, which represents the fluidized proppant at the top of the proppant bed. The blue color corresponds to a low proppant concentration. The proppant bed forms in the main slot and moves down stream with time. The particles injected later deposit away from the injector. At about 15 s, the bed reaches the bypass, some of the proppant grains move into the bypass slot and start depositing there. The proppant bed shape in the simulation is similar to that in the experiment (Figure 2.6), but not the same. The slopes of the proppant bed are wavy due to coarser mesh in the middle of the domain.

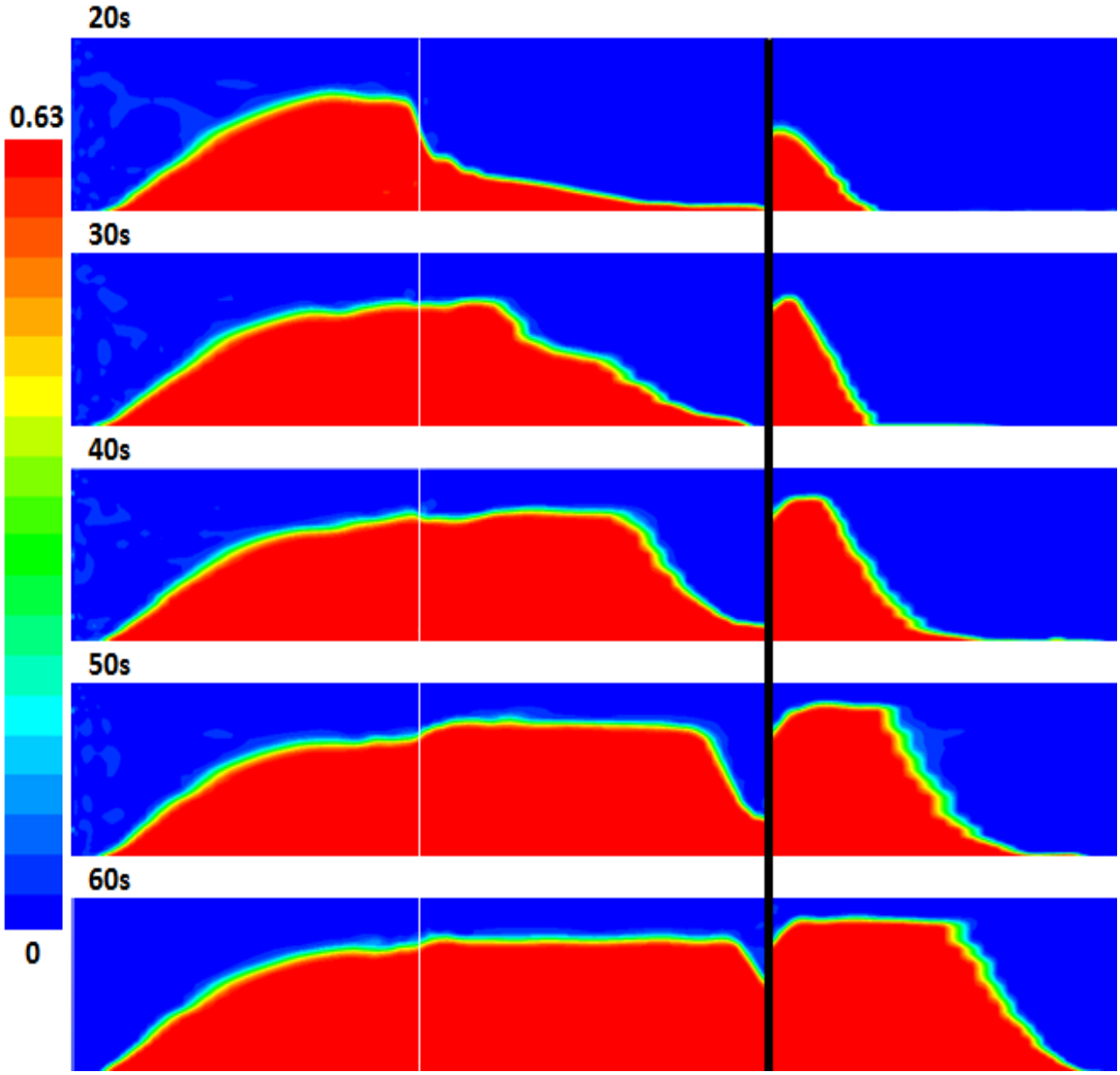

Figure 4.3: Simulation of case 2.8: Proppant bed in the main slot (left of the black line) and bypass slot (right of the black line), 20/40 proppant, 600 s^{-1} shear rate and 90˚ bypass; the color indicates proppant concentration (proppant volume/bulk volume)

Figure 4.4 shows the velocity magnitude of proppant at different time of injection. The red color corresponds to a high proppant velocity; the green color corresponds to an intermediate proppant velocity. The blue color corresponds to a low proppant velocity, and

it could be observed that the velocity of proppant in the proppant bed is zero, which means the formation of an immobile proppant bed at the bottom of the slot. The simulation clearly predicts the three zones: bottom immobile proppant bed zone, middle flowing slurry zone, and top clear fluid zone, as postulated by Wang et al. (2003). As the proppant bed height increases, the proppant flow faster as the flow channel shrinks. In the primary slot, once the proppant flow into the zone above the slope of the proppant bed, the proppant would slow down and settle upon the slope to elongate the growth of the proppant bed. Besides the inertial effects of the proppant, the slickwater flow rate in the bypass slot is smaller than that in the primary slot, which leads to smaller proppant velocity in the bypass slot compared to in the primary slot.

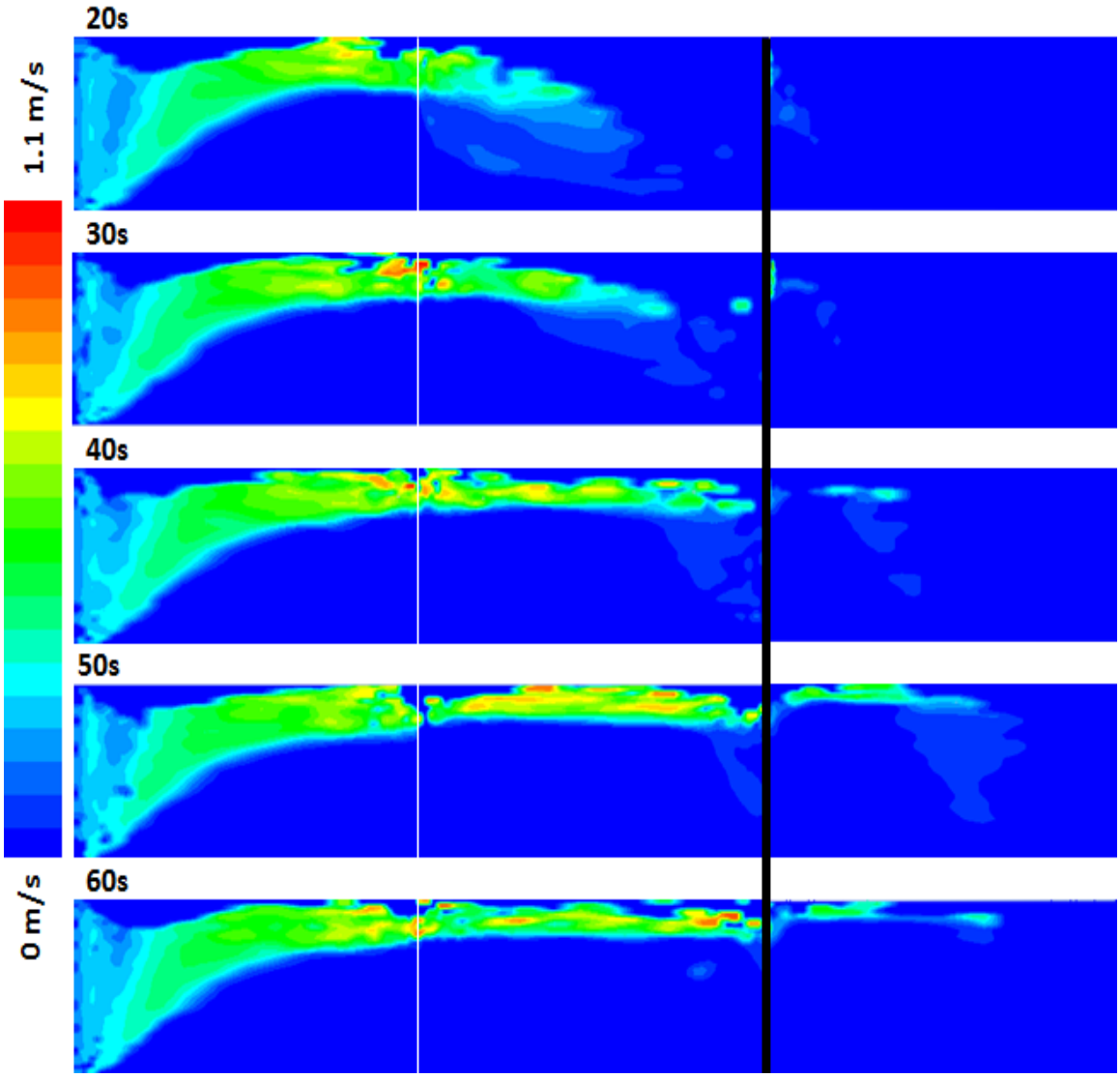

Figure 4.4: Simulation of case 2.8: Velocity profile in the main slot (left of the black line) and bypass slot (right of the black line), 20/40 proppant, 600 s^{-1} shear rate and 90˚ bypass; the color indicates proppant velocity magnitude

Figure 4.5 shows the simulation results of 40/70 proppant at 600 s^{-1} shear rate with the 90 degree bypass (case 2.11). Smaller proppant is easier to flow to the downstream of the slot before complete settling. As a result the proppant bed propagates faster downstream for the smaller proppant. The proppant bed shape in the simulation is similar to that in the

experiment (Figure 2.14, case 2.11, at 40 s). Figure 4.6 shows the velocity magnitude of proppant at different time of injection. It could be observed that the colormap of proppant velocity is more uniform than that in Figure 4.4. This indicates that as the proppant size gets smaller, the slurry is more fluidized.

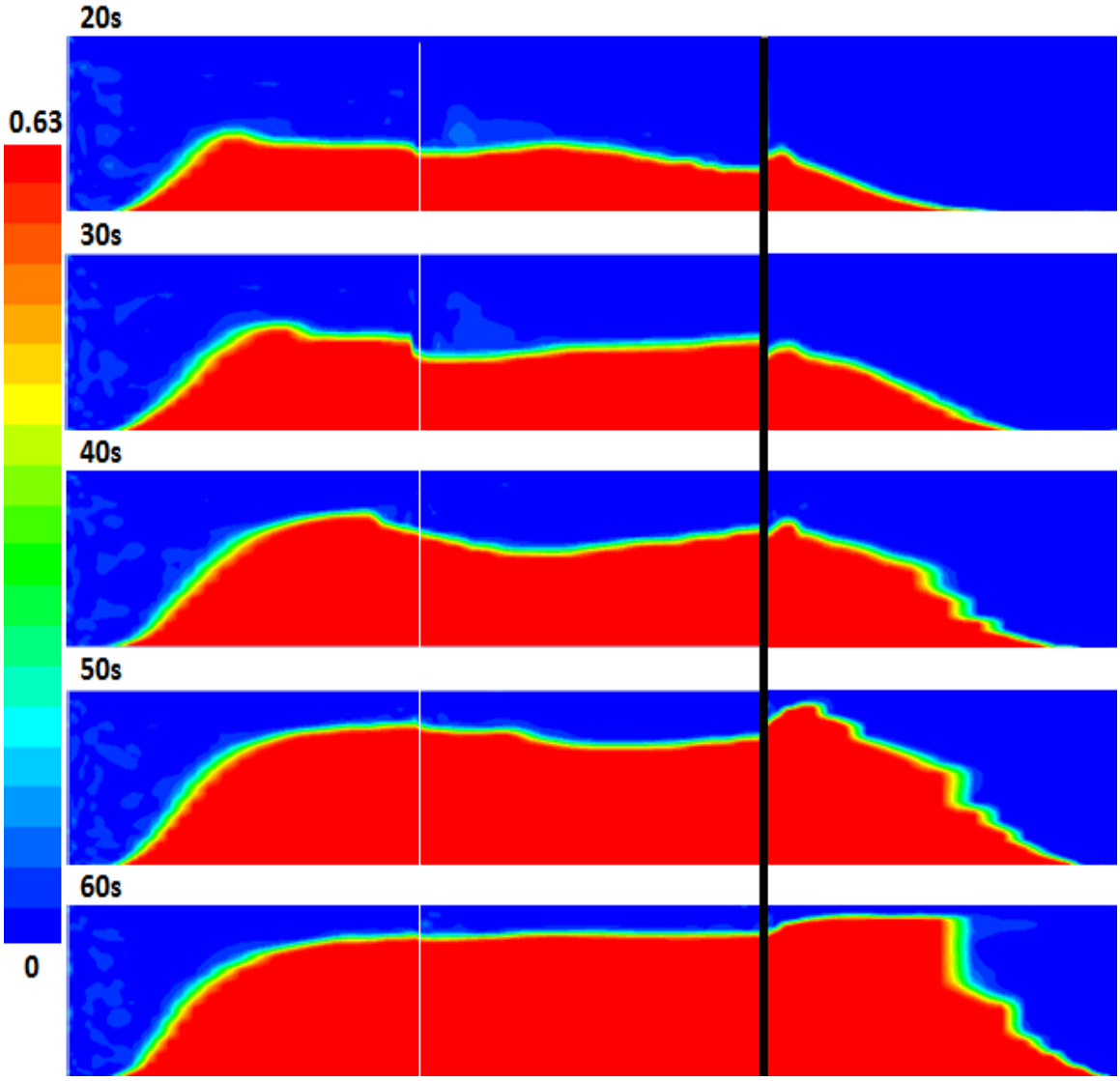

Figure 4.5: Simulation of case 2.11: Proppant bed in the main slot (right of the black line) and bypass slot (left of the black line), 40/70 proppant, 600 s^{-1} shear rate and 90˚ bypass; the color indicates proppant concentration (proppant volume/bulk volume)

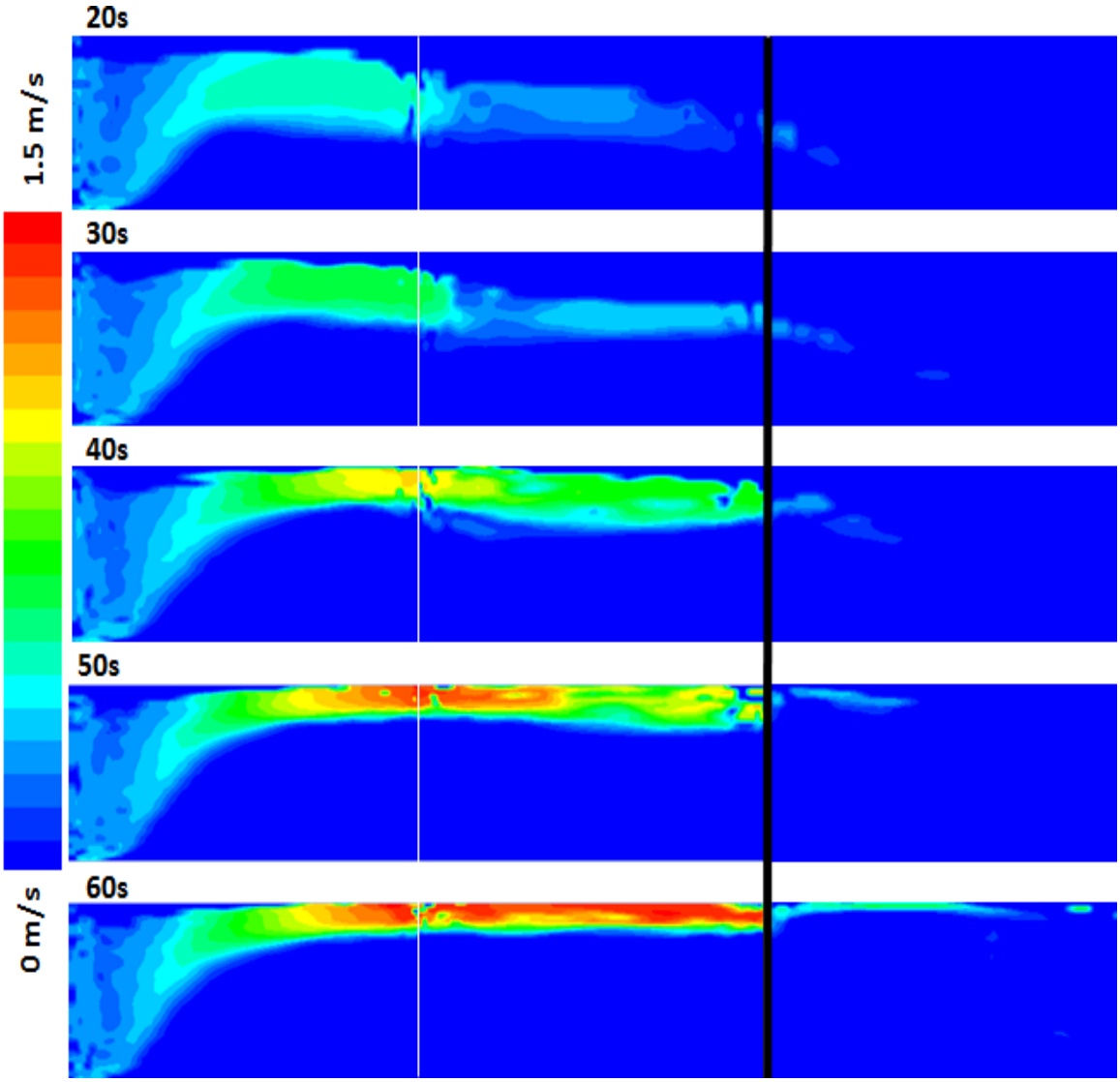

Figure 4.6: Simulation of case 2.11: Velocity profile in the main slot (left of the black line) and bypass slot (right of the black line), 40/70 proppant, 600 s^{-1} shear rate and 90˚ bypass; the color indicates proppant velocity magnitude

4.4.2 Quantitative Match

Figures 4.7 and 4.8 show the fraction of the injected proppant deposited in the bypass for all the 90˚ cases, in both experiments and simulations. The simulation results are very close to the experimental values. The proppant placement in the bypass increases

as the time, shear rate and proppant size increase. The results for 40/70 proppant at 900 s^{-1} shear rate are not shown because the simulation fails for this case. This could be because Eq. (4.23) was only solved in its algebraic form by neglecting the convection and diffusion term. However, for finer particles at dilute and fast moving conditions, these two terms are significant.

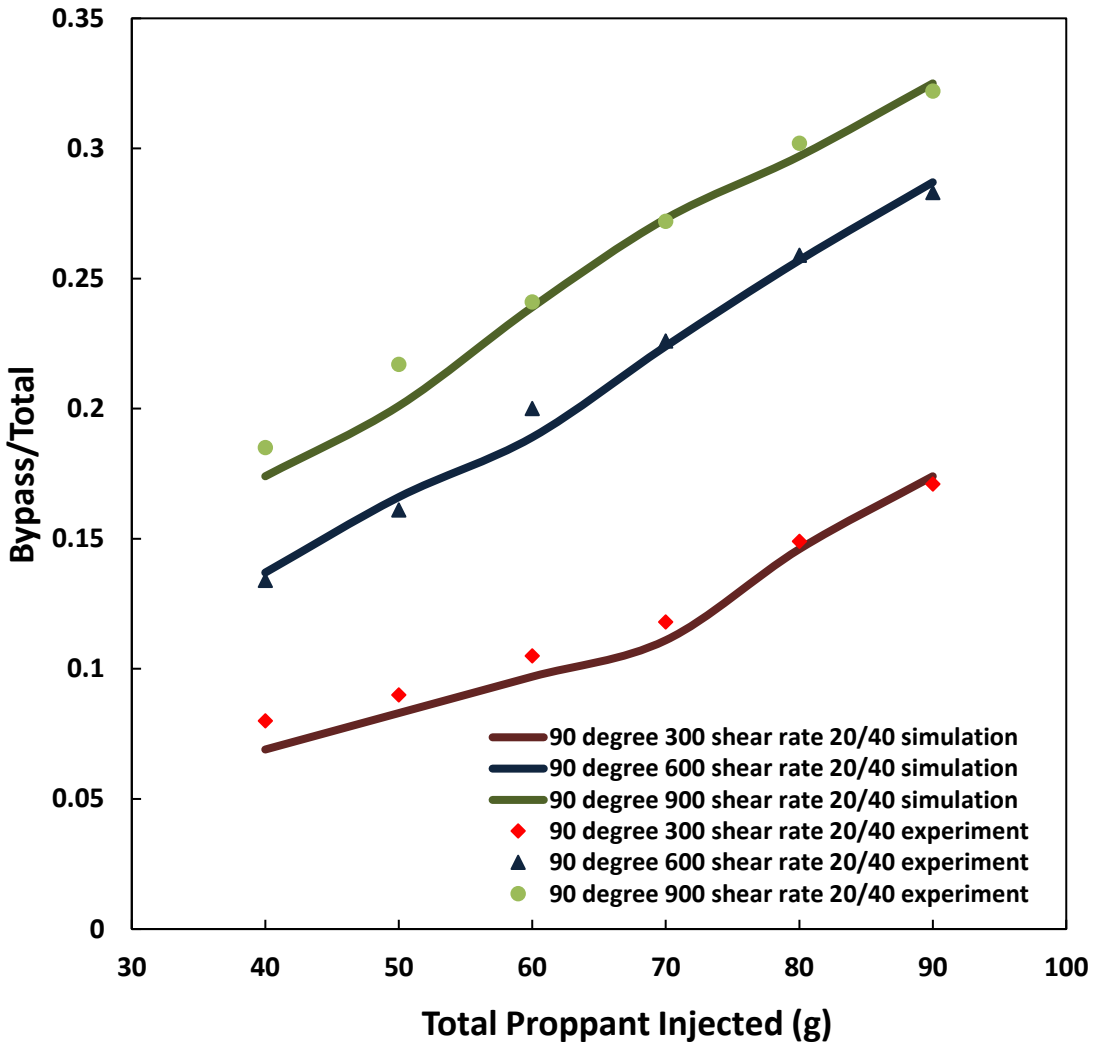

Figure 4.7: Simulation and experimental results of proppant deposited in the bypass for cases 2.7, 2.8 and 2.9

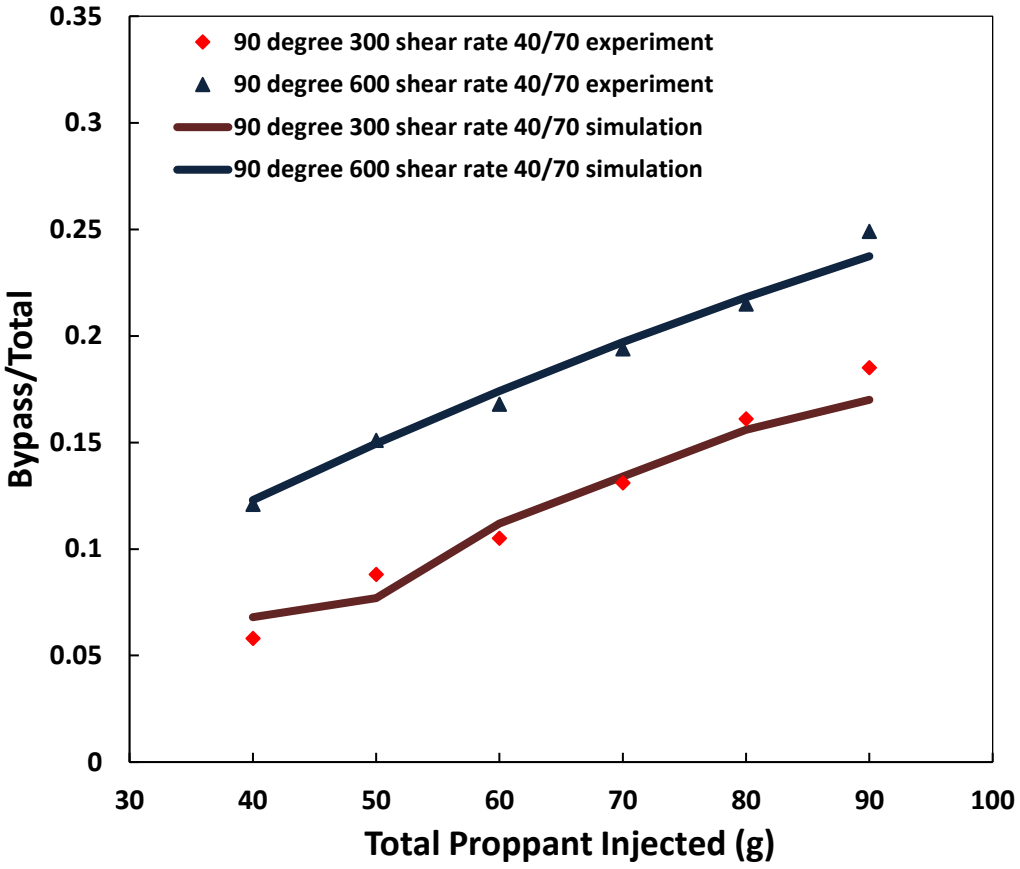

Figure 4.8: Simulation and experimental results of proppant deposited in the bypass for cases 2.10 and 2.11

Equilibrium bed heights are measured at 5 points, as shown in Figure 4.9. Figure 4.10 and 4.11 show the comparison of these heights between experiments and simulations. The simulation heights match the experimental ones except at the first point near the entrance, which may come from the simplification of the injection port. Point 3 shows the equilibrium proppant bed height at the bypass intersection. This analysis shows that the entrance eroded region increases as the shear rate increases.

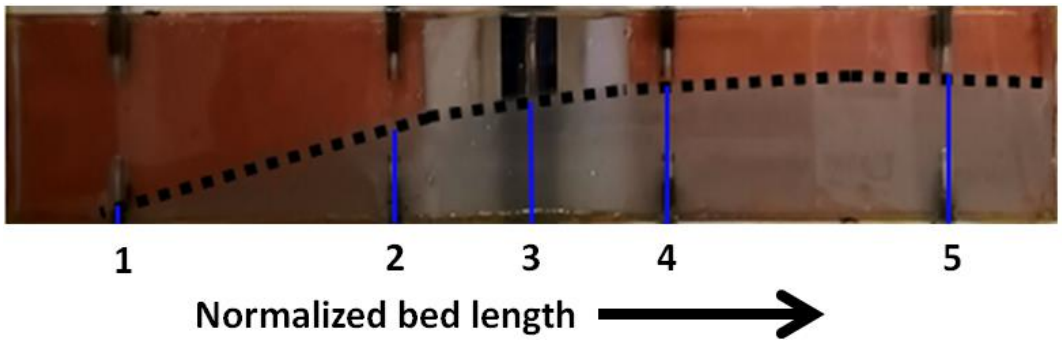

Figure 4.9: Equilibrium bed heights at five points along the main slot

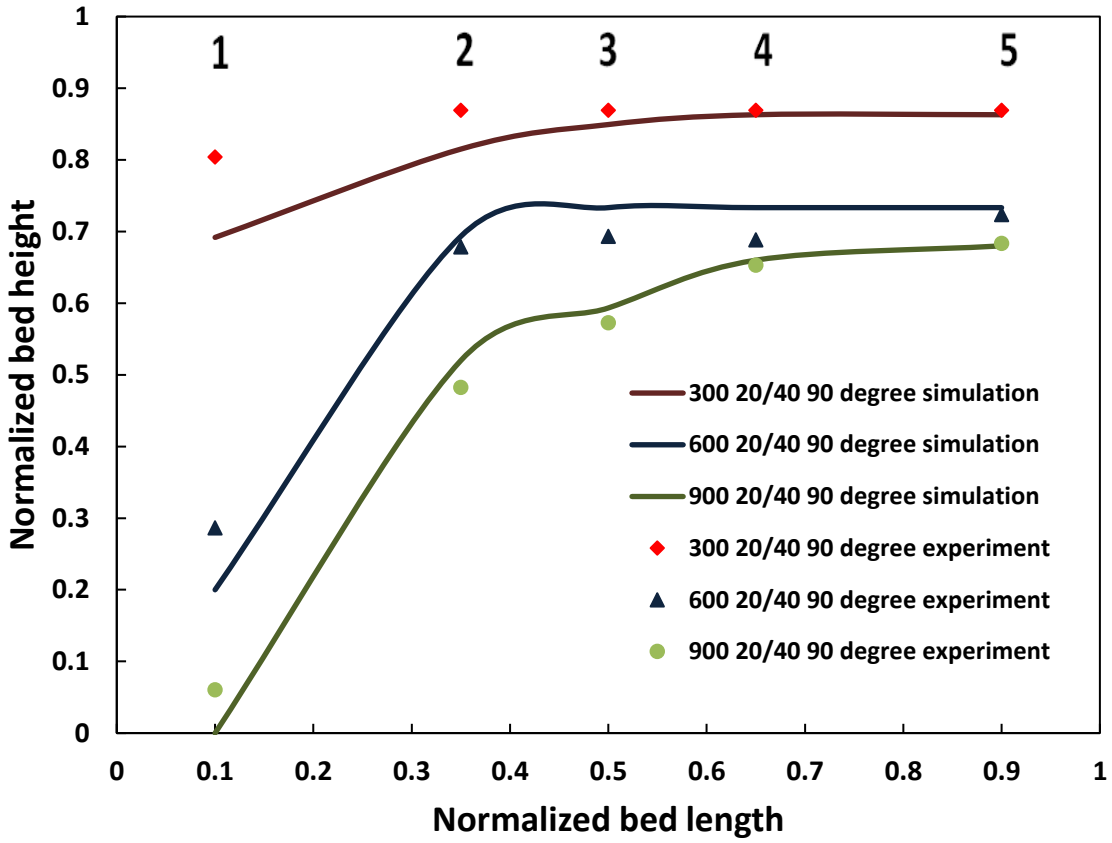

Figure 4.10: Simulation and experimental results of equilibrium normalized bed heights for cases 2.7, 2.8 and 2.9; points 1-5 from Figure 4.9 are indicated at the top of the graph

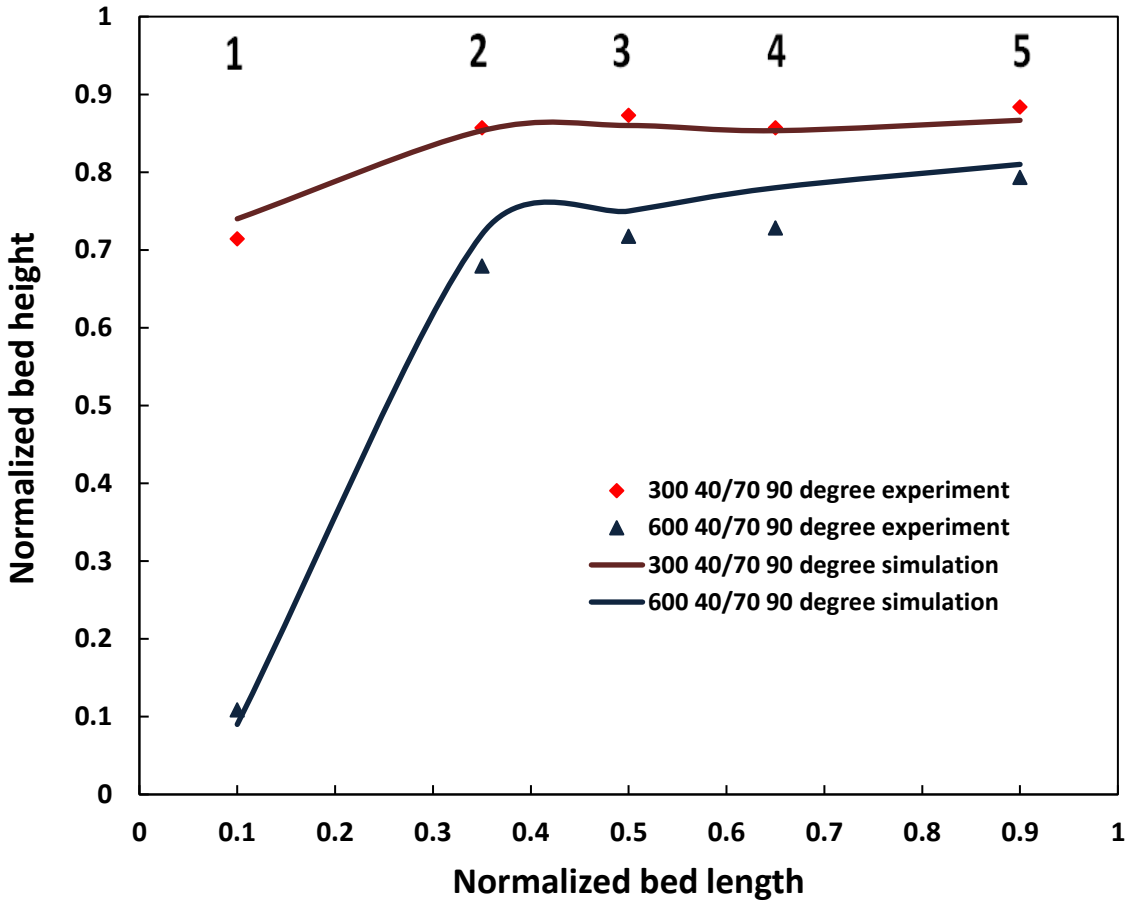

Figure 4.11: Simulation and experimental results of equilibrium normalized bed heights for cases 2.10 and 2.11; points 1-5 from Figure 4.9 are indicated at the top of the graph

In Figure 4.12, the x-axis indicates the total amount of proppant injected, and y-axis indicates the fraction of the total liquid that flows through outlet2 (outlet2 fraction). This figure compares the cases 2.8, 2.10 and 2.11. Initially, the outlet2 fraction is about 0.4 for all the three cases. For case 2.8, the outlet2 fraction decreases at the early stage, then increases to a plateau at a later stage during fracturing. In this case, proppants settle quickly and the proppant bed grows horizontally from the inlet to the outlets. The fast formation of the proppant bed near the injection leads to quick decline of the outlet2 fraction in the early

stage. As the proppant bed accumulates inside the bypass, the outlet2 fraction increases and reaches to a plateau. For case 2.10, the outlet2 fraction decreases at the early stage at a slower rate compared to that of case 2.8, then increases at a later stage. For this case, at the very beginning, some proppant can flow into the bypass before settling, and the proppant bed accumulates both horizontally (from the inlet to the outlets) and vertically (from the bottom to the top) inside the fracture slot. The profile is similar to the one in case 2.8, but more stretched in time. For case 2.11, the outlet2 fraction decreases throughout the entire injection, but the decline rate is the lowest among the three cases compared. In this case, most proppant accumulates from the bottom to the top because 40/70 proppants settle slower. In such condition, the outlet2 fraction decreases more gradually compared to the previous two cases. To summarize, different proppant bed formation processes lead to different outlet2 fraction profiles.

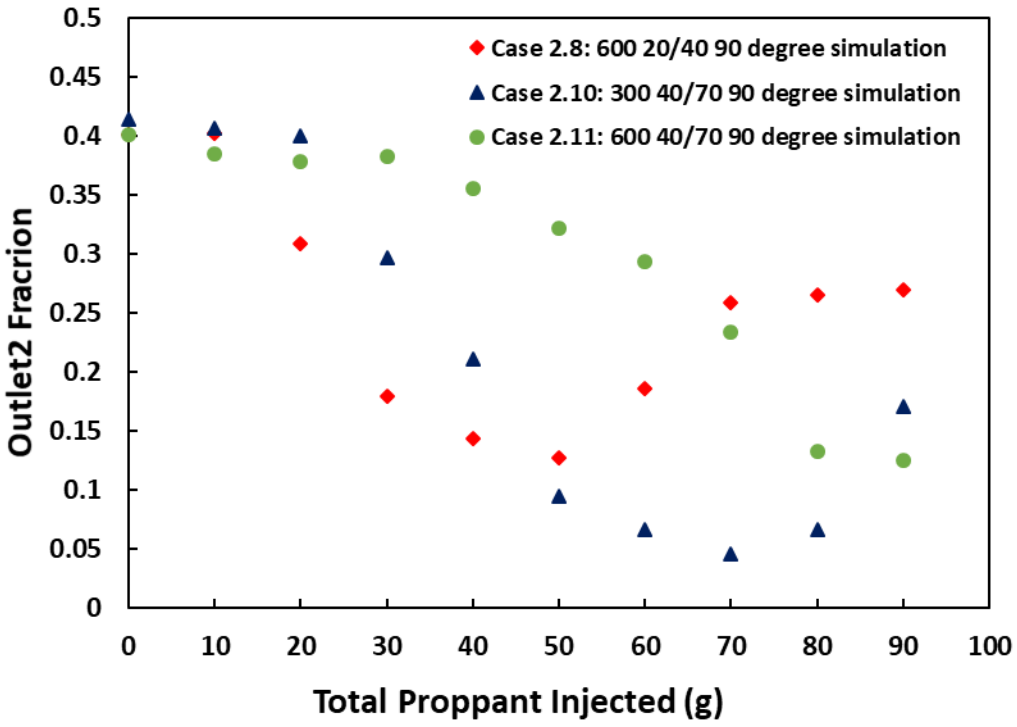

Figure 4.12: Simulation results of outlet2 fraction (outlet2 /inlet) for cases 2.8, 2.10 and 2.11

Figure 4.13 indicates the same case as Figure 4.5 does. The only difference is the cell number of the computation domain. For Figure 4.5, the mesh is finer with total 25270 cells; for Figure 4.13, the mesh is coarser with total 8280 cells. Overall, the difference between the two meshes is moderate. However, obvious difference could typically be observed in two zones in the computation domain: first, at the bypass intersection where local refinement is important; second, at the zones away from the boundaries where much larger cells are used in coarser mesh. Figures 4.14 and 4.15 compare the bypass/total ratio for different cases with finer and coarser meshes. Overall, the bypass/total ratio is fairly close in both finer and coarser mesh.

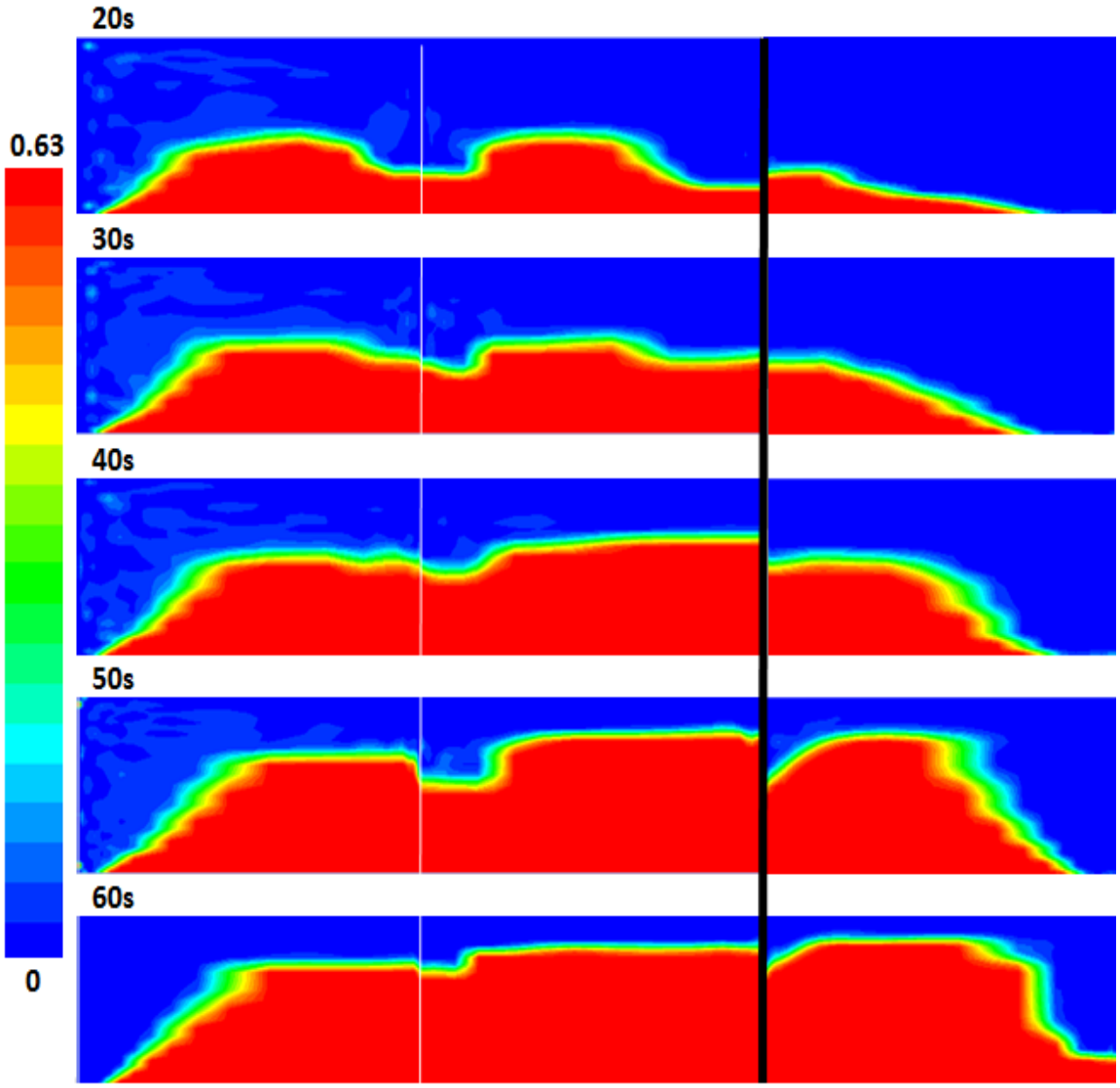

Figure 4.13: Simulation of case 2.11 with a coarser mesh

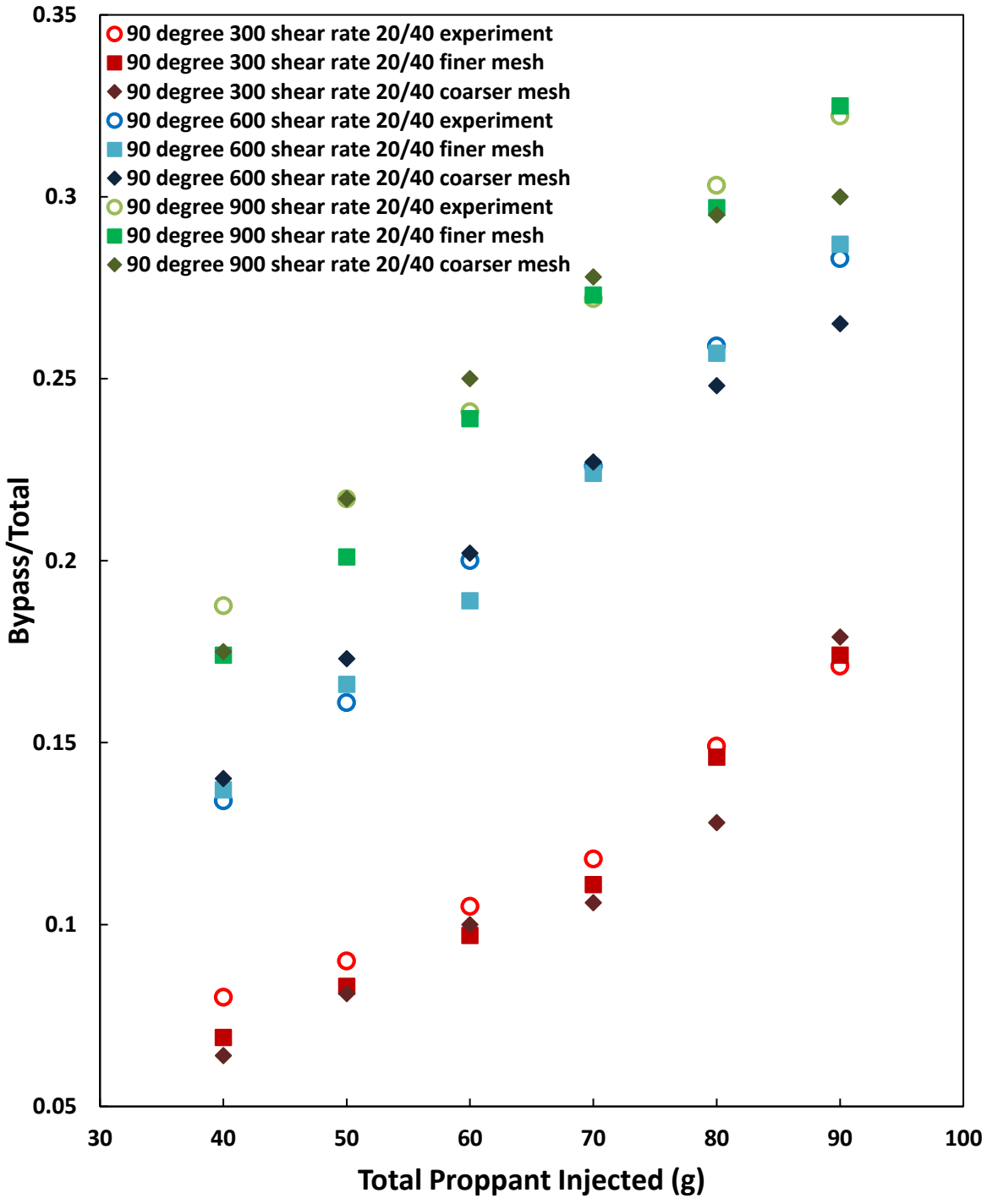

Figure 4.14: Effect of mesh on the bypass/total ratio for 20/40 proppant cases at 300, 600 and 900 s^{-1} shear rates

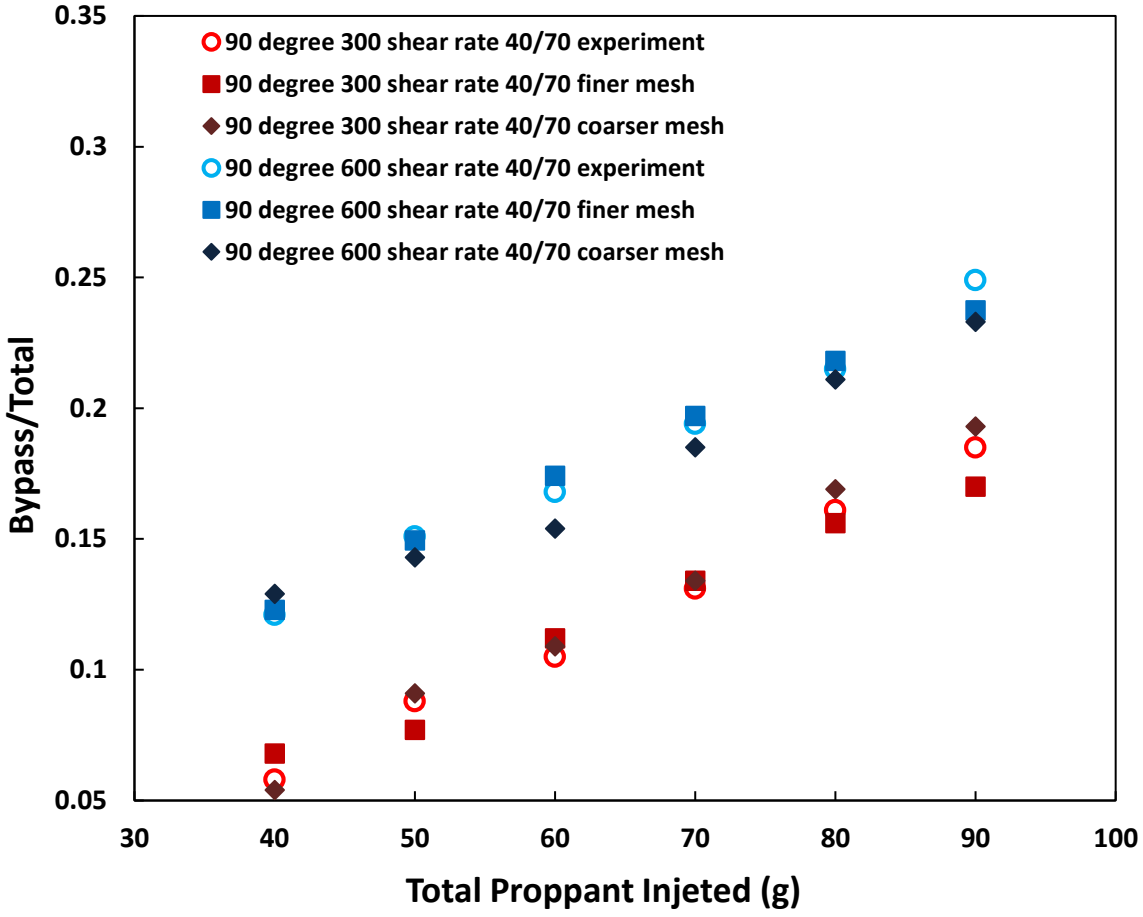

Figure 4.15: Effect of mesh on the bypass/total ratio for 40/70 proppant cases at 300 and 600 s^{-1} shear rates

4.4.3 Proppant Residence Time and Vortex Generation

Figure 4.16 shows the residence time of the proppant particles at the injection time of 30 s for case 2.7 (top panel, 20/40 proppant at 300 s^{-1}) and 11 (bottom panel, 40/70 proppant at 600 s^{-1}). The left frame shows the color code for particle residence time in seconds. The particles are enlarged for clarity. For the larger proppant (top figure), the proppant injected earlier (red) is deposited in the proppant bed at the bottom near the entrance; the proppant injected later (blue) forms the proppant bed further downstream and

at the top. This is similar to the observations stated by Kern et al. (2014). For the smaller proppant (bottom panel), the proppant injected earlier is deposited at the bottom and the proppant injected later is at the top of the proppant bed throughout the length of the bed. Also, bed length is larger for the smaller proppant and bed height is smaller.

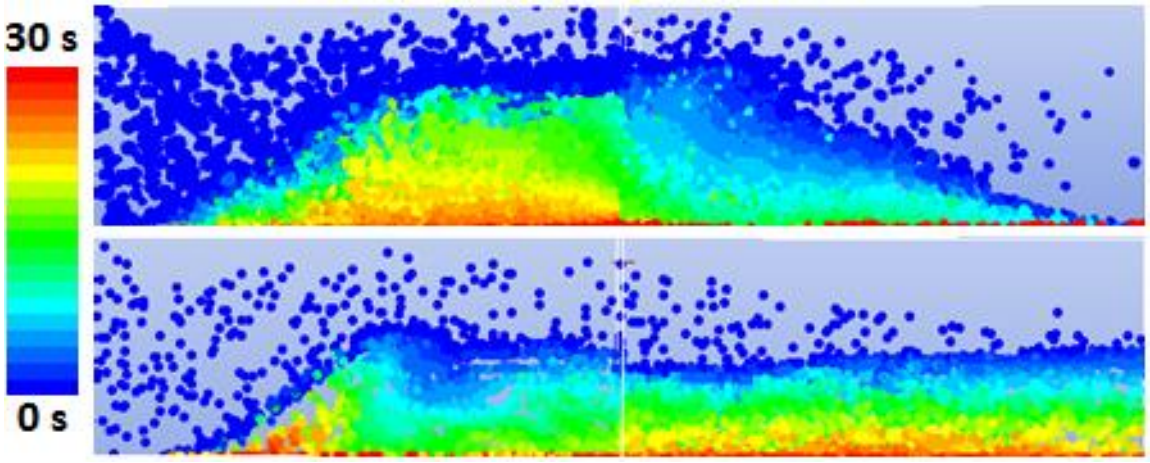

Figure 4.16: Particle residence time for simulation of case 2.7 (top figure) and case 2.11 (bottom figure) at 30 s

The bypass creates a depression in the proppant bed of the main slot at the intersection of case 2.11. The X velocity profile of slickwater indicates that a vortex (inside the black dashed-line box) is generated at the intersection of the bypass slot as shown in Figure 4.17, which is also observed in the experiment as shown in Figure 2.14. This vortex can significantly erode the proppant bed if the proppant size is small.

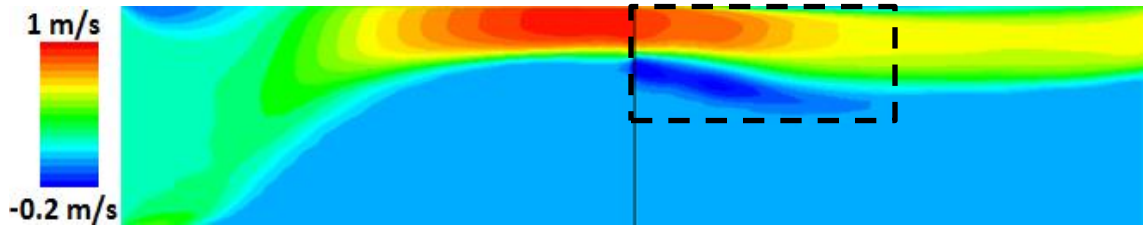

Figure 4.17: X velocity profile of slickwater of case 2.11 at 40 s; a vortex is generated at the intersection as observed in the corresponding experiment in Figure 2.14.

Even though this model is validated against simplified experimental scenarios with fixed fracture geometry and simplified boundary conditions, it captures some of the key mechanisms observed in the experiments, and also matches laboratory results quantitatively. This proppant transport model could be coupled with a geomechanical fracturing model to simulate more realistic fracturing processes.

4.5 CONCLUSIONS

In this chapter, a hybrid CFD model is established to simulate the experimental cases in Chapter 2. The simulation model captures the key features of proppant transport in the laboratory model. Such a model can be used to estimate proppant transport and placement in field-scale models. The following main conclusions are made in this chapter.

1. A hybrid Eulerian-Lagrangian CFD model, DDPM, is established to study proppant transport. In this model, particles (particle size distribution could be considered) are grouped into parcels to accelerate computation and particle trajectory can be obtained in this model.

2. This model can nicely match both qualitative and quantitative results against experimental data including: three-zone transport, proppant bed shape, proppant residence time, generation of vortex and proppant amount flowed into the bypass slot.

3. The grid size of the mesh can alter the proppant bed profile. Obvious difference could typically be observed in two zones in the computation domain: first, at the bypass intersection where local refinement is important; second, at the zones away from the

boundaries where much larger cells are used in coarser mesh. However, the bypass/total ratio is fairly close in both coarser and finer mesh.

4. This model fails for diluted slurry at high shear rate scenario such as slurry flow through perforation holes. However, the model should work for proppant transport in fracture geometry in most of field conditions.

NOMENCLATURE

α	Volume fraction (%)
ρ	Density (kg/m^3)
$\vec{v}$	Velocity vector (m/s)
p	Pressure (Pa)
$\bar{\bar{\tau}}$	Stress strain tensor (kg/(m·s^2))
$\vec{g}$	Gravitational vector (m/s^2)
β	Interphase momentum exchange coefficient (kg/(m^3·s))
t	Time (s)
μ	Viscosity (kg/(m·s))
C_D	Drag coefficient
Re	Reynolds number
d	Diameter (m)
e	Restitution coefficient
Θ_s	Granular temperature (m^2/s^2)

$\vec{I}$ Unit Tensor

λ_s Bulk viscosity (kg/(m·s))

g_o Radial distribution function

k_Θ Granular energy diffusion coefficient (kg/(m·s))

γ Collisional dissipation of energy (W/m^3)

Φ Interphase energy exchange (W/m^3)

ϕ Internal friction angle (degree)

Chapter 5: Simulation of Proppant Transport in Foam

5.1 SUMMARY

Foam is not a single-phase fluid; it is dynamic due to liquid drainage. Additionally, the existence of individual foam bubbles could significantly alter the movement of proppant, as discussed in chapter 3. Therefore, it could be misleading to assume foam as a single-phase fluid and apply its apparent viscosity to calculate proppant settling.

The objective of chapter 5 is to develop an empirical model for proppant settling in foam fracturing fluid based on the experimental results in chapter 3, and then incorporate it into an in-house numerical model to evaluate proppant placement in foam fracturing applications.

Our results found that foams place proppants more uniformly than slickwater. For dry foams, drainage has little effect on the final proppant placement. For wet foams, drainage affects the proppant placement significantly. The faster the foam drains, the less uniform is the final proppant placement. The liquid from the foam collects at the bottom where the proppants settle fast and form a small proppant bed.

5.2 INTRODUCTION

The proppant movement in a foam is controlled by the particle-bubble interaction (Cantat and Pitois, 2006; Jing et al., 2016; Raufaste et al., 2007). Raufaste (2007) measured the total drag force of a flowing foam on a circular obstacle within a long 2D channel. In their study, the obstacle diameter was larger than the foam bubble diameter. They showed that the total drag force of foam bubbles on an obstacle (F) could be described as

$$F = F^p + F^n \tag{5.1}$$

This chapter is based on an in review journal publication (Tong, Gu, Singh, and Mohanty). Gu helped with the fracturing modeling. Singh helped with the experiments. Dr. Mohanty supervised the project.

where F^p and F^n are the forces from the pressure inside bubbles and from bubble lamella, respectively, as shown in Figure 5.1. The force from the bubble lamella, F^n is estimated by

$$F^n = \frac{0.516}{(1-\phi_g)^{1/4}}\frac{\gamma d}{\sqrt{A}} \tag{5.2}$$

where ϕ_g, γ, d and A are foam quality, line tension of bubble film, obstacle diameter and bubble area, respectively. After measuring the total force F via a fiber sensor connected to the obstacle, the bubble pressure force F^p was calculated with Eq. (5.1).

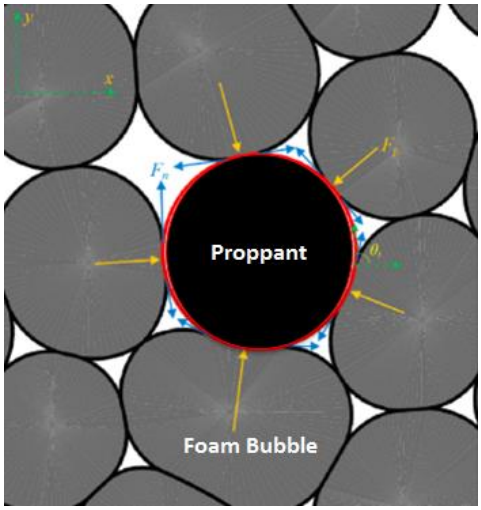

Figure 5.1: Forces on a proppant from surrounding foam bubbles (Jing et al., 2016)

Jing (2016) extended the work to obstacles having the same size as the bubbles. A single particle settling in foam was studied both experimentally and numerically. With the introduction of friction coefficient, λ, a more generalized equation was proposed to calculate the total force F:

$$F = a\left(1-\phi_g\right)^b\lambda \tag{5.3}$$

where a and b are fitting parameters which are dependent on the particle and the foam fluid.

In chapter 3, we investigated proppant settling under dynamic conditions in foams at ambient conditions. Several interesting phenomena were observed in our study. First, liquid drainage significantly affects the settling velocity of proppants, as shown in Figure 5.2. The top and bottom images show the typical proppant transport pattern in 70% and 80% nominal quality foam. Because of severe liquid drainage, proppants settle fast, and a liquid bank accumulates at the outlet of the slot in 70% foam cases. As a result, a proppant bed is formed near the entrance, which is similar to slickwater experimental results (Liu and Sharma, 2005).

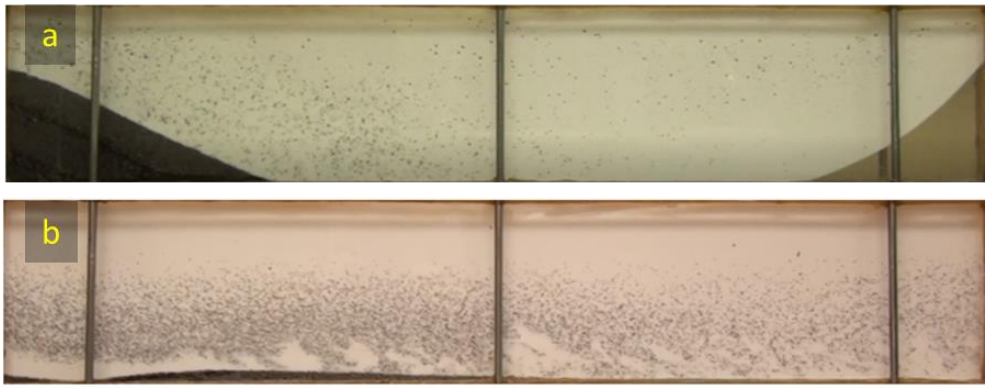

Figure 5.2: Proppant transport in (a) wet (70% nominal quality) and (b) dry (80% nominal quality) foams

For 80% quality foam, proppants settle very slowly. Generally, the slurry moves faster at the bottom of the slot probably due to a lower local foam quality, and the proppants also settle relatively faster at the bottom. The shear rate dependent effective viscosity alone is not sufficient to model proppant settling velocity in foams as it treats foam as an homogeneous "phase," ignores liquid drainage and bubble-proppant interaction. Thus, clearly, there is a need to develop a model which can account for foam phase separation and its effect on proppant settling.

Foam is not a single-phase fluid; the liquid in foam drains slowly and changes the quality of foam with time and location. Foams consist of liquid lamellae (cell face) which meet in Plateau borders (cell edges), as shown in Figure 5.3 (Verbist et al., 1996). The cross-section of the Plateau border decreases as the foam liquid fraction decreases. The vertices of the foam network are junctions of at least four borders (Koehler et al., 1999). Liquid drains down in foam due to gravity and capillary forces and the flow is resisted by viscous and disjoining forces (Koehler et al., 2000). Severe drainage could conceptually lead to a continuous gas zone at the top of the fracture as dry foams collapse, a liquid layer at the bottom of the fracture as liquid drains down, and a foam zone in between. This scenario should be minimized in completion treatments as it would lead to poor proppant placement (Fei et al., 2017). Since the local foam apparent viscosity, which governs the proppant settling, is a strong function of the local foam quality, it becomes important to incorporate this spatial variation of quality in the model induced by foam drainage.

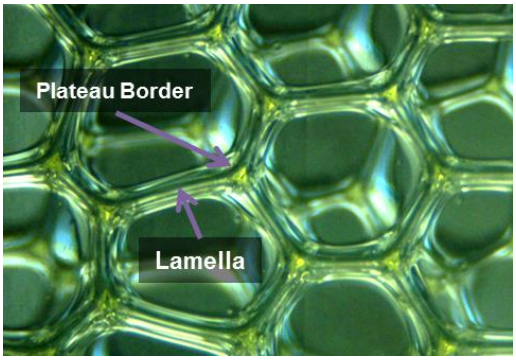

Figure 5.3: Typical foam microstructure

Liquid drainage in foam has been investigated (Weaire et al., 2007). There are two main approaches to investigating foam drainage: (1) free drainage (in which freshly made foam is allowed to drain) and (2) forced drainage (in which the liquid is continuously introduced to the top of the foam). Forced drainage offers the possibility to relate the steady

rate of drainage to the corresponding liquid fraction of the foam in the absence of bubble collapse and coalescence. However, a free drainage scenario is closer to foam fracturing applications.

Free drainage goes through three regimes in time: a transient regime, a linear evolution regime, and a final exponential equilibrium regime (Hutzler et al., 1995; Verbist et al., 1996). Figure 5.4a shows an experimental result of a free drainage experiment with initial liquid fraction equals to 13%. X-axis and y-axis indicate the vertical position of the foam column and the foam liquid fraction, respectively. The very bottom of the foam column is not shown in Figure 5.4a. Due to the complexity of free drainage, it is not possible to derive an analytic solution to quantify the liquid fraction as a function of time and vertical position (Weaire et al., 2007). Instead, Figure 5.4b shows the numerical solution of a free drainage process against dimensionless time τ excluding the transient regime. The y-axis indicates the plateau border area, a proxy for the liquid fraction, as a function of the dimensionless foam height, ξ. As observed, for the linear evolution regime, two trends are evolved in foam free drainage process: (1) the liquid fraction of foam $(1-\phi_g)$, varies almost linearly in the vertical direction; (2) the slope of the linear relationships changes with time and is also a function of $(1-\phi_g)$ (Weaire et al., 2007).

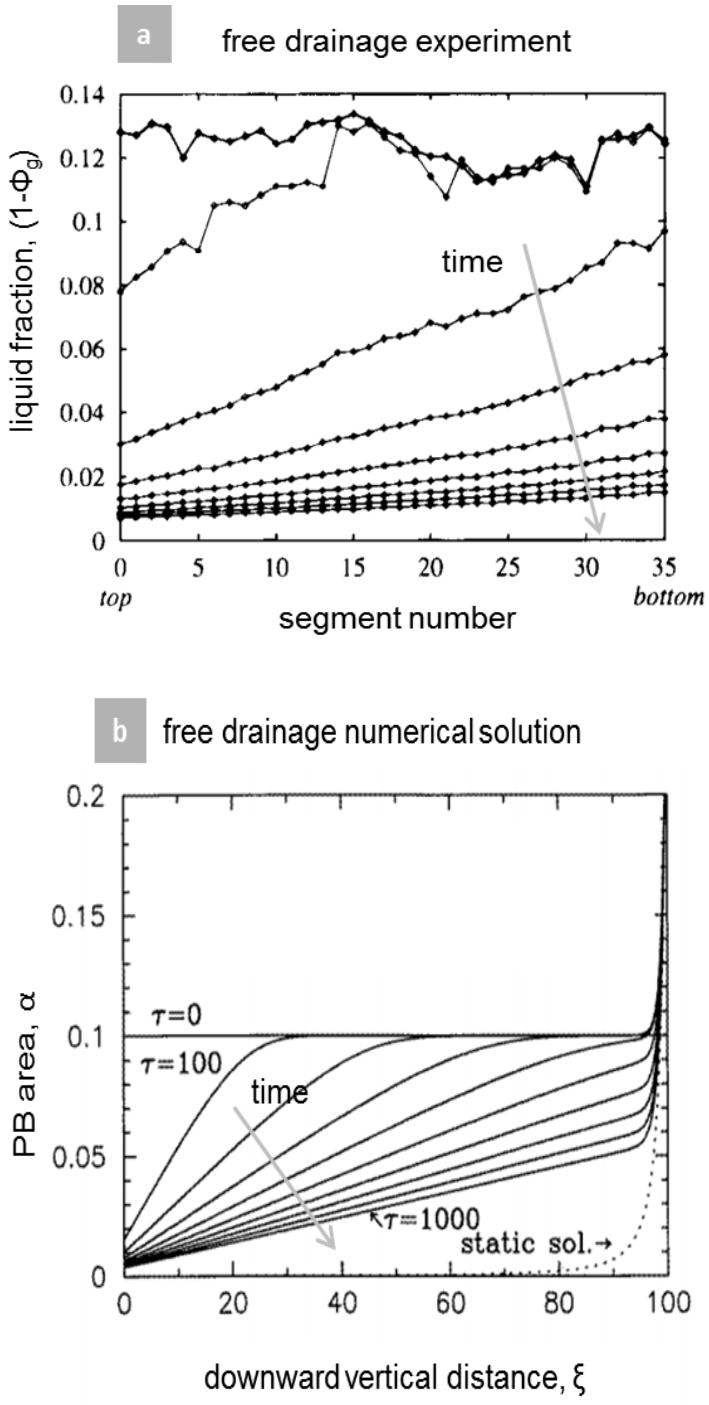

Figure 5.4: (a) Liquid fraction as a function of foam height column during free drainage experiment (Hutzler et al., 1995); (b) Full numerical solution to the free-drainage case at various time (Verbist et al., 1996)

In this study, a proppant settling velocity correlation and a foam drainage model are developed and incorporated into an in-house fracturing simulator (Gu and Mohanty, 2014; Tong et al., 2018) to investigate foam fracturing performance in the field scale. Due to the limitations of the experimental setup, dynamic proppant settling experiments were conducted at ambient conditions. The following assumptions were made in our model: (1) foam bubble generation were neglected; (2) pressure and temperature did not affect the stability of the foam lamellae; (3) the existence of proppant did not affect the structure of the foam. Clearly, these assumptions are not valid for a weak foam. However, for foam fracturing applications, strong foams are typically used to ensure proppant carrying ability. Moreover, the coalescence of foam lamellae can be significantly retarded by addition of foam boosters such as polymers or nanoparticles in the foaming formulation (Alzobaidi et al., 2017; Xu et al., 2016). The foam rheology data was obtained from the lab results of Gu and Mohanty (2015).

5.3 METHODOLOGY

5.3.1 Foam Drainage Model

Based on the literature, a model is proposed for the foam liquid fraction $(1-\phi_g)$. The liquid fraction in the foam column is assumed to be proportional to a scaling function, f given by:

$$f(R_0, \bar{z}, t) = e^{-R_0 \bar{z} t} \tag{5.4}$$

where R_0, $\bar{z}$ and t are the drainage rate, normalized fracture height and time of drainage, respectively (Hutzler et al., 1995; Verbist et al., 1996; Weaire et al., 2007). In Figure 5.5, the x-axis is the normalized height of the fracture and the y-axis is the value of the scaling function, f. It shows that the scaling function gradually changes from an almost linear

profile to an exponential profile as time progresses. Assuming the gas density is fairly constant at the reservoir condition, the average foam quality remains the same as the initial foam quality during the entire drainage process. Therefore, the area below the scaling function should always equal to the initial liquid fraction. If the fracture height is uniformly divided into n_z grid blocks with each block size of $\Delta\bar{z}$, then we can define a weighting factor $w(j)$ at the specific time step of j as:

$$w(j) = \frac{1 - \phi_{g,initial}}{\Delta\bar{z}\sum_{i=1}^{n_z} f(i,j)} \tag{5.5}$$

Therefore, the liquid fraction of grid i at time j can be expressed by:

$$\phi_l(i,j) = \frac{w(j)f(i,j)}{w(1)} \tag{5.6}$$

For example, Figure 5.5 shows the drainage profile of a 75% quality foam (25% liquid fraction) in both linear regime and exponential regime. The effect of horizontal flow on the drainage process is neglected.

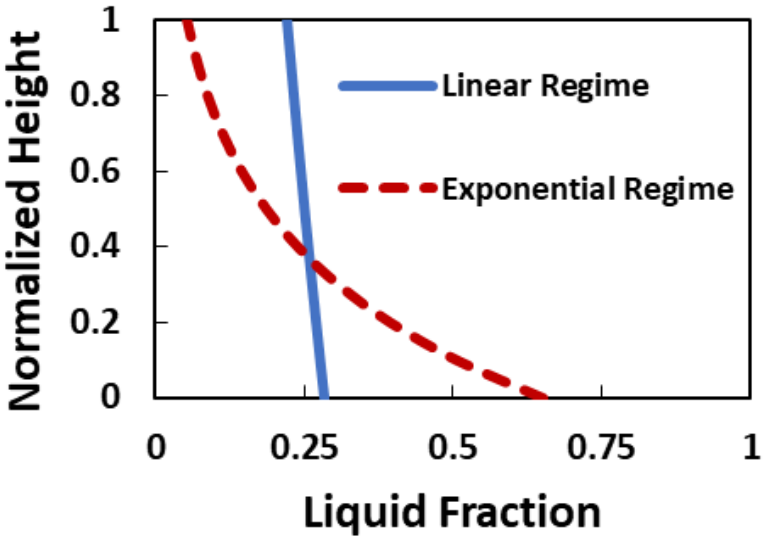

Figure 5.5: Drainage profile of a 75% quality foam derived from the scaling function

This model predicts foam liquid volume fractions greater than the critical value $\phi_{l,t}$ (36%) at the bottom of the column (say, below height, z_f). However, at this liquid fraction, the gas bubbles are isolated, migrate upwards and leave a pure liquid layer at the bottom. To incorporate this mechanism, we forced the liquid fraction to be 100% once the liquid fraction approaches $\phi_{t,l}$ (36%). Then, we corrected the height of the pure liquid layer (z_l) to maintain mass balance by assigning the liquid fraction of 100% to this layer. The liquid fraction was kept at (36%) between z_l and z_f, as shown in Figure 5.6. This drainage model is able to capture the drainage profile as well as the accumulation of the liquid layer at the bottom of the foam column.

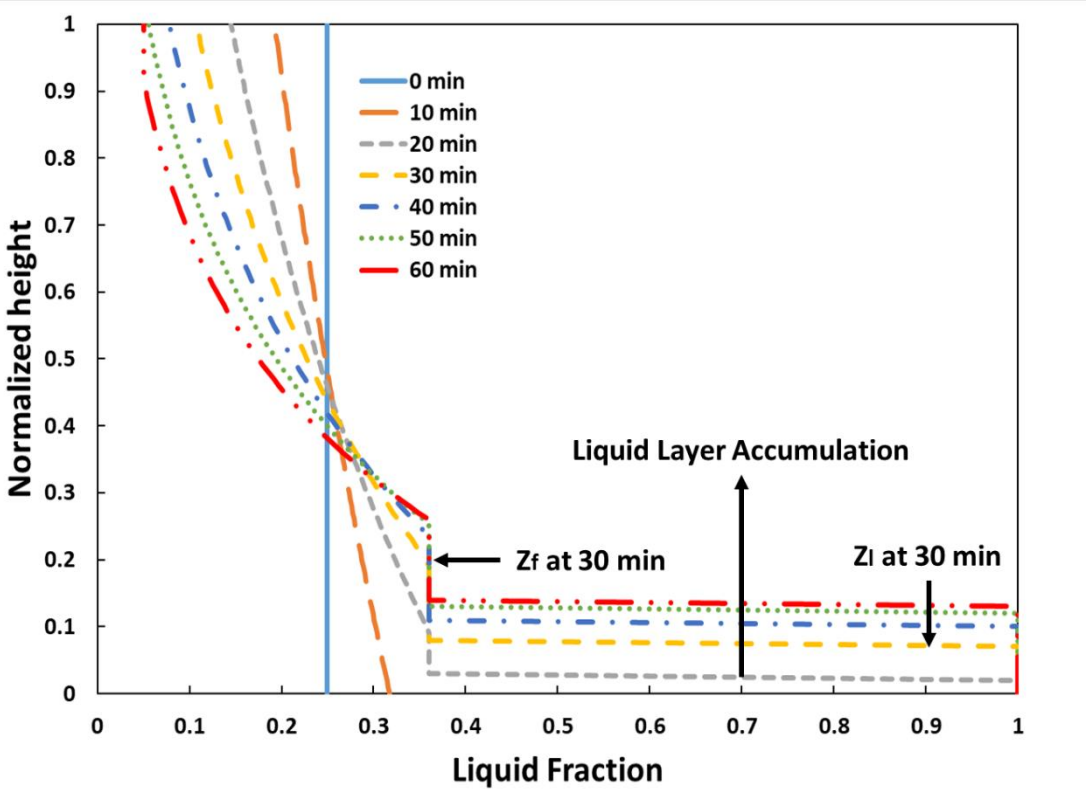

Figure 5.6: Foam liquid fraction profile

5.3.2 Correlation of Settling Velocity in Foam

Particle settling in a foam is more complex than settling in a single-phase shear-thinning fluid due to the existence of the foam microstructures. For liquid fraction greater than 36%, we use the classical Stokes equation for the settling velocity. For liquid fraction lower than 36%, we propose the following empirical expression for the settling velocity, V_Z:

$$V_z = a_0(1-\phi_g)^{b_0}\left(\left|\frac{dV_{xn}}{d\bar{z}}\right|\right)^{c_0}\sqrt{\frac{d(\rho_s-\rho_f)}{\rho_f}} \tag{5.7}$$

where a_0 , b_0 and c_0 are three empirical parameters. This expression is based on experimental evidence that the settling velocity increases with proppant diameter, proppant density, liquid fraction, and the local shear rate $\frac{dV_{xn}}{d\bar{z}}$ (Jing, 2016). This expression is compared with our experimental results and the parameters are extracted.

Eq. (5.7) is based on a single particle and recently the complex settling behavior of two particles in foam has also been reported (Jing et al., 2018). The settling could be accelerated or hindered depending on the relative position of the two particles. For simplicity, we used the retardation factors (see Eq. (5.16)) to account for hindered settling for concentrated slurry proposed by Liu and Sharma (2005).

5.3.3 Fracturing Modeling

A 2D fracture model is developed based on the PKN model (Nordgren, 1972; Perkins and Kern, 1961), which assumes the fracture has a constant height and an elliptical cross section. The width of the fracture is expressed by

$$w(x,z) = \frac{1-\nu}{G}(h^2-4z^2)^{0.5}(P[x]-\sigma_{hmin}), \qquad -\frac{h}{2} < z < \frac{h}{2} \tag{5.8}$$

where x and z are the horizontal and vertical positions, w is the fracture width, ν is Possion's ratio, G is the shear Modulus, h is the fracture height, $P[x]$ is fluid pressure in horizontal direction, and σ_{hmin} is the minimum horizontal stress.

Horizontal fluid pressure gradient along a narrow, elliptical channel is given by:

$$\frac{\partial(P[x]-\sigma_{hmin})}{\partial x} = -\frac{64\mu_f q}{\pi h w_{max}^3} \tag{5.9}$$

where $\mu_f$is the viscosity of the fracturing slurry, q is the total volumetric flow rate. μ_f is a function of the foam viscosity and the proppant concentration (Brouwers, 2010):

$$\mu_f = \mu_l\left(\frac{1-c_p}{1-c_p/c_1}\right)^{\frac{a_1 c_1}{1-c_1}} \tag{5.10}$$

where μ_l is the viscosity of the carrier fluid (foam), c_p is the proppant concentration, c_1 is the random close packed volume fraction and a_1 is a coefficient. For hard sphere suspensions at low shear, $c_1 = 0.64$ and $a_1 = 2.5$. Foam rheological data was retrieved from the previous experimental work (Gu and Mohanty, 2015). The foam rheology was described with a power-law model,

$$\mu_{app} = K\gamma^{n-1} \tag{5.11}$$

where μ_{app}, γ, K and n are the apparent foam viscosity, shear rate, consistency index and power-law index, respectively. The consistency index (K) and the power-law index (n) depend on both foam quality and pressure (psi) as follows (Gu and Mohanty, 2015):

$$\mathrm{K} = 10^{\left(5.89\phi_g{}^2+0.43\phi_g-4\right)} + 8.6\times10^{-11}e^{21\phi_g}(P-1000),\ 64\% \le \phi_g \le 95\% \tag{5.12}$$

and

$$\mathrm{n} = 1.54 - 1.64\phi_g{}^2 - \left(0.89\phi_g - 0.21\right)\left[\log\left(\frac{P}{1000}\right)\right],\quad 64\% \le \phi_g \le 95\% \tag{5.13}$$

Combining Eqs. (5.8)-(5.13) with the 1-D continuity equation of an incompressible, single phase fluid, leads to:

$$-\frac{G}{64(1-\nu)h}\frac{d}{dx}\left[\frac{\partial(w_{\max}^4)}{\mu_f \partial x}\right]+\frac{8C_l}{\pi\sqrt{t-\tau}}+\frac{dw_{max}}{dt}=0$$

$$IC: w_{max}(x,0)=0; \tag{5.14}$$

$$BC: w_{max}\left(x \geq l_f, t\right)=0; \frac{\partial {w_{max}}^4(0,t)}{\partial x}=\frac{256(\nu-1)\mu_f q_{inj}}{\pi G}$$

where C_l is the leak-off coefficient, τ is the time when the fluid begins leaking, and l_f is the fracture length. For a non-filter cake building fluid such as slickwater or polymer-free foam in a gas reservoir, the leak-off coefficient can be expressed as:

$$\mathrm{C}_l = C_{leak}\sqrt{\frac{K_f \Delta P \phi_r}{\mu_f}} \tag{5.15}$$

where $C_{leak}$is a unit-conversion constant, K_f is the effective permeability, ΔP is the differential leak-off pressure and ϕ_r is the rock porosity.

Proppant transport is calculated according to the following equation.

$$\frac{d(wc_p)}{dt}+\frac{d(V_x k_{retx} wc_p)}{dx}+\frac{d(V_z k_{retz} wc_p)}{dz}=0$$

$$IC: c_p(x,z,t=0)=0 \tag{5.16}$$

$$BC: \frac{\partial c_p}{\partial x}\left(\partial\Omega_{tip},t\right)=0;\ \frac{\partial c_p}{\partial z}(\partial\Omega_{bound},t)=0;\ c_p(\partial\Omega_{inlet},t)=c_{inj}$$

where w is the average fracture width, c_p is the proppant concentration (vol%), $\mathrm{V_x}$ is the horizontal velocity of the carrier fluid and $\mathrm{V_z}$ is the settling velocity of the proppant obtained from Eq. (5.7). k_{retx} and k_{retz} are retardation factors (Liu and Sharma, 2005) for modifying proppant velocities considering effects of inertia, fracture walls and proppant

concentration. Table 5.1 lists the cases for parametric study to evaluate the effect of the modified settling velocity correlation and foam drainage on proppant placement. Table 5.2 lists the shale gas reservoir properties and fracturing treatment parameters.

Table 5.1. Fracturing cases with different initial foam quality under various drainage condition

Case #	Foam Quality	Case Study Scenarios
5.1-0	0%	Slickwater case
5.1-1	70%	Original Stoke's Law with No Drainage
5.1-2	70%	Proposed Settling Correlation with No Drainage
5.1-3	70%	Proposed Settling Correlation with Low Drainage (Ro=0.02)
5.1-4	70%	Proposed Settling Correlation with Medium Drainage (Ro=0.05)
5.1-5	70%	Proposed Settling Correlation with High Drainage (Ro=0.10)
5.1-6	70%	Original Stoke's Law with High Drainage (Ro=0.10)
5.1-7	85%	Original Stoke's Law with High Drainage (Ro=0.10)
5.2-1	75%	Original Stoke's Law with No Drainage
5.2-2	75%	Proposed Settling Correlation with No Drainage
5.2-3	75%	Proposed Settling Correlation with Low Drainage (Ro=0.02)
5.2-4	75%	Proposed Settling Correlation with Medium Drainage (Ro=0.05)
5.2-5	75%	Proposed Settling Correlation with High Drainage (Ro=0.10)
5.3-1	80%	Original Stoke's Law with No Drainage
5.3-2	80%	Proposed Settling Correlation with No Drainage
5.3-3	80%	Proposed Settling Correlation with Low Drainage (Ro=0.02)
5.3-4	80%	Proposed Settling Correlation with Medium Drainage (Ro=0.05)
5.3-5	80%	Proposed Settling Correlation with High Drainage (Ro=0.10)
5.4-1	85%	Original Stoke's Law with No Drainage
5.4-2	85%	Proposed Settling Correlation with No Drainage
5.4-3	85%	Proposed Settling Correlation with Low Drainage (Ro=0.02)
5.4-4	85%	Proposed Settling Correlation with Medium Drainage (Ro=0.05)
5.4-5	85%	Proposed Settling Correlation with High Drainage (Ro=0.10)

Table 5.2. Formation properties and treatment parameters

Reservoir Properties		Treatment Parameters	
Shear Modulus, G	10 GPa	Clusters No / stage	5
Poisson's Ratio, ν	0.2	Injection Rate / Stage	80bpm (0.212 m^3/s)
Reservoir Depth	8500 ft (2591 m)	Pad Injection Time	20 min
Fracture height	270 ft (82 m)	Slurry Injection Time	40 min
Matirx Permeability	1000 nD	Proppant Size	20/40 (0.64 mm)
Pore Pressure Gradient	0.43psi/ft (9.8 kpa/m)	Proppant Density	3.36 g/cc
Fracturing Gradient	0.78psi/ft (17.6 kpa/m)	Proppant Loading	48 lbs/bbl (4 vol%)
Gas Filled Porosity	3%	Foam Quality	70-85%

5.4. RESULTS AND DISCUSSION

5.4.1 Foam Drainage and Proppant Settling

A series of conceptual foam drainage cases are analyzed with varying drainage rates. ϕ_g is assumed to remain constant after it reaches a maximum value of 95%. Figure 5.6 shows the estimated quality profiles of an initially 75% quality foam under with R_0 = 0.05, and Figure 5.7 shows the results of R_0 = 0.02 and 0.10. For low drainage rate with R_0 = 0.02, liquid accumulates at the bottom of the fracture after 40 mins, and foam quality profile is fairly smooth in the vertical direction. For medium drainage rate with R_0 = 0.05, the accumulation of liquid occurs earlier and the overall foam quality profile is altered significantly. For high drainage rate with R_0 = 0.10, severe liquid accumulation happens within 10 mins and the foam at the top drains to the maximum quality quickly.

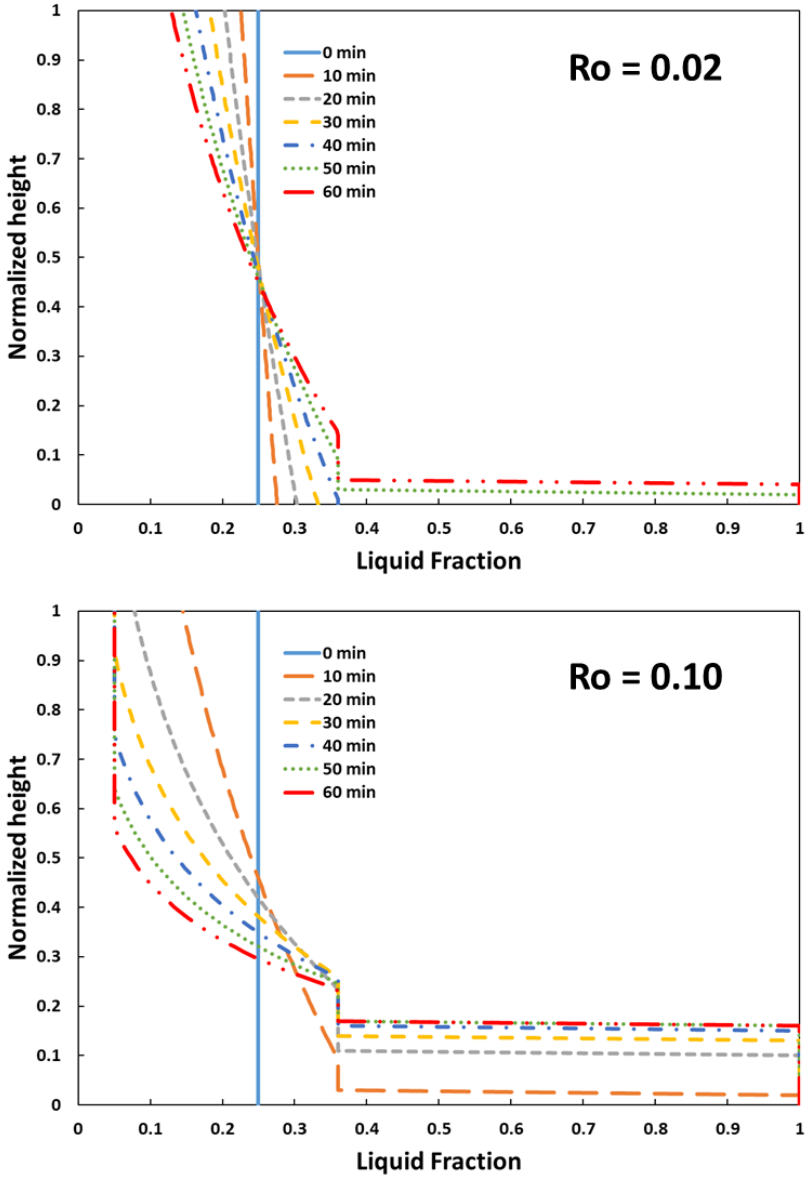

Figure 5.7: Effect of drainage rate on quality with an initial quality of 75%

Proppant settling in a dilute slurry (2.5 vol% proppant loading) under 42 s^{-1} shear rate is chosen to develop the proppant settling velocity correlation, and the details of the experiments could be found in our previous study (Tong et al., 2018). 75%, 80% and 85% proppant-free foam fluid was first injected into a Hele-Shaw slot and the effluent was

collected at three normalized slot heights, $\bar{z}$ = 0, 0.5 and 1. The effluent foam quality values were measured and plotted against $\bar{z}$, as shown in Figure 5.8.

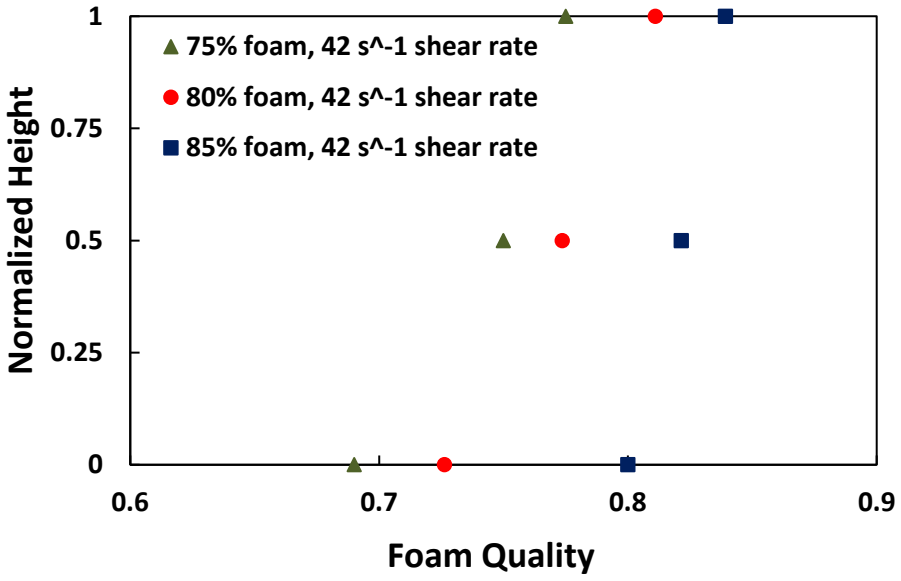

Figure 5.8: Vertical foam quality variation

Proppants were tracked in these experiments and their velocity was measured by a software called Tracker. In Figure 5.9, each data point represents an average value of 3 independent measurements and all data are summarized in Table 5.3. In Figure 5.9a, x-axis and y-axis indicate foam quality and proppant settling velocity, respectively. For individual cases, the proppant settles faster as the foam quality decreases. However, when comparing different cases, foam quality does not have a simple relationship to the proppant settling velocity. In Figure 5.9b, x-axis and y-axis indicate proppant settling velocity and normalized slot height, $\bar{z}$. Because few proppants were at the top part of the slot, no data was collected for $\bar{z} > 0.5$. The vertical position of the proppant affects the settling of the proppant.

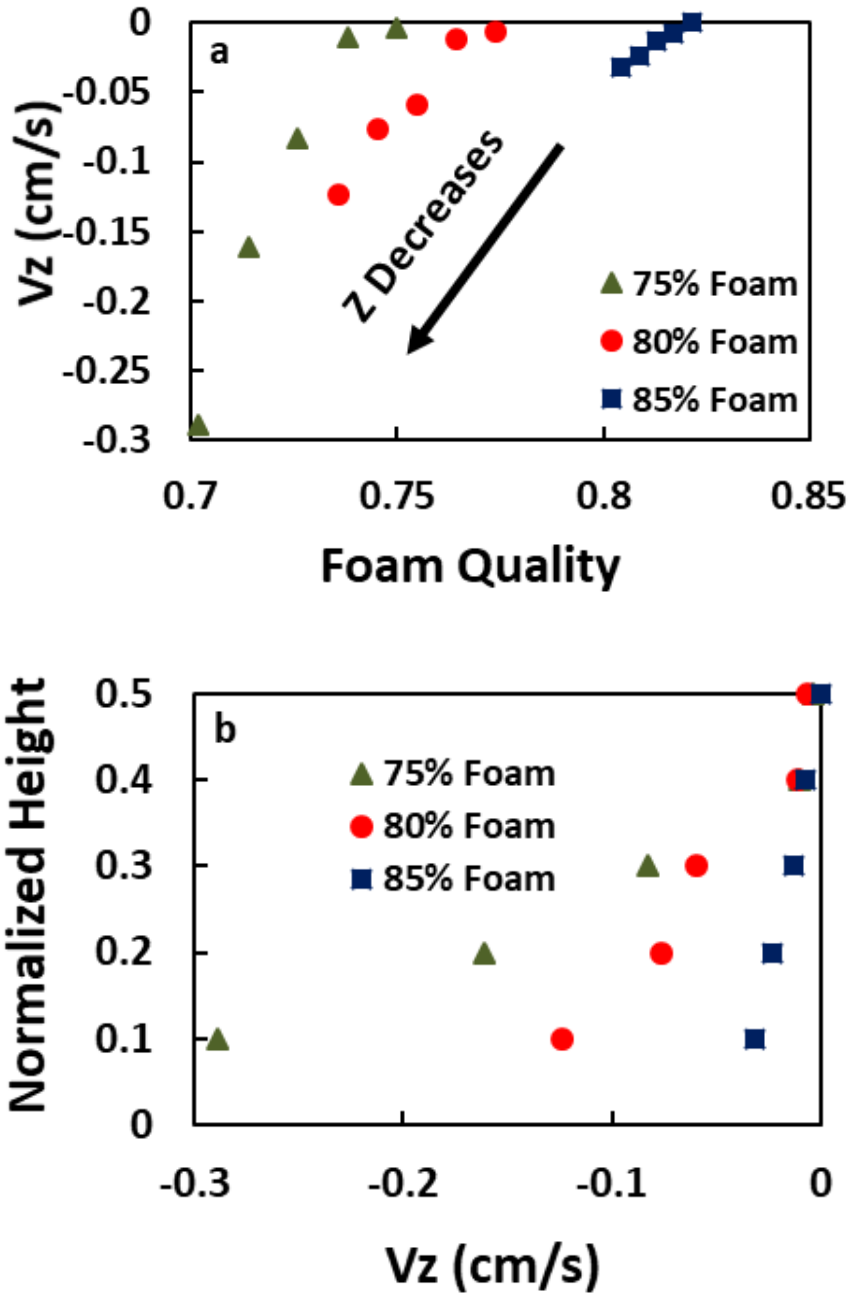

Figure 5.9: Proppant settling velocity against foam quality at various $\bar{z}$ positions

The dependence of proppant settling velocity V_z on horizontal velocity (V_{xn}) and local foam x-velocity gradient in the z direction ($\frac{dV_{xn}}{d\bar{z}}$) is explored in Figure 5.10. In Figure

5.10a, x-axis and y-axis indicate V_{xn}, the normalized x-velocity of proppant (V_x/V_{x_foam}), and the normalized slot height $\bar{z}$, respectively. V_x is the measured x-velocity of the proppant, and V_{x_foam} is the nominal x-velocity of the foam (injection rate / cross-sectional area). Points shown in Figure 5.10 are average values from three independent measurements. Table 5.3 summarizes average values of local foam quality, velocity gradient term $\left|\frac{dV_{xn}}{d\bar{z}}\right|$ and proppant settling velocity from three independent measurements. This data is fitted to the empirical correlation in Eq. (5.7) to obtain a_0 = -125.8, b_0 = 3.831, c_0 = 0.7141 with a correlation coefficient, R^2 = 0.977.

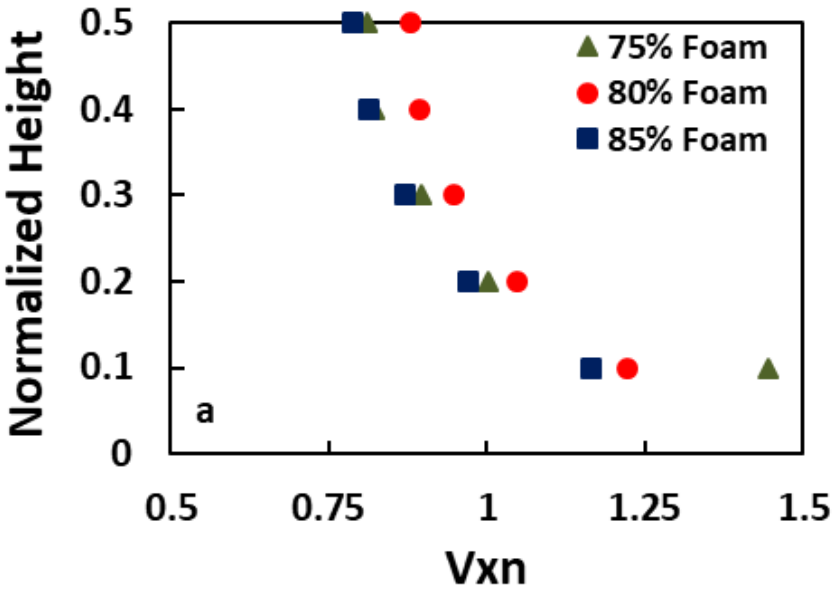

Figure 5.10: Proppant settling velocity against the velocity gradient term $\left|\frac{dV_{xn}}{d\bar{z}}\right|$

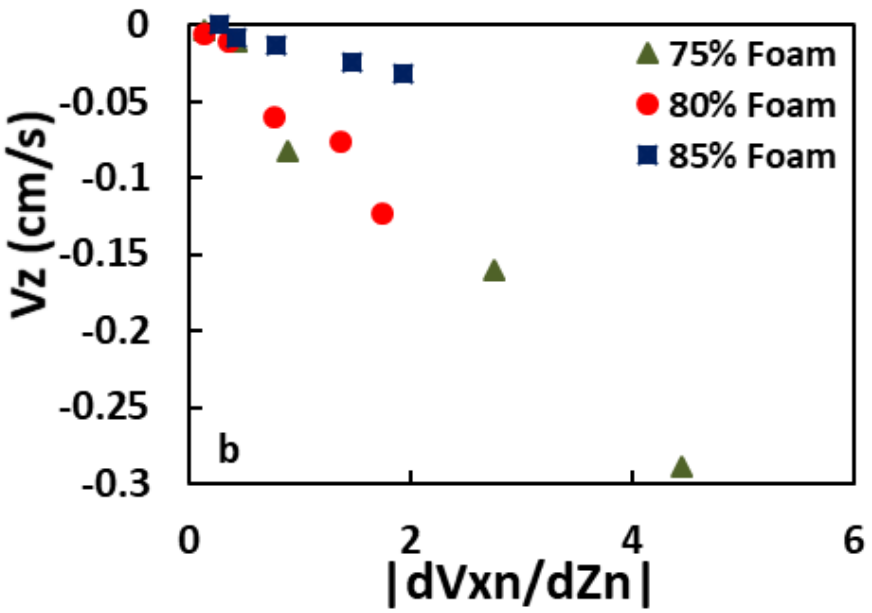

Figure 5.10: Continued

Table 5.3: Summary of average data for settling velocity correlation development

$\bar{Z}$	75% foam			80% foam			85% foam		
	ϕ_g	$\left\|\frac{dV_{xn}}{d\bar{z}}\right\|$	Vz (cm/s)	ϕ_g	$\left\|\frac{dV_{xn}}{d\bar{z}}\right\|$	Vz (cm/s)	ϕ_g	$\left\|\frac{dV_{xn}}{d\bar{z}}\right\|$	Vz (cm/s)
0.1	0.702	4.447	-0.2888	0.736	1.746	-0.1235	0.804	1.937	-0.0318
0.2	0.714	2.755	-0.1607	0.745	1.363	-0.0766	0.809	1.466	-0.0236
0.3	0.726	0.890	-0.0827	0.755	0.771	-0.0595	0.813	0.778	-0.0129
0.4	0.738	0.427	-0.0103	0.764	0.352	-0.0112	0.817	0.416	-0.0076
0.5	0.750	0.137	-0.0034	0.774	0.140	-0.0060	0.821	0.272	0.0000

Figure 5.11 shows the fit of the data with the correlation. Proppants settle faster as: (1) ϕ_g decreases; (2) $\left|\frac{dV_{xn}}{d\bar{z}}\right|$ increases; (3) d increases; (4) $\frac{\rho_s}{\rho_f}$ increases. Figure 5.12 shows the calculated velocity from the correlation vs. the experimental velocity. This proppant settling correlation is used in the fracturing model.

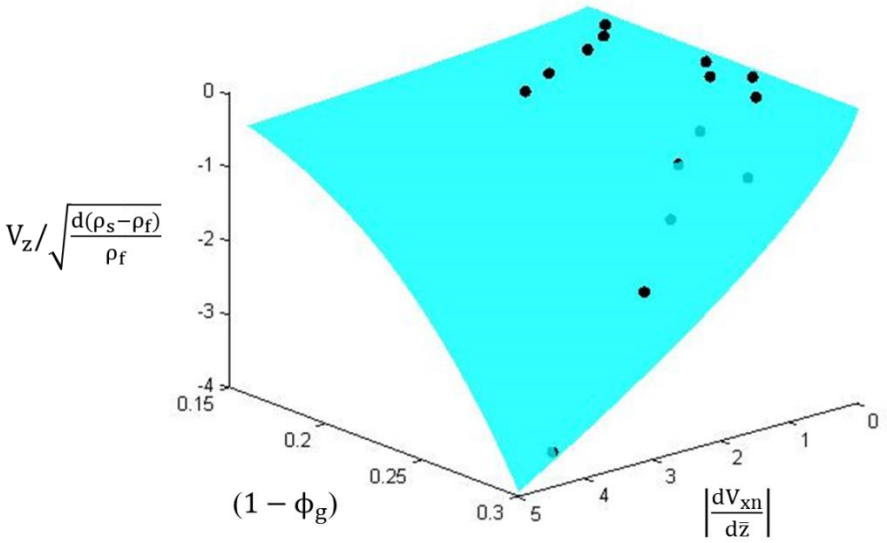

Figure 5.11: Comparison of experimental settling velocity and the correlation under the best curve fit scenario

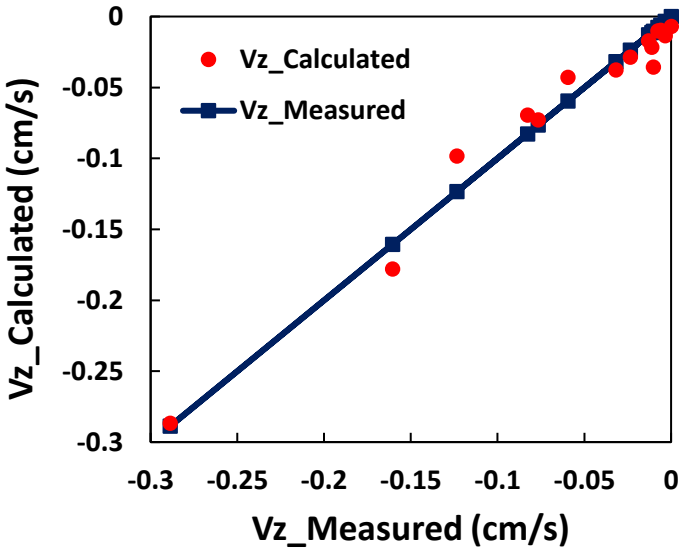

Figure 5.12: Measured settling velocity of proppant against calculated settling velocity of proppant

5.4.2 Fracturing Modeling

Eqs. (5.14) and (5.16) are solved to model fracture propagation and proppant transport at the field-scale. Figure 5.13 shows the proppant placement of case 5.1-0 and 5.1-1 at the end of slurry injection (40 min, excluding pad injection time), and the colors represent the proppant volume concentration, varying from 0 to 0.64. In slickwater (case 5.1-0), most of the proppants settle near the wellbore and a proppant bed is formed at the bottom 10 m of the fracture. In case 5.1-1, no proppant bed was formed and a uniform proppant distribution is achieved with 70% foam. Figure 5.13 demonstrates that foam is effective in carrying proppants compared to slickwater.

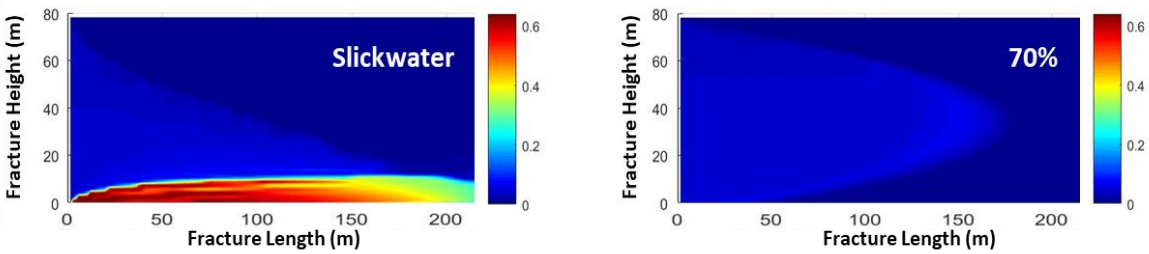

Figure 5.13: Proppant volume concentration for slickwater and 70% quality foam with original settling law under no drainage condition (Ro = 0) at 40 min

Figure 5.14 shows the proppant volume concentrations for 70%, 75%, 80% and 85% quality foams (Cases 5.1-1, 5.2-1, 5.3-1 and 5.4-1) predicted by the original Stokes' law with no drainage, and the colors represent the proppant volume concentration, varying from 0 to 0.1. For each case, the proppants move faster in the middle than at the top or bottom. As the foam quality increases, proppants move slower because the foam viscosity increases. Figure 5.15 shows the proppant volume concentrations for 70%, 75%, 80% and 85% quality foams (Case 5.1-2, 5.2-2, 5.3-2 and 5.4-2) predicted with the proposed settling correlation with no drainage. The proppants settle slower as they approach the middle of

the fracture where the $\left|\frac{dV_{xn}}{d\bar{z}}\right|$ term gets closer to zero. Therefore, proppant concentrated zones are found at the middle of the height with the proposed settling correlation, especially in 70% and 75% quality foams. For foam quality above 75%, the difference between the predictions from the new and old settling correlations vanishes.

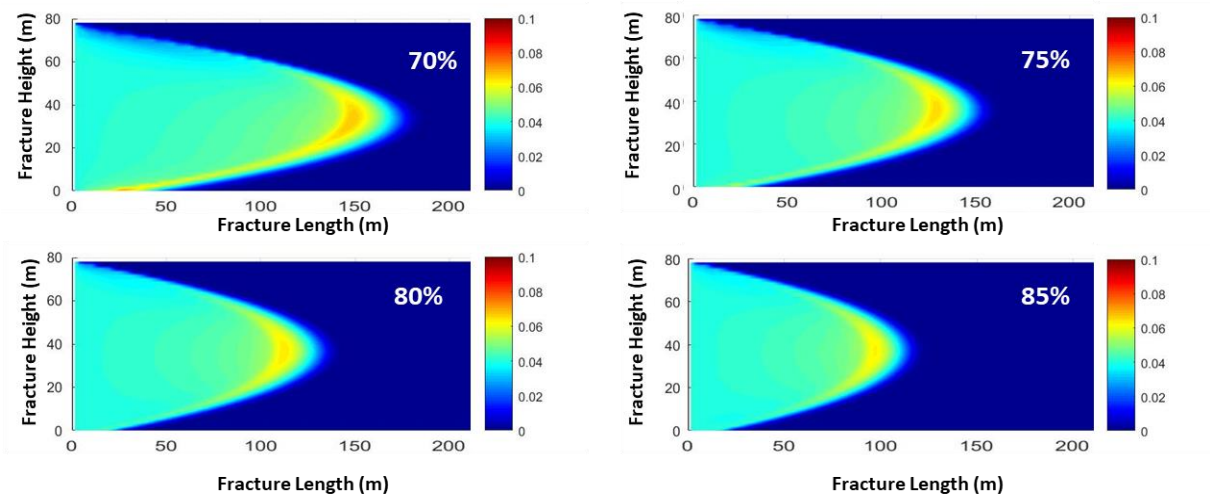

Figure 5.14: Proppant volume concentration for different initial quality foam with original settling law under no drainage condition (Ro = 0) at 40 min

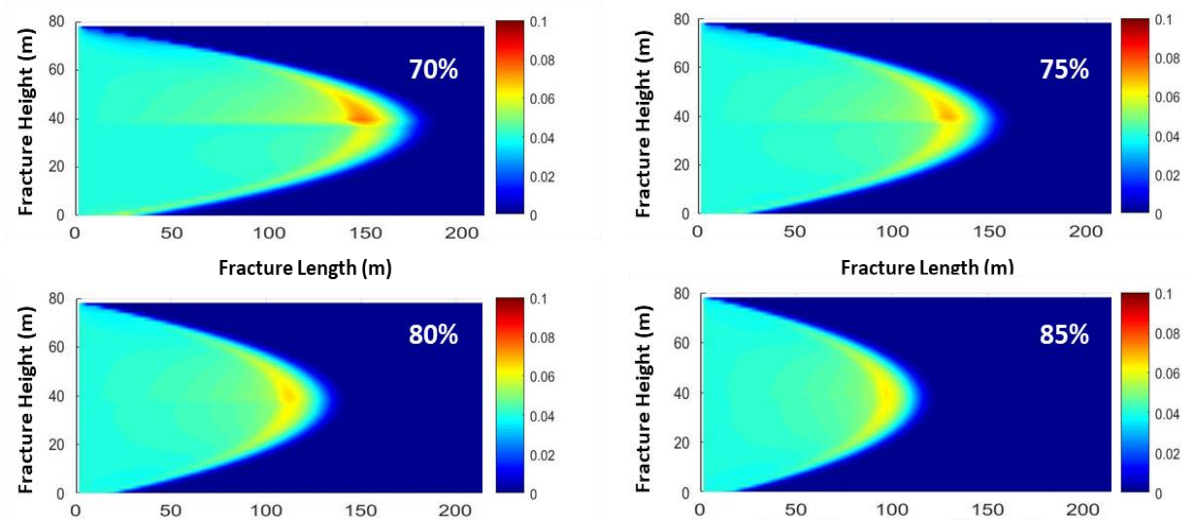

Figure 5.15: Proppant volume concentration for different initial quality foam with proposed settling correlation under no drainage condition (Ro = 0) at 40 min

The proppant placement is studied next for non-zero foam liquid drainage rates. Figures 5.16 – 5.18 are the proppant areal concentrations at low (Ro=0.02, Case 5.1-3, 5.2-3, 5.3-3,5. 4-3), medium (Ro=0.05, Case 5.1-4, 5.2-4, 5.3-4, 5.4-4), and high drainage rates (Ro=0.10, Case 5.1-5, 5.2-5, 5.3-5, 5.4-5) with the proposed settling correlation. The colors represent the proppant volume concentration, varying from 0 to 0.64.

For foam at low drainage rate condition (Figure 5.16), the final proppant distribution is relatively uniform and similar to that without drainage. As the drainage rate increases, a liquid layer forms quickly at the bottom of the fracture and leads to increase in proppant concentration at the bottom. Generally speaking, the proppant distribution gets less uniform as the foam quality decreases or the drainage rate increases. In addition, a highly concentrated proppant zone forms in the middle of the fracture under medium to high drainage condition.

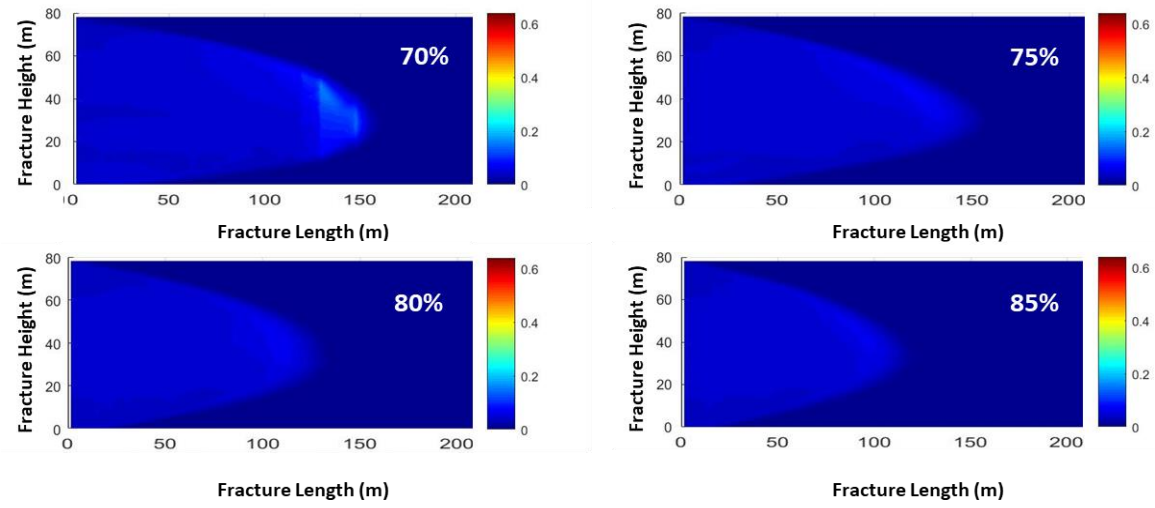

Figure 5.16: Proppant volume concentration for different initial quality foam with proposed settling correlation under low drainage condition (Ro = 0.02) at 40 min

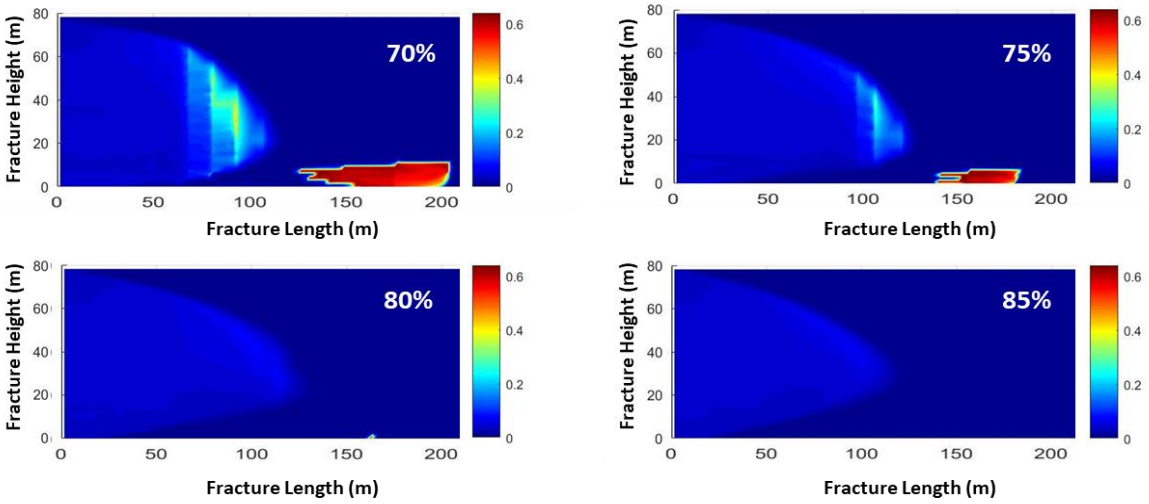

Figure 5.17: Proppant volume concentration for different initial quality foam with proposed settling correlation under median drainage condition (Ro = 0.05) at 40 min

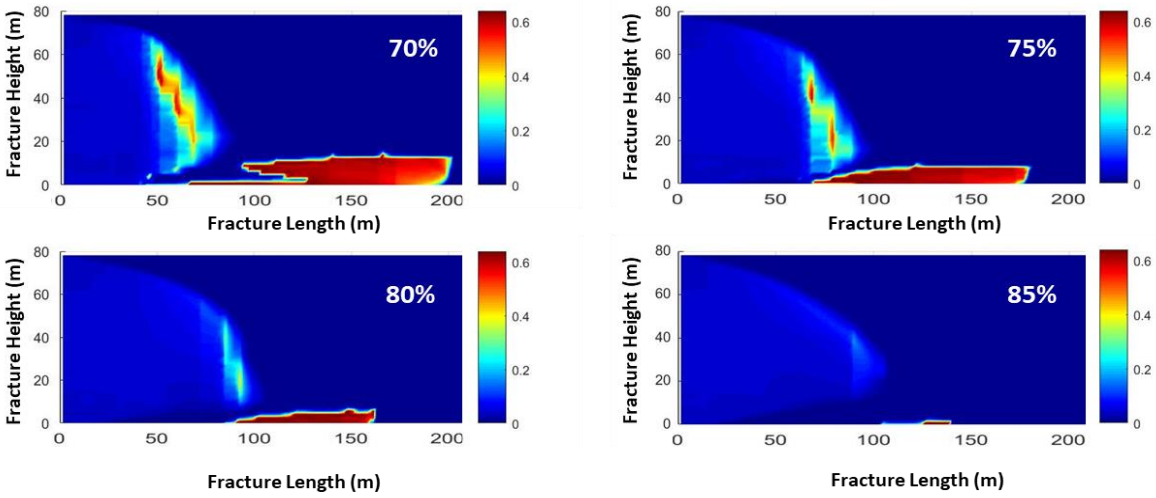

Figure 5.18: Proppant volume concentration for different initial quality foam with proposed settling correlation under high drainage condition (Ro = 0.10) at 40 min

Figure 5.19 shows the proppant settling in high drainage foam with original Stokes' law (Case 5.1-6 and 5.1-7). These cases should be compared with Figure 5.18 plots of the same quality foam. The comparison shows that in wet foams, the original Stokes' law predicts a

faster proppant settling and a larger proppant bed formation. As the foam quality increases, the effect of settling law diminishes.

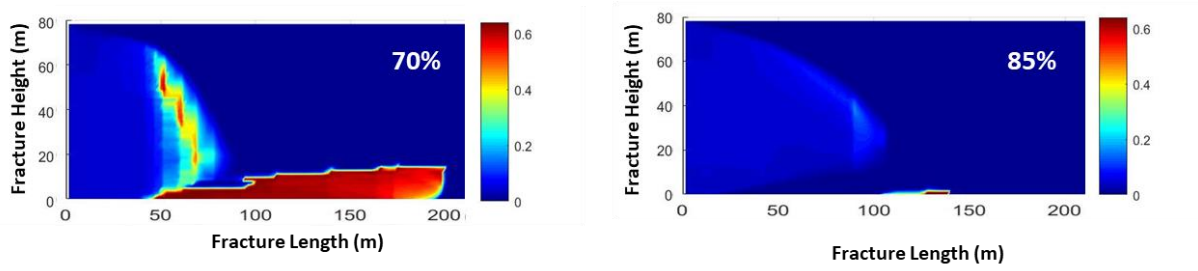

Figure 5.19: Proppant volume concentration for 70% and 85% quality foam with original settling correlation under high drainage condition (Ro = 0.10) at 40 min

Figure 5.20 shows the proppant volume concentration, horizontal foam velocity and foam quality for 75% foam under medium drainage condition against time. The timeframe indicates the slurry injection time after the initial pad stage. Unlike Figures 5.14 – 5.18, there are white regions in Figure 5.20, and these regions indicate unfractured matrix (and therefore no x velocity and foam quality profile). A liquid layer starts to form at the bottom around 100 m deep in the fracture; a large velocity liquid regime is also observed at the same place. As time progresses, the proppants gradually settle in that region and form a proppant bed at the bottom of the fracture. Such settling is avoided in higher quality foams (85% quality in Figure 5.18).

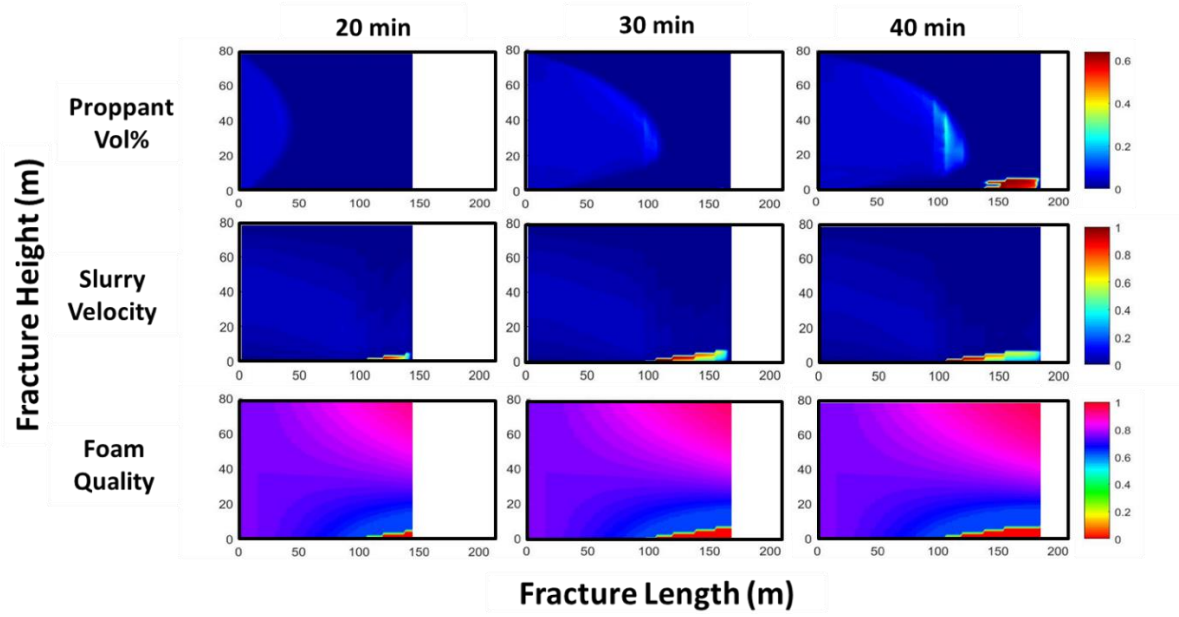

Figure 5.20: 75% foam with proposed settling correlation under median drainage condition (Ro = 0.05). Top three plots: proppant volume concentration with color ranges from 0 to 0.64; middle three plots: foam x velocity with color ranges from 0 to 1.0 m/s; bottom three plots: foam quality profile with color ranges from 0 to 1.

5.5. CONCLUSIONS

In this work, a foam drainage model and a proppant settling correlation in foam are developed and incorporated into an in-house fracturing simulator to evaluate proppant placement in foam fracturing treatment at the field scale. However, this study still has several limitations including: first, the settling correlation is developed at ambient condition, and more rigorous experiment at reservoir condition should be conducted to fully understand proppant settling in field treatment; second, foam drainage experiment should be properly designed to optimize the scaling function for a more realistic drainage profile; third, the fracturing modeling is fairly simple, and a fully 3D fracturing modeling should be used for future study; finally, the simulations are made under the assumption that

the proppants do not affect the structure of the foam, and the interaction between proppant and bubbles at concentrated condition should be evaluated. Overall, the following conclusions are reached in this work.

1. Foam is not a single phase fluid, and the concept of apparent foam viscosity and Stokes' law are misleading for calculating proppant settling velocity in foam.

2. Proppant settling velocity is found to depend on foam quality and the foam velocity gradient term, $\frac{dV_{xn}}{d\bar{z}}$. Proppants settle slower as the foam quality increases or the velocity gradient term decreases.

3. Foams carry proppants deep and high into the fractures. In slickwater, most of the proppants settle near the wellbore and a proppant bed is formed at the bottom 10 m of the fracture.

4. Foam drainage process alters the foam quality profile during fracturing treatments. The liquid from the foam collects at the bottom where the proppants settle fast and form a proppant bed.

5. Foam drainage effect is more detrimental to the proppant distribution as the foam quality decreases. To achieve uniform proppant distribution foams of quality 85% or higher should be used.

Nomenclature

F force

ϕ_g gas volume fraction

ϕ_l liquid volume fraction

γ line tension of bubble film

d particle diameter

A bubble area

λ	friction coefficient
f	scaling function
R_0	drainage rate index
$\bar{z}$	normalized fracture height
t	drainage time
w	weighing factor
ρ	density
μ	viscosity
K	consistency index
n	power-law index
P	pressure
w	fracture width
h	fracture height
ν	possion's ratio
G	shear modulus
σ_{hmin}	minimum horizontal stress
q	volumetric flow rate
c	particle concentration
x	fracture length
l_f	total length of half fracture
C_l	leak-off coefficient
τ	time when leak-off begins
C_{leak}	unit-conversion factor

K_f filtrating permeability of the effective fracturing fluid

ϕ_r rock porosity

V velocity

k_{ret} retardation factor

Chapter 6: Chemical Stimulation for Enhanced Fracture Conductivity

6.1 SUMMARY

During hydraulic fracturing treatments, proppants often settle near-wellbore in low viscosity fracturing fluids and leave a large fractured surface unpropped. Poor placement of proppant could lead to a loss of fracture conductivity and undermine the productivity of shale wells. In addition, lots of secondary fractures are too narrow to accommodate commercial proppants and would close during production.

Organic shales often contain a significant amount of calcite. Two chemical stimulation technologies, which target the calcite portion of shale, have been proposed and evaluated in this chapter. The first technology is microencapsulated acids (MEA) for shale acidizing application. Unlike aqueous hydrochloric acid systems which could cause shale softening and excessive mud generation, the MEA system was able to increase fracture conductivity without detrimental formation damage. The second technology is in-situ proppant generation (IPG) through hydrothermal reaction. This reaction has been extensively studied in medical research on forming human bone substitution materials by converting natural calcite-rich materials such as corals and egg shells.

Our results showed that both MEA and IPG could lead to significant increase fracture conductivity without sacrificing shale integrity. In the MEA system, due to the heterogeneity of encapsulation placement and its release, large and isolated etched patterns on fracture surface could be developed and lead to increase in fracture conductivity. In the IPG system, mineral crystals could grow as large as common commercial proppant, and a moderate increase (3x – 10x) in fracture conductivity was observed.

This chapter is based on two publications, and Dr. Mohanty supervised the two projects.
An accepted journal paper (Singh, Tong, Panthi, and Mohanty, 2019). Singh and Tong did the experiments together, and Singh wrote a larger fraction of the paper. Panthi helped with the experiments.
A conference paper (In preparation for journal, Tong, Miller, and Mohanty). Miller helped the writing.

6.2 INTRODUCTION

Chemicals are widely used in well-stimulation techniques to improve well productivity, and acid is a common choice (Daccord et al., 1989; Tripathi and Pournik, 2014). In shales, it involves injecting acids into the fractures which can react with minerals present on the fracture surface such as calcite and dolomite to create micro-channels or etching on the fracture surface (Wu and Sharma, 2017a). This acid-induced surface roughness creates conductive pathways for hydrocarbon flow even after fracture closure. The injected acids can penetrate deeper into the fractures as well as microfractures and does not encounter gravity segregation issues (as opposed to proppants). Despite these advantages, one of the critical challenges of this process is to avoid over-reaction of the acids with the shale which could lead to bulk shale disintegration rather than non-uniform surface etching. The excessive acid reaction could also result in softening of shale making them susceptible to complete fracture closure (even with a rough surface). The other concern is to minimize damage to surface equipment and wellbore due to concentrated acids. Therefore, typically retarded acid systems such as emulsified or foamed acids are also commonly used in field applications (Cairns et al., 2016; Nasr-El-Din et al., 2000; Taylor and Nasr-El-Din, 2003). However, the most commonly adopted method is acid-in-oil emulsions. Since conventionally surfactants are used to stabilize these emulsions, achieving thermal stability under harsh reservoir conditions (low pH due to acids, high reservoir temperature and salinity) is quite challenging.

Recently, injecting polymer based solutions into fractures to generate polymeric particles as in-situ proppants has been proposed (Chang et al., 2015). The benefit of generating in-situ proppant from aqueous solution is significant because it can avoid any physical or geometry restriction due to aperture variation of the fractures. According to Chang et al. (2015), the size and formation time of these particles could be nicely

controlled, and usually these particles are spherical in shape and can be much larger than the size of commercial proppants. They also investigated the mechanical property of the gel-proppant pack (in laboratory setting) but found that these polymer proppants could be too deformable to prop the fractures at reservoir conditions.

In this chapter, we propose two chemical stimulation techniques to improve fracture conductivity. The first one is a Pickering emulsion approach to stabilize colloidal systems in order to encapsulate acids (Singh et al., 2018). Such particle-stabilized colloids have shown outstanding stability and resistance to coalescence as compared to surfactant-stabilized systems even under harsh reservoir conditions (Panthi et al., 2017; Singh et al., 2017). In the air-water-particle system, the emulsion-type of the colloid is governed dominantly by the surface-wettability of the particles characterized by the contact angle (Θ). If the particles are hydrophilic in nature ($\Theta < 90$), they have the affinity to stabilize air-in-water emulsion (aqueous foams). On the contrary, if the particles are hydrophobic in nature ($\Theta > 90$), they can stabilize water-in-air emulsion (Binks and Murakami, 2006) as shown in Figure 6.1a. These emulsions are often referred in the literature as "dry water" owing to their dry appearance and free-flowing characteristic like a powder (Figure 6.1b).

The surface morphology of the MEA was also characterized in a previous study of our group (Panthi et al., 2017; Singh et al., 2017). Figure 6.1c shows a Scanning Electron Microscopy (SEM) image of the MEA system under high vacuum condition. However, high vacuum conditions could lead to water evaporation inside the MEA (Forny et al., 2007) which could possibly collapse the silica shell (Carter et al., 2011). Figure 6.1d shows a scan from Confocal Laser Scanning Microscopy (CLSM), which is a non-invasive technique (no vacuum needed) widely used for imaging diverse colloidal systems such as foams and emulsions (Singh and Mohanty, 2015).

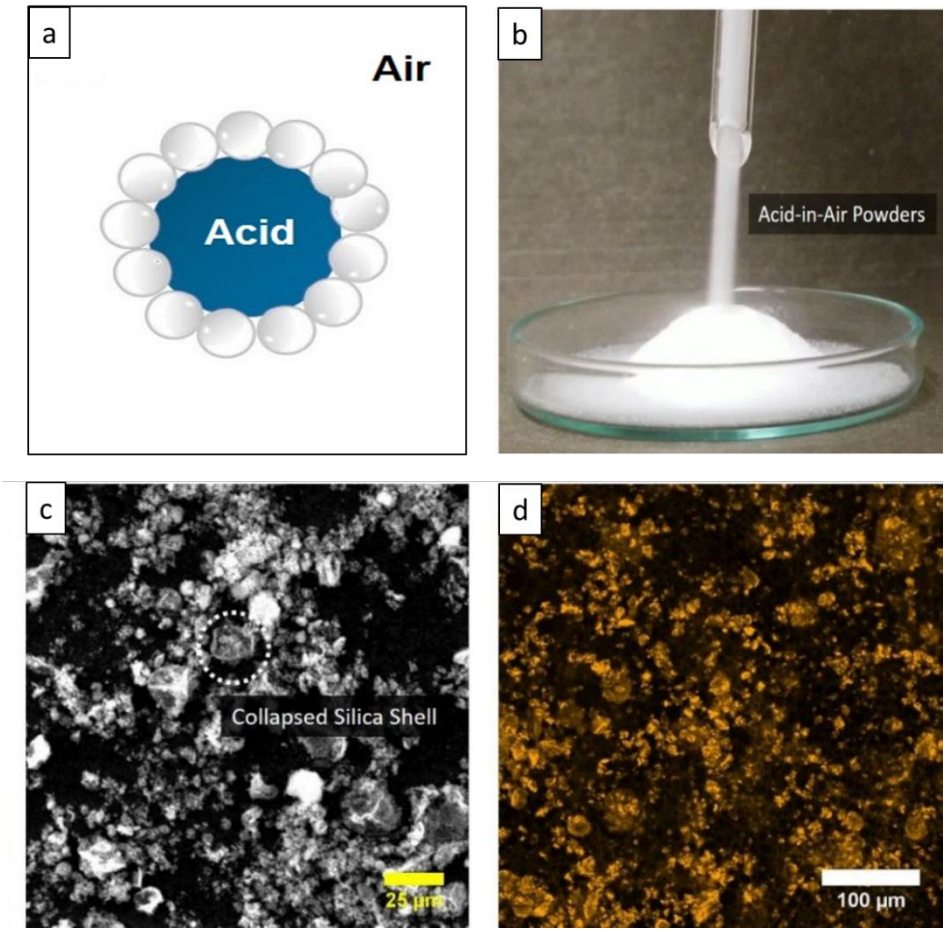

Figure 6.1: (a) schematic of acid-in-air powder (white sphere represents the silica nanoparticles); (b) free-flowing MEA; (c) SEM image of the MEA (scale bar is 25 µm); (d) confocal micrograph of the MEA (scale bar is 100 µm)

Besides, the superior thermal stability and delayed release of the MEA system have been successfully demonstrated (Singh et al., 2017). In this chapter, the objective is to evaluate the performance of MEA in stimulating the microfractures of calcite-rich shale rocks through a series of fractured shale core experiments. Fracture conductivity and shale surface topology were compared before and after MEA treatment.

The second stimulation method is a hydrothermal reaction which could form hydroxyapatite (HAp) crystals from calcite components in shales. Hydroxyapatite

($Ca_{10}(PO_4)_6(OH)_2$) is the main inorganic component of human bones and ranks 5 in Mohs hardness scale. Calcite can be converted to HAp through hydrothermal dissolution/precipitation reactions (Roy and Linnehan, 1974; Yoshimura et al., 2004). Corals, seashells and other calcite-rich materials have been converted to hydroxyapatite in other applications (Sassoni et al., 2011; Sivakumar et al., 1996; Vecchio et al., 2007) including synthesis of bone substitutes and carbonate statue protection. In this chapter, this reaction is first proposed to generate in-situ proppant for fracturing applications. A series of batch reactions and reactive fractured core experiments are conducted with both reservoir and outcrop shale samples.

6.3 METHODOLOGY

6.3.1 Shale Samples

Rock samples from a shale oil reservoir and its outcrop were used in this study. Figure 6.2a shows a typical shale fragment prepared for batch reaction experiments. The white lines / regions are calcite-rich. Table 1 lists the mineralogy quantified with X-ray diffraction (XRD); more than 50 wt% of the mineral is calcite. Figures 6.2b and 6.2c show SEM images of the shale surface at different resolutions, and plenty of calcite layers and islands could be observed. Figure 6.3 shows a typical shale core sample for reactive fractured core experiments. The diameters of the core samples are all identical at 1 inch, and the lengths of the core samples range from 3.2 inch to 4 inch.

Table 6.1: X-ray diffraction data of the shale used in this study (Minerals less than 0.1% were included in others.)

Calcite	Dolomite	Anhydrite	Quartz	Albite	Pyrite	Clay	Others
55.89	0.78	0.68	17.47	7.29	2.57	15.10	0.22

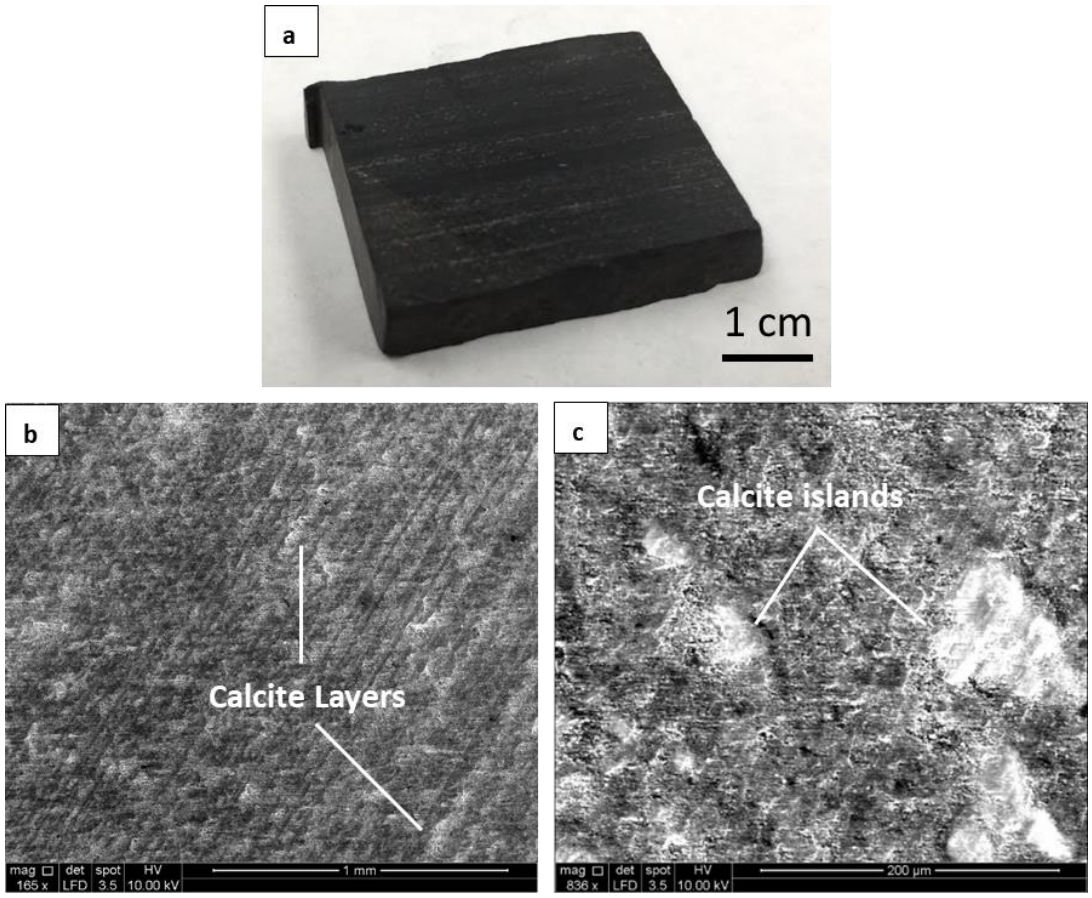

Figure 6.2: (a) Photograph of a shale fragment, (b) SEM at a lower resolution, (c) SEM at a higher resolution

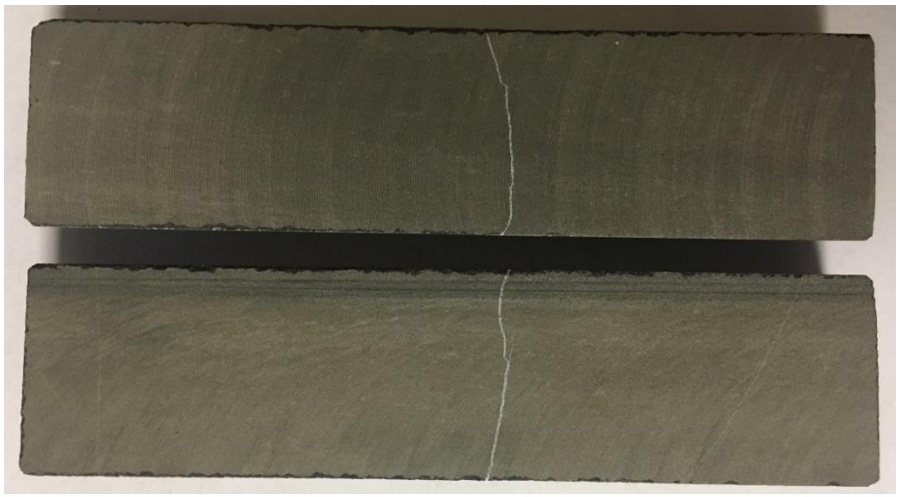

Figure 6.3: Typical shale core samples for reactive fractured core experiments

6.3.2 Microencapsulated Acids

6.3.2.1 Materials

Silica nanoparticles coated with polydimethylsiloxane were used in this study. The surface coating makes the nanoparticles highly hydrophobic. The nominal size of the primary particles was 14 nm. Deionized water with a resistivity greater than 18.2 MΩ-cm obtained from Barnstead^{TM} E-Pure^{TM} DI system was used to prepare solutions. Hydrocholoric acid (37%, Sigma-Aldrich) and Sodium Chloride (Fisher Chemical) were used as received.

6.3.2.2 Encapsulation of Acids

The silica nanoparticles and hydrochloric acid aqueous solution (different acid concentrations + 1 wt% sodium chloride) were mixed vigorously in the ratio of 1:50 by weight using a blender operating at 16000 rpm for 45 seconds. The blending process could make self-assembly of silica nanoparticles on the water-air interface leading to the formation of water-(acid solution)-in-air powders (Figure 6.1a).

6.3.2.3 Reactive Fractured Core Experiments

The objective of this experiment was to quantify the change in fracture conductivity due to acid-induced surface etching. The shale core sample was cut into two pieces as shown in Figure 6.3, and then put back together without any proppant to mimic unpropped natural or induced fractures. First, the initial conductivity of the fractured core was measured. The core, covered with a heat-shrink wrap, was placed in a Hassler coreholder. A constant overburden pressure of 500 psi was applied, and conductivity was measured using brine (4 wt% NaCl) at ambient conditions. The core was then taken out of the holder and was prepared for an acid treatment. In field application, the release of acid from acid-

in-powders can be triggered via mechanical crushing during fracture closure. In order to mimic this under laboratory conditions, an overburden pressure-induced crushing was performed. It is to be noted that since it is difficult to mimic the leak-off of external carrier fluid, the MEA was manually placed in the fracture rather than injected in a slurry form. An acid-resistant O-ring was positioned on the fracture boundary and MEA (around 1.6 gm for a 4-inch long core sample) was placed uniformly inside the O-ring, as shown in Figure 6.4a. The fractured cores were again put back together and were covered with heat-shrink wrap (Figure 6.4b). The core was placed in the coreholder and was kept in an oven operating at 80 °C. A constant overburden pressure of 200 psi was applied to induce the in-situ pressure-triggered release of the acids (Figure 6.4c). The system was left in the oven for 24 hours to react. The core was again removed from coreholders, and the O-ring and compressed MEA were removed. The core was again put back into a core holder and the conductivity was again measured at 500 psi overburden pressure. Table 6.2 lists all fractured core experiments with MEA system.

Table 6.2: Experiments of reactive fractured core experiments in MEA cases

Shale Type	**Outcrop**	**Outcrop**	**Outcrop**
Expt. #	1	2	3
Core length	4.0	4.0	4.0
Acid wt%	0.5	10	15

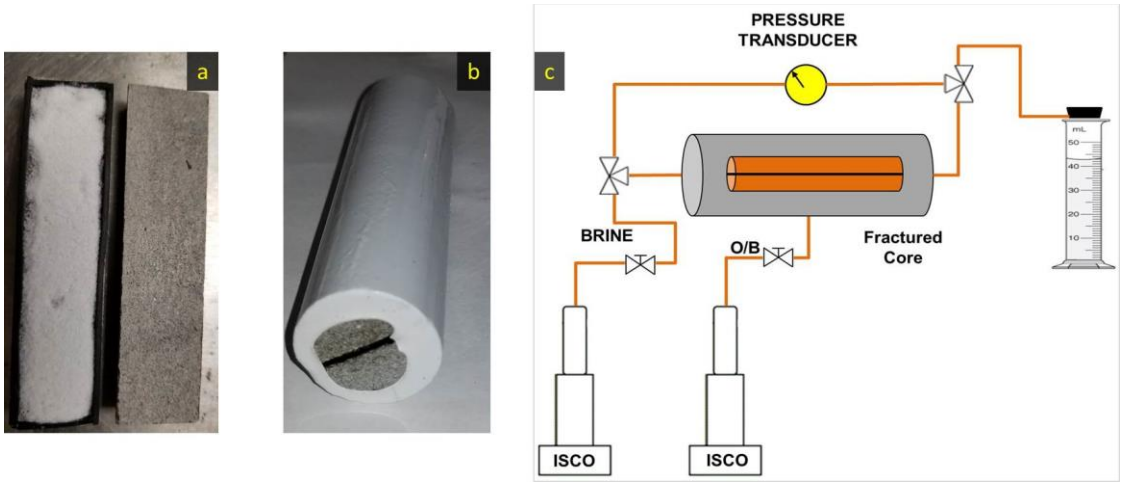

Figure 6.4: (a) Microencapsulated acid placed on fractured shale core; (b) Heat-shrink wrapped core; (c) experiment set up to measure conductivity of the fractured core under closure.

6.3.2.4 Fracture Surface Topology

When a concentrated acid interacts with a shale surface, which is typically contains calcite, it leads to surface etching which could be characterized using the surface roughness. The shale surface roughness was quantified using the Wyko NT9100 optical profilometer. In addition, optical microscopy was used to qualitatively characterize the surface topology. Bright-field images of the fractures surface were captured using a Nikon optical microscope equipped with a high-resolution camera. The fracture faces of the shale cores were analyzed before and after the MEA treatments.

6.3.3 In-situ Proppant Generation

6.3.3.1 Materials

Synthetic brines were made with reagent-grade salts from Fisher Scientific. A low salinity soft brine (2,500 ppm NaCl, close to frac water composition) and a high salinity brine (13700 Na^{+}, 1620 Mg^{2+}, 520 Ca^{2+}, 24470 Cl^{-} and 3310 SO_4^{2-}, all in ppm, representing

a mixture of frac water and formation brine) were used in this study. Two chemicals (H and D) were added to the brines for the reaction with shales. Chemical H is an acid (phosphoric acid) and chemical D is a salt (diammonium phosphate).

6.3.3.2 Batch Reaction Experiments

The two chemicals H and D were mixed in the brines and shale fragments were added to this mixture. The target mineral is hydroxyapatite (HAp), and it is rarely obtained with perfect stoichiometry and is usually found as carbonated, calcium-deficient HAp, in which carbonate ions have replaced some of the phosphate or hydroxide ions in the lattice. A calcium deficiency exists to compensate for charge imbalance and create thermodynamic stability. HAp has both very low solubility ($K_{sp} \sim 10^{-59}$ at 25 °C) and low dissolution rate in acid ($R_{diss} \sim 10^{-14}$ moles·cm^2·s^{-1} at 25 °C). Both its solubility and dissolution rate are significantly lower than those of calcite (Sassoni et al., 2011). The chemical reactions are listed in Eqs. (6.1) and (6.2).

$$10CaCO_3 + 6H_3PO_4 \rightarrow Ca_{10}(PO_4)_6(OH)_2 + 10CO_2 + 8H_2O \quad (6.1)$$

$$10CaCO_3 + 6(NH_4)_2HPO_4 + 2H_2O \rightarrow Ca_{10}(PO_4)_6(OH)_2 + 6(NH_4)_2CO_3 + 4H_2CO_3 \quad (6.2)$$

Table 6.3 shows the list of experiments with the amounts of the chemicals in brine. The ratio between chemical H to chemical D was kept at least 1:1 to ensure the solution was acidic. The mass ratio between the solution to the shale was maintained at 2:1, and the vials were kept in an oven at 80 °C (~reservoir temperature) for 24 hours. After the experiment, the shale samples were dried at the room temperature and then analyzed with a scanning electron microscope (SEM).

Table 6.3: Weight % of chemical H and chemical D in batch experiments.

Expt. #	4	5	6	7	8	9	10	11	12
H wt%	1	2	3	1	2	3	2	3	3
D wt%	0	0	0	1	1	1	2	2	3

6.3.3.3 Reactive Fractured Core Experiments

The chemicals were injected through fractured shale core samples to mimic injection of chemicals into microfractures in shale reservoirs. The proppants were formed in situ inside the fracture. The change of fracture conductivity was measured before and after the treatments. Both reservoir shale samples and outcrop shale samples were used in this study. Table 6.4 lists all the reactive fractured core experiments conducted.

The first step in the experiment was to measure the pre-treatment brine conductivity of the unpropped fracture at room temperature under an overburden pressure (1000 psi), as shown in Figure 6.4c. After the first step, the core was taken out of the core holder and reassembled with two rubber spacers at the sides of the fracture aperture to mimic the conditions during stimulation fluid injection (before fracture closure). The whole core assembly was wrapped with a heat shrink tube and a Hassler sleeve and placed inside the core holder. The coreholder was placed inside an 80 °C oven. Then the chemical formulation was injected into the fractured core for a time period followed by a shut-in period (similar to field stimulation processes) of 24 hours. Then the core was taken out of the coreholder and the rubber spacers were removed and the core was reassembled again in the coreholder. Then the post-treatment brine conductivity of the fracture was measured at the same overburden pressure.

Table 6.4: Core samples of reactive fractured core experiments in IPG cases

Shale Type	Reservoir	Reservoir	Reservoir	Outcrop	Outcrop	Outcrop
Expt. #	13	14	15	16	17	18
Core length	3.5	3.4	3.2	4.0	4.0	4.0

6.3.3.4 Brinell Hardness Measurement

The shale Brinell hardness number (BHN) was measured using a modified indentation test adapted from the standard method for hardness measurement on metallic materials (ASTM E10-15a). A 4 mm diameter tungsten carbide sphere indenter was used to apply load on shale surface at a constant displacement rate of 0.003 inch/min. Since the reaction primarily occurs on the surface of the shale samples, a small load should be used to avoid deep indentation. In this study, all BHN measurements stopped once the load reached to 20 lbf.

BHN is calculated by using the load-displacement curve:

$$\mathrm{BHN} = \frac{S}{\pi D_i} \tag{6.3}$$

where S is the slope of the linear part of the load-displacement curve during the loading stage. D_i is the diameter of the indenter (4 mm). The raw shale samples had an average BHN around 230±15 MPa, and the BHN values were also measured after reactions.

6.4 Results and Discussion

6.4.1 Microencapsulated Acids

6.4.1.1 Reactive Fractured Core Experiments

The unpropped fracture conductivity of the Eagle Ford shale samples were measured at 500 psi closure pressure before treatment. For the three different samples, they were equal to 0.19, 0.35 and 0.24 mdft. Table 6.5 shows the results of conductivity after the MEA treatments using acid concentrations of 0.5, 10 and 15 wt%. The final conductivities increased significantly in all the cases and were equal to 0.46, 1.18 and 9.94

mdft, respectively. A positive correlation was seen between percentage increment and the acid concentration used, as summarized in Table 6.5.

Table 6.5: Conductivity values of reactive fractured core experiments in MEA cases

Expt. #	1	2	3
Conductivity before MEA (mdft)	0.19	0.35	0.24
Conductivity after MEA (mdft)	0.46	1.18	9.94

Figure 6.5a shows the micrograph of one of the samples before MEA treatment. The surfaces were found to be free of any natural or induced (from saw-cutting) visible pores/vugs. A quantitative analysis using profilometer reveals the average surface roughness of 7.25 ± 1.52 μm. Although the acid treatment of shales results in mineral dissolution, it may have either beneficial or detrimental effect on the final conductivity. Since the conductivity is predominantly governed by the fracture aperture, factors such as the variation in etching patterns and non-uniform etching become highly relevant. Figure 6.5b shows the micrograph of fracture surface in Expt. 1 after treatment with MEA with an acid concentration of 0.5 wt%. The presence of acid-induced pores/vugs can be clearly seen on the surface. The average size (in the xy plane) of these vugs were 85.1 ± 28.4 μm. The average surface roughness (depth) was increased to 8.68 ± 4.82 μm (Table 6.6).

Table 6.6: Average and root mean squared roughness of Expt. 1 and 2

Label	Expt. #	Average Roughness, Ra in μm	RMS Roughness, Rrms in μm
a	**Before MEA**	7.25 ± 1.52	9.43 ± 2.47
b	**1**	8.68 ± 4.82	11.27 ± 6.33
c &d	**2**	16.77 ± 6.89	23.26 ± 8.54

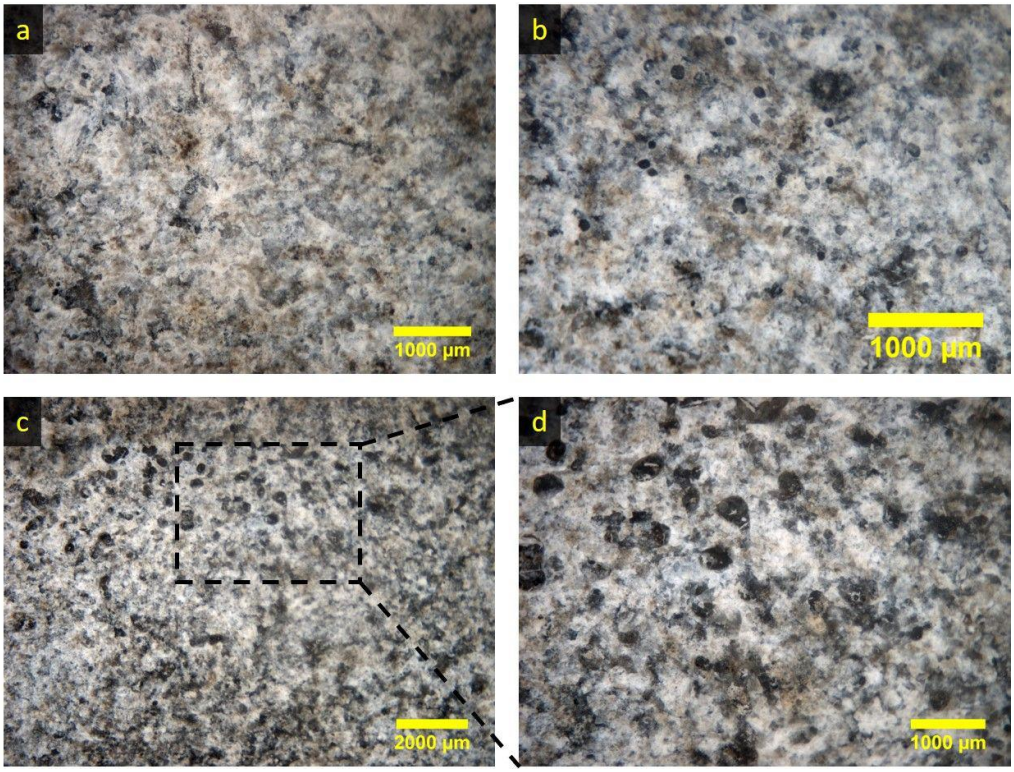

Figure 6.5: Optical micrograph of the fracture surface of shale (a) before MEA treatment; and post-MEA treatment with an acid concentration of (b) 0.5 wt%, (c) 10.0 wt%, (d) 10.0 wt% (zoomed image)

Figure 6.6 shows the 3D surface profile. Interestingly, these vugs were preferentially circular in shape. We hyphothesize that once the acid is released from the MEA, it results in the formation of beads of acids due to the presence of hydrophobic nanoparticles, which then create these specific circular etching patterns. Generally, the mineral distribution and the availability of acid could play a significant role in dictating these patterns. However, in the present cases, the shale was highly calcite-rich, and amount of acid used in the experiments was very limited. Figure 6.5c,d show the micrograph of the shale surface in Expt. 2 when the acid was 10 wt%. Note that amount of MEA used was kept constant in all cases. Analogous to the Expt. 1, the formation of circular vugs was observed on the surface. The average size of the vugs was 211.4 ± 82.1 µm. The average

surface roughness was measured to be 16.77 ± 6.89 µm indicating deeper etching due to higher concentration of acid. It is to be noted that in both Expt. 1 and 2, the surface profiles in the vicinity of the vugs were still smooth (Figure 6.6 b,c) indicating a non-uniform etching pattern due to MEA.

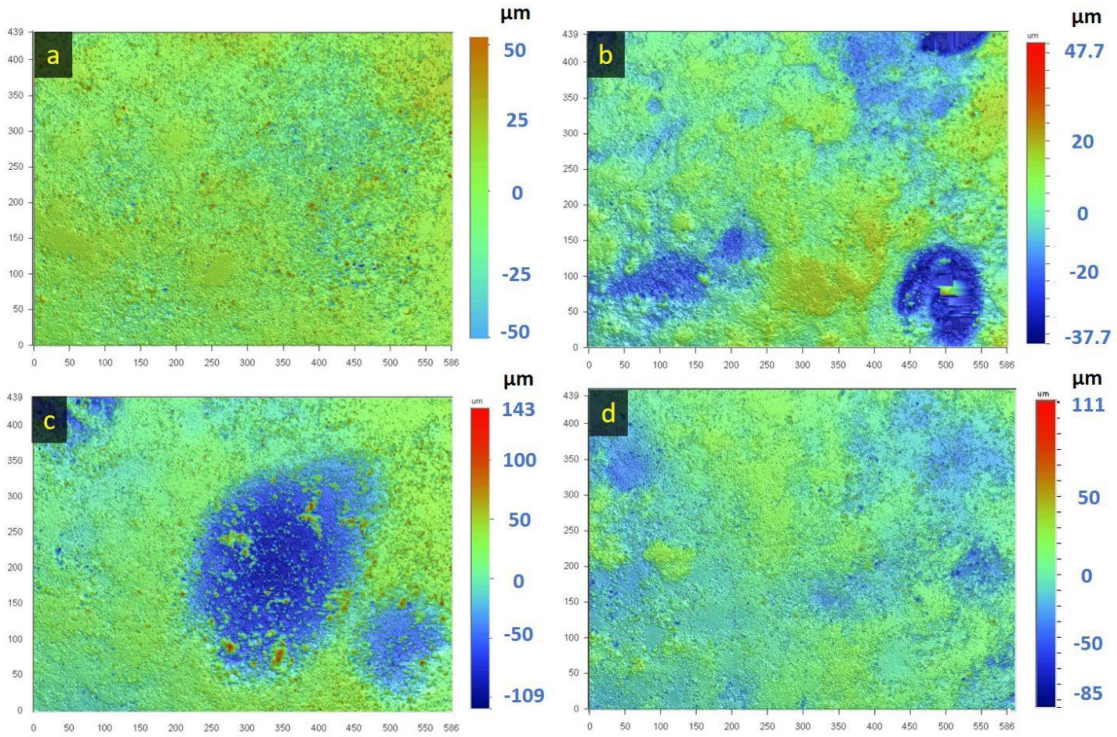

Figure 6.6: Surface topology of shale surface (a) before MEA treatment; and post-MEA treatment with an acid concentration of (b) 0.5 wt%, (c) 10.0 wt%, (d) surface topology inside the etched pattern obtained from 15 wt% acid.

In the last case, the acid concentration was increased 15 wt%. Figure 6.7 a shows the digital image of the entire shale sample after treatment. Distinct patches (black color) could be easily seen on the surface on different locations. These patches were of the order of several mm in dimensions as shown in Figure 6.7 a,b. These patches could not be imaged in a single scan using surface profilometer due to the limited scanning area capability of

the instrument. Figure 6.6d shows the surface profile inside one of the patches. Interestingly, the surface roughness inside the etched zone was relatively smooth. As observed in previous cases, small circular vugs were also seen at different locations of the surface (Figure 6.7c). The conductivity increment for Expt. 3 was significantly higer than that of Expt. 1 and 2. The rock was intact and its hardness was not compromised. The enhanced conductivity can be attributed to the formation of these non-localized surface etchings.

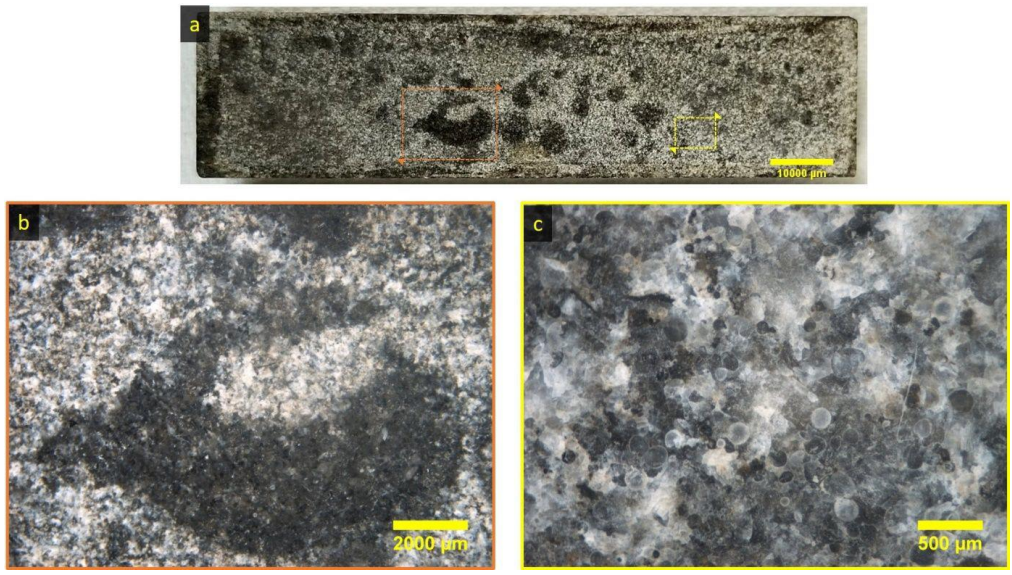

Figure 6.7: (a) Digital image of the entire shale fracture face post-MEA treatment of Expt. 3; (b,c) optical micrograph of different regions.

6.4.2 In-situ Proppant Generation

6.4.2.1 Low Salinity Brine Batch Reaction Experiments

Batch experiments were conducted to study the effect of chemical composition on the crystal formation on the surface of shales. Figures 6.8 shows the generation of crystals on a shale penny chip of 1 inch diameter. Figure 6.9 and 6.10 show SEM images of crystals

formed on the shale at different combinations of chemicals in 2500 ppm NaCl brine. The pictures on the left panel are low resolution pictures and those on the right are higher resolution pictures. The label ‘xHyD’ (in Figure 6.9 and 6.10) means that the shale sample was treated with x wt% of chemical H and y wt% of chemical D. In all these experiments, crystals were successfully generated within 24 hours.

Figure 6.8: Generation of crystals on shale surface.

For Figure 6.9a through c, only the acid was used and acid concentration was increased from Figure 6.9a to c. For Expt. 4 (the ‘1H0D’ case), there were a lot of cavities of size about 50 μm on the shale surface due to calcite dissolution. These cavities could enhance the flow capacity of the shale matrix and lead to better production. There were crystals of size 50 - 600 μm and only a few crystals were observed on the shale surface. The surface hardness of the shale was 230 MPa before any treatment. The post-treatment surface hardness was about 221 MPa, which indicated the absence of softening due to the chemical treatment. As the acid concentration (chemical H) increases, calcite dissolution increases. For Expt. 5 (the ‘2H0D’ case), more calcite was dissolved (compared to Expt. 4) to form cavities, and the number of HAp crystals increased (Figure 6.9b). Some of the cavities were filled with HAp crystals. However, excessive calcite dissolution resulted in a lower hardness value of 136 MPa and mud generation. The same features were observed

in Expt. 6 (the '3H0D' case) (Figure 6.8c). Higher acid use leads to more proppant formation, but also higher calcite dissolution and loss in hardness. That is why chemical D was introduced to control the calcite dissolution rate in the next set of experiments.

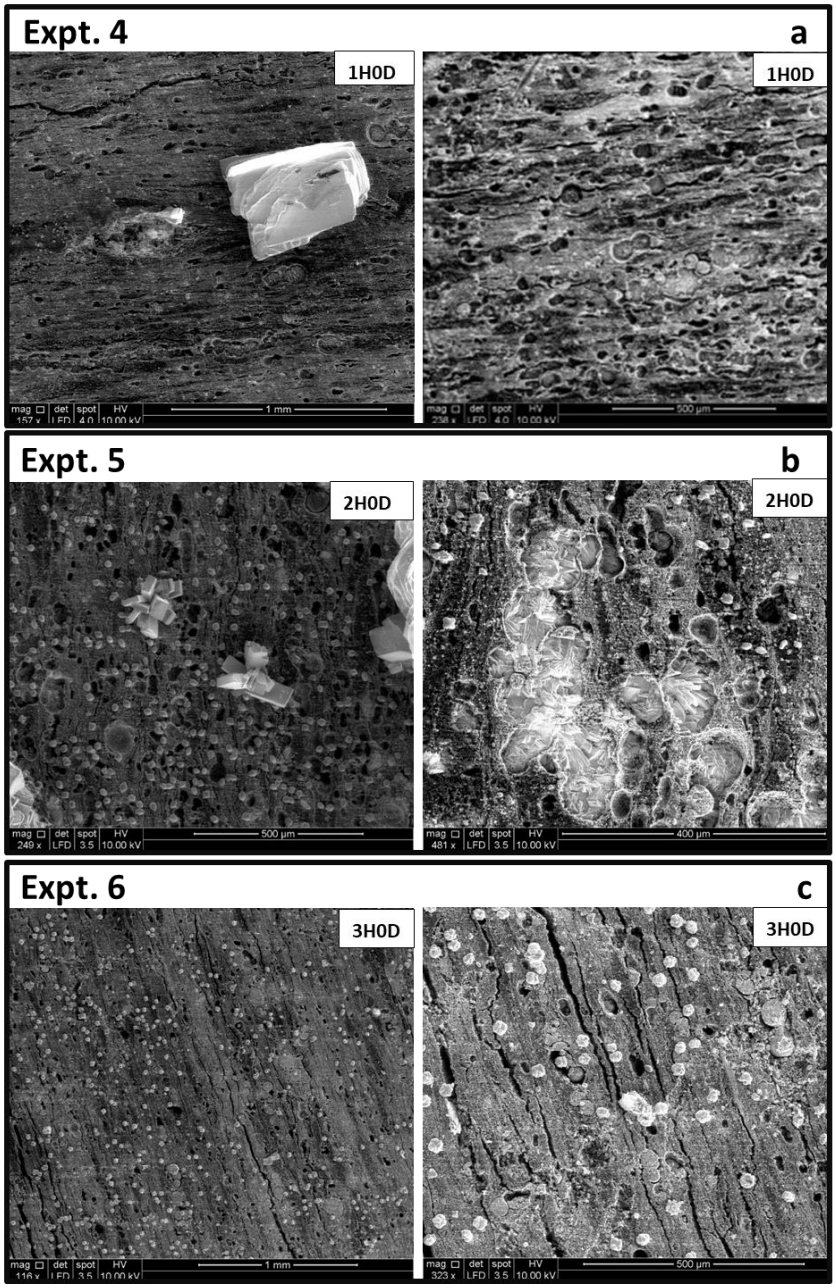

Figure 6.9: (a) SEM images of Expt. 4, (b) SEM images of Expt. 5, (c) SEM images of Expt. 6.

Figure 6.10a to c show representative SEM images of shale samples treated with both chemicals H and D. Crystals of size 200 μm (the size of common commercial sand proppants) formed on the surface of the shale sample, and plenty of cavities were also generated. The location of calcite largely determined the distribution of the crystals. In both Expt. 7 and 8 (cases '1H1D' and '2H1D'), the crystals were aligned along several lines which indicated that they possibly originated from calcite-rich layers. In Expt. 9 (the '3H1D' case), a calcite-rich layer was fully converted into a HAp layer. Moreover, for Expt. 9 and 12 at high concentrations (cases '3H1D' and '3H3D'), a larger coverage of the shale surface was observed due to excessive crystal formation. The formation of a HAp film on the shale surface might be unwarranted because it could potentially plug the pore spaces. Interestingly enough, for Expt. 9 (case '3H1D'), the post-treatment hardness decreased to 133 Mpa. A large ratio of chemical H to chemical D leads to a large number of crystal formation and weakening of the surface. In Expt. 7 and 10 (cases '1H1D' and '2H2D'), plenty of crystals were generated and the post hardness was high (272 MPa and 277 MPa, respectively). These chemical combinations are favorable. The hardness value for Experiments 4 – 12 in low salinity brine were summarized in Table 6.7.

Table 6.7: Hardness value for Experiments 4 – 12 in low salinity brine.

H wt%	D wt%			
	0	1	2	3
0	230	NA	NA	NA
1	221	272	NA	NA
2	136	146	277	NA
3	148	133	223	284

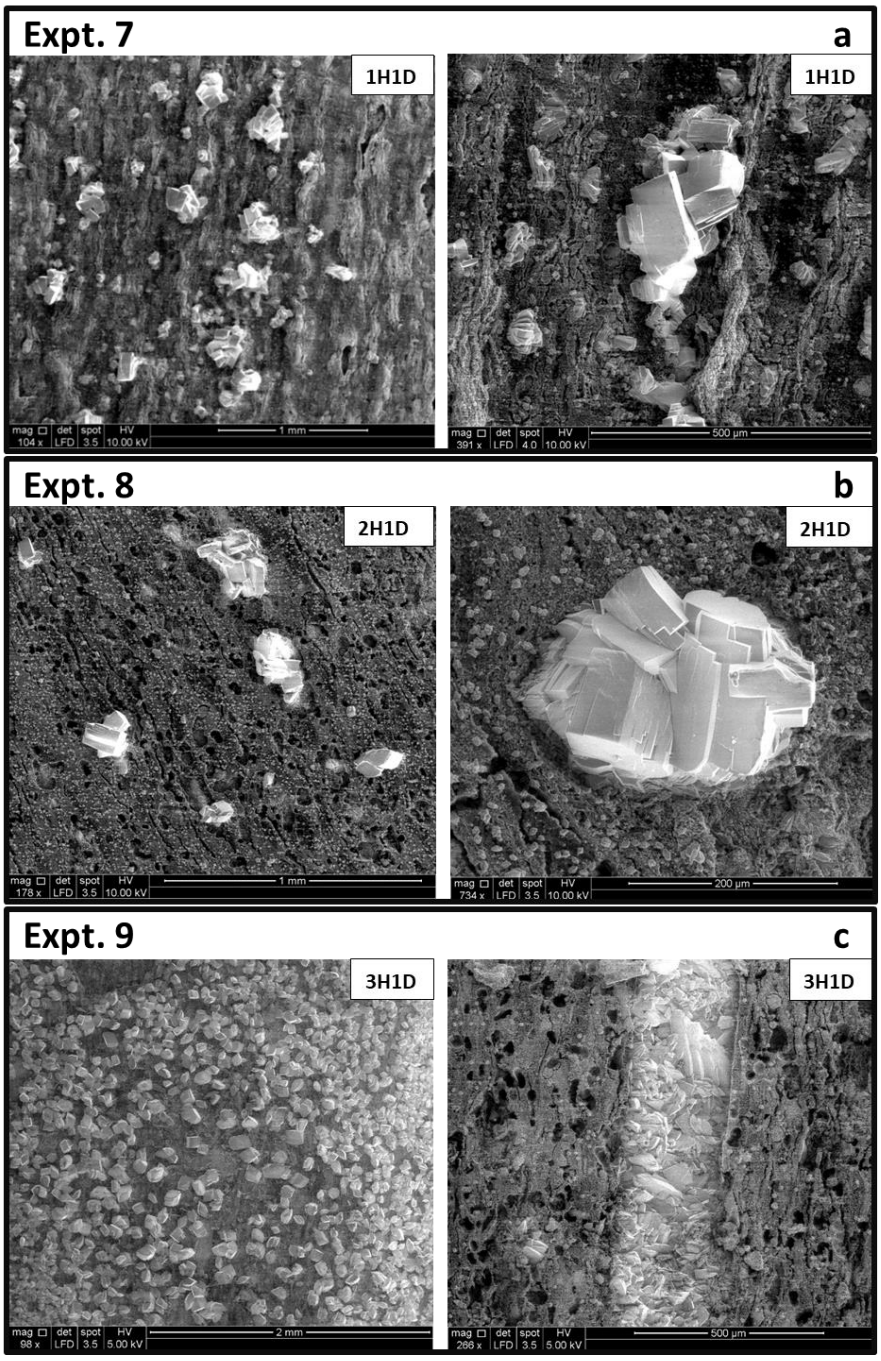

Figure 6.10: (a) SEM images of Expt. 7, (b) SEM images of Expt. 8, (c) SEM images of Expt. 9.

6.4.2.2 High Salinity Brine Batch Reaction Experiments

Batch reaction experiments were carried out with a typical high salinity brine (referred as seawater), and Figure 6.11 shows the representative SEM images of shale surfaces after treatment at different chemical concentrations in seawater (SW). Crystals forming in seawater brine were more spherical in shape compared to those forming in low salinity brine. In the high salinity and hardness brine, more crystals formed compared to the corresponding low salinity brine cases. Additionally, the crystals formed along calcite-rich layers.

For Expt. 4 and 8 in seawater (case '1H0D' and '2H1D'), lots of spherical crystals and cavities were generated on the shale surface. The post shale surface hardness of these two cases was about 197 MPa and 160 MPa, respectively. For Expt. 7 and 10 (case '1H1D' and '2H2D'), the surface of the crystals looked smoother and the shale surface contained less cavities. As the D component increases, the number of cavities decreases. The hardness value for Experiments 4 – 12 in high salinity brine were summarized in Table 6.8.

Table 6.8: Hardness value for Experiments 4 – 12 in high salinity brine.

H wt%	D wt%			
	0	1	2	3
0	230	NA	NA	NA
1	197	208	NA	NA
2	167	160	284	NA
3	132	161	214	281

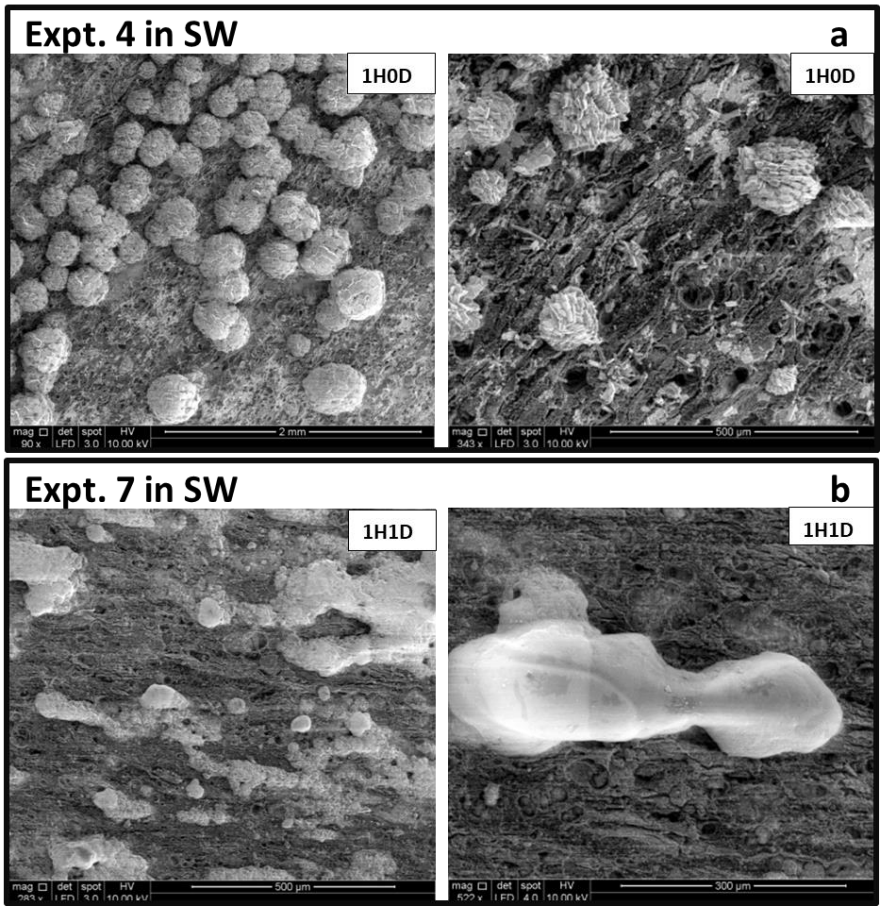

Figure 6.11: (a) SEM images of Expt. 4 in SW, (b) SEM images of Expt. 7 in SW, (c) SEM images of Expt. 8 in SW, (d) SEM images of Expt. 10 in SW

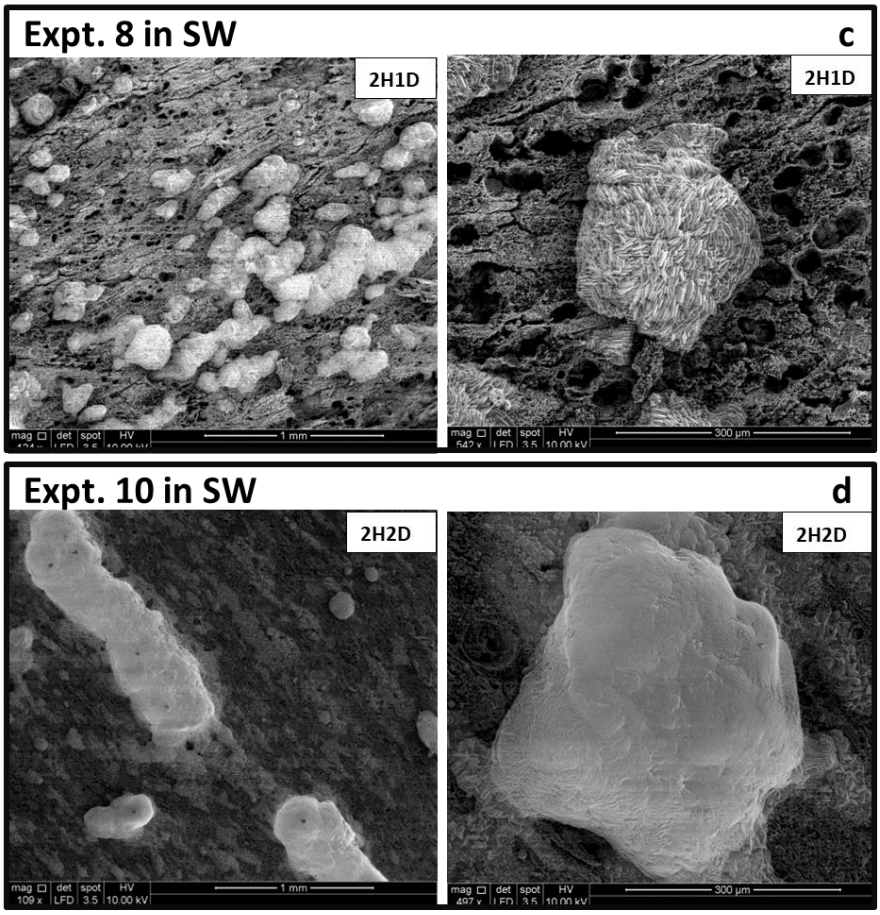

Figure 6.11: Continued

6.4.2.3 Reactive Fractured Core Experiments

Five reactive flow experiments were conducted in fractured cores. Experiments 13 – 15 were in reservoir shale rocks, and they were cut into half in our lab. Due to the rough cutting surface, initial brine conductivity for experiments 13 and 14 were not very low. For Experiment 15, we polished the fractured surface after cutting, and managed to lower the initial brine conductivity to around 3 md-ft. Additionally, we used split outcrop samples from vendors, which offered typical initial brine conductivity less than 0.5 md-ft, in Experiments 16, 17 and 18.

Experiment 13 was designed to evaluate the feasibility of using synthesized crystals to support fracture aperture. It is not a reactive flow experiment. Brine conductivity of the unpropped fracture core was measured at 1000 psi overburden pressure, and the value was 71 md-ft. Crystals formed from batch experiments were manually introduced onto the fracture surface, as shown in Figure 6.12. Heat shrink tubes were used to hold the core assembly and then it was placed in a core holder. The brine conductivity was measured again at 1000 psi overburden pressure. The brine conductivity increased to 483 md-ft with the crystals in the fracture, an almost 7 times increase. Figure 6.13a shows a Micro-CT image of the core assembly. Figure 6.13b shows the view into the fracture in the direction of the blue arrow, and it shows that the crystals could maintain a 330 μm aperture. Figure 6.13c shows the view into the fracture in the direction of the red arrow. The presence of crystals leads to the large increase in post fracture conductivity.

Figure 6.12: Crystals were manually introduced onto the fracture surface

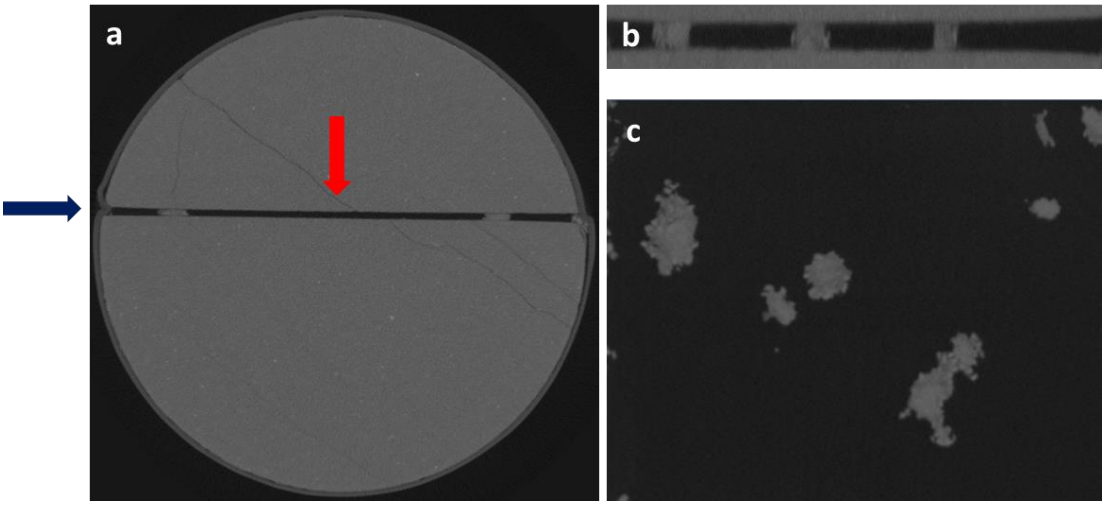

Figure 6.13: Micro-CT images of the propped core in Experiment 13

In Experiment 14, the reactive flow experiment was conducted as described in section 6.3.3.3, and it mimicked the condition in a narrow microfracture geometry. Initial brine conductivity of the unpropped fractured core was measured at 1000 psi overburden pressure, and the value was 18 md-ft. After the treatment, a lot of small crystals formed on the surface of the rock, as shown in Figure 6.14. The brine conductivity of the unpropped core was measured after removing the rubber cubes. The post conductivity increased to 21 md-ft, which led to a 16.6% increase in fracture conductivity.

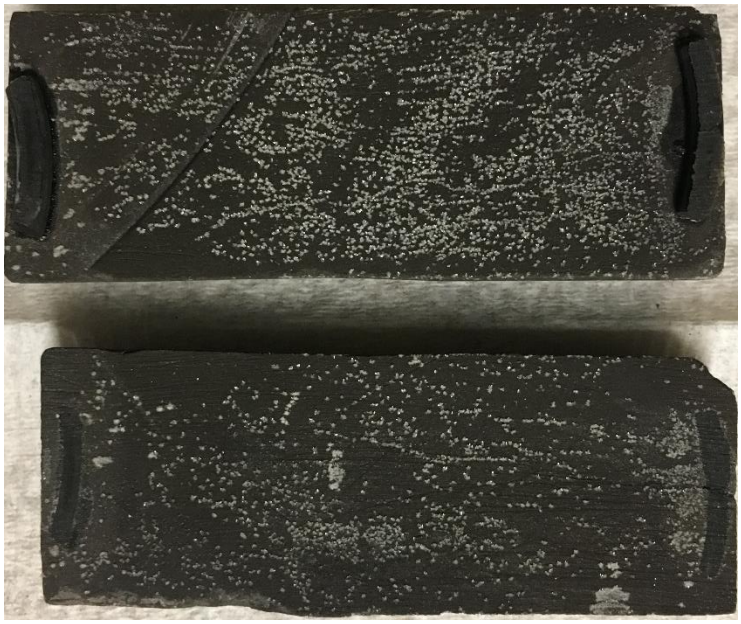

Figure 6.14: Fracture surface of Experiment 14 after reaction

Figure 6.15a shows a Micro-CT image of the core assembly. Figure 6.15b shows the view if looking into the fracture in the direction of the navy arrow, and it shows that the crystals could maintain a 254 μm aperture. Figure 6.15c shows the view if looking into the fracture in the direction of the red arrow. Due to the limited volume of solution exposed to the fracture surface, the size of the crystals was smaller compared to those generated in batch tests, and due to the roughness of the initial fracture, a small increase in fracture conductivity was observed. In Experiments 13 and 14, the initial unpropped fracture conductivity were high because of poor cutting quality in our lab saw, and this could potentially mask the contribution of these small crystals formed in between the narrow fracture.

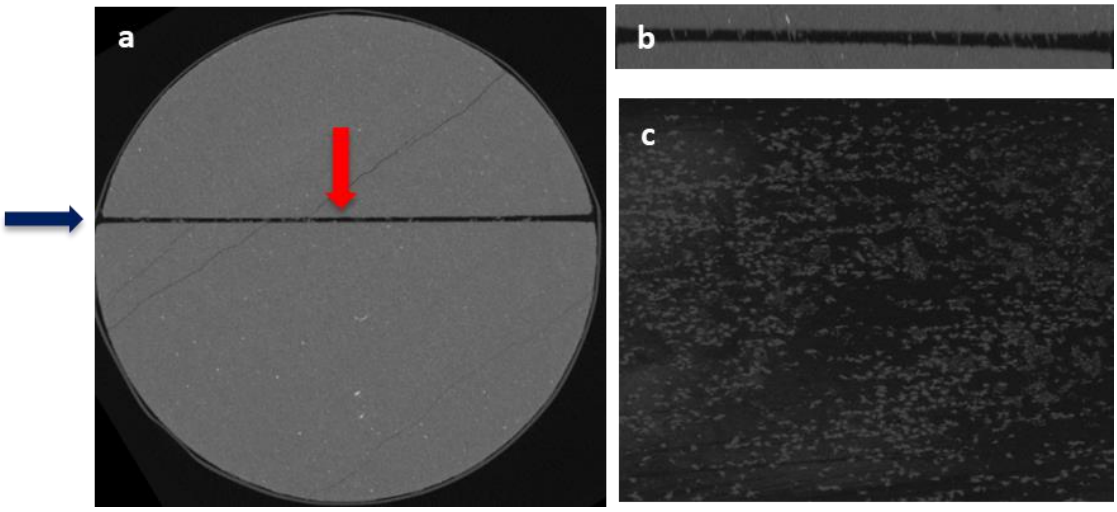

Figure 6.15: A slice of micro-CT images of Experiment 14

In order to achieve more realistic initial unpropped fracture conductivity, Experiments 15 - 18 were performed. These three cases were all conducted with the same procedure as that of Experiment 14. The summary of initial and post brine conductivities at the unpropped condition are listed in Table 6.8. The shale sample used in Experiment 15 was a reservoir core and the fractured surface was polished after splitting in our lab. The initial brine conductivity of the unpropped fracture was 3.4 md-ft. After the chemical treatment, the fracture conductivity at unpropped condition increased to 37.0 md-ft. The shale samples used in Experiments 16, 17 and 18 were received from vendors. These cores were cut into half by the vendor, and the initial brine conductivity was 0.25, 0.47 and 0.30 md-ft for Experiments 16, 17 and 18, respectively. After the treatment, the fracture conductivity increased to 0.74, 3.39 and 1.79 md-ft, respectively. The increase is 3 to 10 times due to the in situ proppant formation.

Table 6.9: Conductivity increase in reactive flow experiments

Shale Type	Reservoir	Reservoir	Reservoir	Outcrop	Outcrop	Outcrop
Expt. #	13	14	15	16	17	18
Initial Conductivity (md-ft)	71	18	3.4	0.25	0.47	0.30
Post Conductivity (md-ft)	483	21	37	0.74	3.39	1.79

There is also a concern that the acid H could be consumed in the near wellbore region, leaving little acid for the downstream microfractures. However, the lowest PKa value of acid H is around 2.16, which means the reaction rate could be much slower compared to that of HCL. In addition, if the acid gets consumed in the near well bore region, encapsulated chemical systems could be developed for deep delivery of these chemicals.

6.5 CONCLUSIONS

Two chemical stimulation techniques have been proposed for calcite-rich shales to improve fracture conductivity. The following conclusions can be drawn:

1. A practical route to microencapsulation of acid is possible by blending of concentrated acids with highly hydrophobic silica nanoparticles which results in self-assembly of particles at the water-air interface. The release of acid could be triggered via mechanical crushing during fracture closures.
2. The unpropped fracture conductivity of the calcite-rich shale increased dramatically after the MEA treatment. The released acids from MEA resulted in the formation of non-uniformly distributed vugs on the fracture surface of varying size (um to mm) depending on the MEA distribution and acid concentration.

3. The hydro-thermal reaction is able to form proppant-sized crystals on the calcite-rich shale surfaces at elevated salinity, hardness and temperature conditions within 24 hours.
4. The distribution of calcite affects the formation of the crystals, and the crystals generally tend to form in calcite-rich regions.
5. Proper design of the chemical formulation can lead to high hardness crystal generation and avoid shale softening.
6. The hydro-thermal reaction is able to improve fracture conductivity in microfractures, and a typical 3 – 10 times increase in post fracture conductivity is observed in reactive fractured core experiments.

Chapter 7: Conclusions and Recommendations

7.1 CONCLUSIONS

During the hydraulic fracturing process, a lot of complex fracture networks and fractured surface are created in shale reservoirs. A good utilization of fractured surface is crucial for shale well productivity, and this dissertation presents an experimental and numerical study to improve effective fracture surface. Proppants are injected during hydraulic fracturing to keep the fractures open. Proppant transport in complex fracture networks is poorly understood, and this study started from investigating proppant transport in a fracture with intersections. Some quantitative data were retrieved from the lab results and an experimentally validated CFD model was also proposed. Besides proppant transport between fractures, fracturing fluid also plays a significant role in proppant placement. Foam is a promising fracturing fluid, and its drainage process and proppant settling in it have been studied and incorporated in an in-house fracturing modeling to evaluate proppant placement in field scale for the first time. Additionally, two chemical stimulation techniques were proposed to target on narrow fractures that cannot accommodate any proppants. The first technique is a nanoparticle encapsulated acid system, and the second one is a hydrothermal reaction which is able to generate in-situ mineral crystals acting as proppants on fractured shale surfaces. Improved fracture conductivity were observed experimentally for both techniques. The main conclusions obtained from this dissertation are listed as follows.

- The existence of fracture intersections would affect the placement of proppants. According to lab results, the formation of a proppant bed at the fracture junction could significantly alter the final proppant distribution. Generally, a linear relationship is

observed between the proppant injected and the fraction of proppant that flows into bypass secondary fractures.

- Injection rate, proppant size and the orientation of bypass fracture could affect the placement of proppant in secondary fractures. Considering the small scale of the lab experiments, bed-load transport could be the main mechanism governing the movement of the slurry. Under this condition: higher injection rate leads to better placement of proppant in secondary fractures; smaller bypass angle leads to slightly better placement of proppant in secondary fractures; proppant size does not have an apparent effect.
- Foam is not a single-phase fluid, and its gas fraction would vary vertically due to foam drainage process. In wet foams (70% nominal gas fraction), proppant could settle quickly and form a proppant bed due to strong foam drainage process. In dry foams (80% nominal gas fraction), drainage is limited and proppant could be uniformly suspended. However, vertical gas fraction variation still exists in dry foams, which could lead to a faster moving and settling proppant at the bottom of the fracture.
- The microstructure of foam, such as foam bubbles and lamella, could mechanically trap proppants from settling. Therefore, applying foam effective viscosity to calculate proppant settling velocity in foam would be misleading. Besides, this mechanical entrapment of proppants also leads to complex flow patterns such as protrusion of foam fingers into proppant laden foam.
- A hybrid Eulerian-Lagrangian Computational Fluid Dynamics (CFD) model is established to simulate proppant transport in fractures with intersections. This model not only honors the discrete nature of proppants, but also saves computational time by modeling particle-particle interactions with the Kinetic Theory of Granular Flow (KTGF).

- The CFD model successfully matched both qualitative and quantitative results in Chapter 2. The values of bypass/total ratio, proppant bed shape, proppant residence time and the formation of vortex at fracture intersections are all matched with the model.
- Proppant settling in foam was found to depend on foam quality and foam velocity gradient; a settling velocity correlation was developed based on the results from Chapter 3. In this new correlation, proppants settle slower as the foam quality increases or the velocity gradient term decreases. In addition, a foam drainage model was developed by introducing a shape scaling function. This model matched several key characteristics of foam drainage: a linear evolution regime, a final exponential equilibrium regime and the accumulation of a liquid table at the bottom.
- The two modules were incorporated into an in-house fracturing model to evaluate proppant placement in field-scale foam-fracturing application. The simulation results indicate that the drainage effect is more important than the settling velocity in terms of final proppant placement. Generally, a slowly draining foam could lead to a more uniform placement of proppants.
- Nanoparticle encapsulated acids are effective on improving fracture conductivity. Microstructures such as vugs and local surface etching patterns were developed after acid release during fracture closure. Significant improvement of fracture conductivity (~ 40x) could be achieved in case the surface etching is very uneven.
- A hydro-thermal reaction was proposed to form mineral crystals on shale surface to act as in-situ proppant. These crystals could grow as big as common proppants, and the distribution of the crystals were largely determined by the distribution of the calcite-rich regions. The rock hardness could be maintained if the solution was designed

properly, and fracture conductivity could improve 3 – 10 times after reaction according to lab results.

7.2 RECOMMENDATIONS

Based on the experience and results obtained from this work, the following future work is recommended.

- In this work, the CFD simulation was conducted in a static fracture geometry with time-independent boundary conditions. In reality, proppants would transport in a propagating fracture, and it would be great if the model could be coupled with a fracture propagation model. With such capabilities, the proppant placement in a fracture network could be better understood.
- The conservation equation of granular temperature, Eq. (4.23), is only solved in its algebraic form by neglecting the convection and diffusion term. However, due to the improving power of HPF platforms, these two terms could be included in the original equation to handle fast and diluted conditions.
- The visualization experiments of proppant settling in dynamic foam was performed at ambient conditions. However, temperature and pressure could significantly alter the behavior of foam. Therefore, it is recommended to conduct similar experiments at HPHT condition. Such experiments could bring significant guidance to foam fracturing applications.
- The drainage model could be improved by developing an empirical index term. The term could be determined based on lab results of foam drainage experiments to give a more reasonable drainage profile of foam. In addition, the in-house fracturing model is fairly simple, and a more comprehensive real 3D fracturing model should be used to simulate foam fracturing in field scale.

- The MEA powders should be injected into the fracture instead of being manually placed in the fracture. Manual placement leads to uniform powder exposure to the fracture surface, and a more uneven distribution of powders would be achieved by injecting the powders into the fracture. In addition, such an experiment could also demonstrate the injectability of the MEA system.
- More systematic studies of the hydro-thermal reaction should be conducted to further understand the successful factors for this application. Such studies could include the following. 1. Investigate the mechanism of the nucleation process to figure out how to generate isolated and big crystals instead of small and continuous crystals. 2. Conduct experiments in proppant-filled fracture cores to evaluate the effect of crystals on the conductivity of proppant-filled fracture. 3. Perform long-term fracture conductivity measurement as the fracture conductivity would change over time. 4. Increase the overburden pressure to reservoir condition.

References

Alotaibi, M.A., Miskimins, J.L., 2018. Slickwater Proppant Transport in Hydraulic Fractures: New Experimental Findings and Scalable Correlation. SPE Production & Operations 33, 164–178. https://doi.org/10.2118/174828-PA

Alzobaidi, S., Lotfollahi, M., Kim, I., Johnston, K.P., DiCarlo, D.A., 2017. Carbon Dioxide-in-Brine Foams at High Temperatures and Extreme Salinities Stabilized with Silica Nanoparticles. Energy Fuels 31, 10680–10690. https://doi.org/10.1021/acs.energyfuels.7b01814

Andrews, M.J., O'Rourke, P.J., 1996. The multiphase particle-in-cell (MP-PIC) method for dense particulate flows. International Journal of Multiphase Flow 22, 379–402. https://doi.org/10.1016/0301-9322(95)00072-0

Andrianov, A., Farajzadeh, R., Mahmoodi Nick, M., Talanana, M., Zitha, P.L.J., 2012. Immiscible Foam for Enhancing Oil Recovery: Bulk and Porous Media Experiments. Ind. Eng. Chem. Res. 51, 2214–2226. https://doi.org/10.1021/ie201872v

Armstrong, L.M., Luo, K.H., Gu, S., 2010. Two-dimensional and three-dimensional computational studies of hydrodynamics in the transition from bubbling to circulating fluidised bed. Chemical Engineering Journal 160, 239–248. https://doi.org/10.1016/j.cej.2010.02.032

ASTM E10-15a, n.d. Test Method for Brinell Hardness of Metallic Materials. ASTM International. https://doi.org/10.1520/E0010-15

Barati, R., Liang, J.-T., 2014. A review of fracturing fluid systems used for hydraulic fracturing of oil and gas wells. Journal of Applied Polymer Science 131.

Bhakta, A., Ruckenstein, E., 1997. Decay of standing foams: drainage, coalescence and collapse. Advances in Colloid and Interface Science 70, 1–124. https://doi.org/10.1016/S0001-8686(97)00031-6

Binks, B.P., Murakami, R., 2006. Phase inversion of particle-stabilized materials from foams to dry water. Nature Materials 5, 865–869. https://doi.org/10.1038/nmat1757

Biot, M.A., Masse, L., Medlin, W.L., 1986. A Two-Dimensional Theory of Fracture Propagation. SPE Production Engineering 1, 17–30. https://doi.org/10.2118/11067-PA

Blot, M.A., Medlin, W.L., 1985. Theory of Sand Transport in Thin Fluids. Presented at the SPE Annual Technical Conference and Exhibition, Society of Petroleum Engineers. https://doi.org/10.2118/14468-MS

Blyton, C.A.J., Gala, D.P., Sharma, M.M., 2015. A Comprehensive Study of Proppant Transport in a Hydraulic Fracture. Presented at the SPE Annual Technical Conference and Exhibition, Society of Petroleum Engineers. https://doi.org/10.2118/174973-MS

Bokane, A., Jain, S., Deshpande, Y., Crespo, F., 2013. Computational Fluid Dynamics (CFD) Study and Investigation of Proppant Transport and Distribution in Multistage Fractured Horizontal Wells. Presented at the SPE Reservoir Characterization and Simulation Conference and Exhibition, Society of Petroleum Engineers. https://doi.org/10.2118/165952-MS

Brouwers, H.J.H., 2010. Viscosity of a concentrated suspension of rigid monosized particles. Phys. Rev. E 81, 051402. https://doi.org/10.1103/PhysRevE.81.051402

Cairns, A.J., Al-Muntasheri, G.A., Sayed, M., Fu, L., Giannelis, E.P., 2016. Targeting Enhanced Production through Deep Carbonate Stimulation: Stabilized Acid Emulsions, in: SPE International Conference and Exhibition on Formation Damage Control. Society of Petroleum Engineers. https://doi.org/10.2118/178967-MS

Cantat, I., Pitois, O., 2006. Stokes experiment in a liquid foam. Physics of Fluids 18, 083302. https://doi.org/10.1063/1.2267062

Carter, B., M. Weaver, J.V., Wang, W., G. Spiller, D., J. Adams, D., I. Cooper, A., 2011. Microencapsulation using an oil-in-water-in-air 'dry water emulsion.' Chemical Communications 47, 8253–8255. https://doi.org/10.1039/C1CC12698A

Chang, F.F., Berger, P.D., Lee, C.H., 2015. In-Situ Formation of Proppant and Highly Permeable Blocks for Hydraulic Fracturing. Presented at the SPE Hydraulic Fracturing Technology Conference, Society of Petroleum Engineers. https://doi.org/10.2118/173328-MS

Chapman, S., Cowling, T.G., Burnett, D., 1990. The Mathematical Theory of Non-uniform Gases: An Account of the Kinetic Theory of Viscosity, Thermal Conduction and Diffusion in Gases. Cambridge University Press.

Cloete, S., Johansen, S.T., Amini, S., 2012. Performance evaluation of a complete Lagrangian KTGF approach for dilute granular flow modelling. Powder Technology 226, 43–52. https://doi.org/10.1016/j.powtec.2012.04.010

Daccord, G., Touboul, E., Lenormand, R., 1989. Carbonate Acidizing: Toward a Quantitative Model of the Wormholing Phenomenon. SPE Production Engineering 4, 63–68. https://doi.org/10.2118/16887-PA

Ding, J., Gidaspow, D., 1990. A bubbling fluidization model using kinetic theory of granular flow. AIChE J. 36, 523–538. https://doi.org/10.1002/aic.690360404

Dontsov, E.V., Peirce, A.P., 2015. Proppant transport in hydraulic fracturing: Crack tip screen-out in KGD and P3D models. International Journal of Solids and Structures 63, 206–218. https://doi.org/10.1016/j.ijsolstr.2015.02.051

Enzendorfer, C., Harris, R.A., Valko, P., Economides, M.J., Fokker, P.A., Davies, D.D., 1995. Pipe viscometry of foams. Journal of Rheology 39, 345–358.

Faroughi, S.A., Pruvot, A.J.-C.J., McAndrew, J., 2018. The rheological behavior of energized fluids and foams with application to hydraulic fracturing: Review. Journal of Petroleum Science and Engineering 163, 243–263. https://doi.org/10.1016/j.petrol.2017.12.051

Fei, Y., Pokalai, K., Johnson, R., Gonzalez, M., Haghighi, M., 2017. Experimental and simulation study of foam stability and the effects on hydraulic fracture proppant placement. Journal of Natural Gas Science and Engineering 46, 544–554. https://doi.org/10.1016/j.jngse.2017.08.020

Forny, L., Pezron, I., Saleh, K., Guigon, P., Komunjer, L., 2007. Storing water in powder form by self-assembling hydrophobic silica nanoparticles. Powder Technology 171, 15–24. https://doi.org/10.1016/j.powtec.2006.09.006

Friedmann, F., Jensen, J.A., 1986. Some Parameters Influencing the Formation and Propagation of Foams in Porous Media. Presented at the SPE California Regional Meeting, Society of Petroleum Engineers. https://doi.org/10.2118/15087-MS

Fu, P., Johnson, S.M., Carrigan, C.R., 2012. An explicitly coupled hydro-geomechanical model for simulating hydraulic fracturing in arbitrary discrete fracture networks. International Journal for Numerical and Analytical Methods in Geomechanics 37, 2278–2300. https://doi.org/10.1002/nag.2135

Gale, J.F., Laubach, S.E., Olson, J.E., Eichhubl, P., Fall, A., 2014. Natural fractures in shale: A review and new observations. AAPG bulletin 98, 2165–2216.

Gale, J.F.W., Reed, R.M., Holder, J., 2007. Natural fractures in the Barnett Shale and their importance for hydraulic fracture treatments. AAPG Bulletin 91, 603–622. https://doi.org/10.1306/11010606061

Gaurav, A., Dao, E.K., Mohanty, K.K., 2012. Evaluation of ultra-light-weight proppants for shale fracturing. Journal of Petroleum Science and Engineering 92–93, 82–88. https://doi.org/10.1016/j.petrol.2012.06.010

Gomaa, A.M., Hudson, H., Nelson, S., Brannon, H., 2016. Improving Fracture Conductivity by Developing and Optimizing Channels within the Fracture Geometry: CFD Study, in: SPE International Conference and Exhibition on Formation Damage Control. 24-26 Feb, Lafayette, Louisiana, USA, SPE-178982. https://doi.org/10.2118/178982-MS

Gu, M., Dao, E., Mohanty, K.K., 2015. Investigation of ultra-light weight proppant application in shale fracturing. Fuel 150, 191–201. https://doi.org/10.1016/j.fuel.2015.02.019

Gu, M., Mohanty, K.K., 2015. Rheology of polymer-free foam fracturing fluids. Journal of Petroleum Science and Engineering 134, 87–96. https://doi.org/10.1016/j.petrol.2015.07.018

Gu, M., Mohanty, K.K., 2014. Effect of foam quality on effectiveness of hydraulic fracturing in shales. International Journal of Rock Mechanics and Mining Sciences 70, 273–285.

Harris, P.C., 1995. A Comparison of Mixed Gas Foams With N2 and C02 Foam Fracturing Fluids on a Flow Loop Viscometer. SPE Production & Facilities 10, 197–203. https://doi.org/10.2118/20642-PA

Harris, P.C., 1989. Effects of Texture on Rheology of Foam Fracturing Fluids. SPE Production Engineering 4, 249–257. https://doi.org/10.2118/14257-PA

Harris, P.C., Reidenbach, V.G., 1987. High-Temperature Rheological Study of Foam Fracturing Fluids. Journal of Petroleum Technology 39, 613–619. https://doi.org/10.2118/13177-PA

Holt, T., Vassenden, F., Svorstol, I., 1996. Effects of Pressure on Foam Stability; Implications for Foam Screening. Presented at the SPE/DOE Improved Oil Recovery Symposium, Society of Petroleum Engineers. https://doi.org/10.2118/35398-MS

Hutzler, S., Verbist, G., Weaire, D., Steen, J.A. van der, 1995. Measurement of Foam Density Profiles Using AC capacitance. EPL 31, 497. https://doi.org/10.1209/0295-5075/31/8/013

Jing, Z., Feng, C., Wang, S., Xu, D., 2018. Origin of accelerated and hindered sedimentation of two particles in wet foam. Eur. Phys. J. E 41, 33. https://doi.org/10.1140/epje/i2018-11642-7

Jing, Z., Wang, S., Wang, Z., 2016. Detailed Structural and Mechanical Response of Wet Foam to the Settling Particle. Langmuir 32, 2419–2427. https://doi.org/10.1021/acs.langmuir.6b00281

Johnson, P.C., Jackson, R., 1987. Frictional–collisional constitutive relations for granular materials, with application to plane shearing. Journal of Fluid Mechanics 176, 67–93. https://doi.org/10.1017/S0022112087000570

Kadhim, D., Imqam, A., Dunn-Norman, S., 2017. Ceramic Proppant Transport and Placement in Heterogeneous Fracture Systems, in: SPE/AAPG/SEG Unconventional Resources Technology Conference, 24-26 July, Austin, Texas, URTEC-2697613-MS; 2017.

Kern, L.R., Perkins, T.K., Wyant, R.E., 1959. The Mechanics of Sand Movement in Fracturing. Journal of Petroleum Technology 11, 55–57. https://doi.org/10.2118/1108-G

Koehler, S.A., Hilgenfeldt, S., Stone, H.A., 2000. A Generalized View of Foam Drainage: Experiment and Theory. Langmuir 16, 6327–6341. https://doi.org/10.1021/la9913147

Koehler, S.A., Hilgenfeldt, S., Stone, H.A., 1999. Liquid Flow through Aqueous Foams: The Node-Dominated Foam Drainage Equation. Physical Review Letters 82, 4232–4235. https://doi.org/10.1103/PhysRevLett.82.4232

Kong, X., McAndrew, J., Cisternas, P., 2016. CFD Study of Using Foam Fracturing Fluid for Proppant Transport in Hydraulic Fractures, in: Abu Dhabi International Petroleum Exhibition & Conference, 7 - 10 Nov, Abu Dhabi, UAE, SPE-183549-MS; 2016. Society of Petroleum Engineers.

Kou, R., Moridis, G.J., Blasingame, T.A., 2018. Analysis and Modeling of Proppant Transport in Inclined Hydraulic Fractures, in: SPE Hydraulic Fracturing Technology Conference and Exhibition. Society of Petroleum Engineers, 23 - 25 Jan, The Woodlands, Texas, USA, SPE-189856-MS; 2018. https://doi.org/10.2118/189856-MS

Kovscek, A.R., Radke, C.J., 1994. Fundamentals of Foam Transport in Porous Media, in: Foams: Fundamentals and Applications in the Petroleum Industry, Advances in Chemistry. American Chemical Society, pp. 115–163. https://doi.org/10.1021/ba-1994-0242.ch003

Li, N., Li, J., Zhao, L., Luo, Z., Liu, P., Guo, Y., 2017. Laboratory Testing on Proppant Transport in Complex-Fracture Systems. SPE Production & Operations 32, 382–391. https://doi.org/10.2118/181822-PA

Liang, Y., Zhang, Y., Li, T., Lu, C., 2014. A critical validation study on CPFD model in simulating gas–solid bubbling fluidized beds. Powder Technology 263, 121–134. https://doi.org/10.1016/j.powtec.2014.05.003

Liu, Y., Sharma, M.M., 2005. Effect of Fracture Width and Fluid Rheology on Proppant Settling and Retardation: An Experimental Study, in: SPE Annual Technical Conference and Exhibition, 9-12 Oct, Dallas, Texas, USA, SPE-96208-MS; 2005. https://doi.org/10.2118/96208-MS

Lu, L., Gopalan, B., Benyahia, S., 2017. Assessment of Different Discrete Particle Methods Ability To Predict Gas-Particle Flow in a Small-Scale Fluidized Bed. Industrial & Engineering Chemistry Research 56, 7865–7876. https://doi.org/10.1021/acs.iecr.7b01862

Lu, Y., Agrawal, M., 2014. A Computational-Fluid-Dynamics-Based Eulerian-Granular Approach for Characterization of Sand Erosion in Multiphase-Flow Systems. SPE Journal 19, 586–597. https://doi.org/10.2118/159921-PA

Lun, C.K.K., Savage, S.B., Jeffrey, D.J., Chepurniy, N., 1984. Kinetic theories for granular flow: inelastic particles in Couette flow and slightly inelastic particles in a general flowfield. Journal of Fluid Mechanics 140, 223–256. https://doi.org/10.1017/S0022112084000586

Mack, M., Sun, J., Khadilkar, C., 2014. Quantifying Proppant Transport in Thin Fluids: Theory and Experiments. Presented at the SPE Hydraulic Fracturing Technology Conference, Society of Petroleum Engineers. https://doi.org/10.2118/168637-MS

Malhotra, S., Lehman, E.R., Sharma, M.M., 2014. Proppant Placement Using Alternate-Slug Fracturing. SPE Journal 19, 974–985. https://doi.org/10.2118/163851-PA

Malhotra, S., Sharma, M.M., 2012. Settling of spherical particles in unbounded and confined surfactant-based shear thinning viscoelastic fluids: An experimental study. Chemical Engineering Science 84, 646–655. https://doi.org/10.1016/j.ces.2012.09.010

McAndrew, J., Cisternas, P., Pruvot, A., Kong, X., Tong, S., 2017. Water Consumption and Proppant Transport Aspects of Foam Fracturing Fluids, in: SPE/AAPG/SEG Unconventional Resources Technology Conference, 24-26 July, Austin, Texas, USA, URTEC-2670102-MS; 2017.

McClure, M., Babazadeh, M., Shiozawa, S., Huang, J., 2015. Fully Coupled Hydromechanical Simulation of Hydraulic Fracturing in Three-Dimensional Discrete Fracture Networks. Presented at the SPE Hydraulic Fracturing Technology Conference, Society of Petroleum Engineers. https://doi.org/10.2118/173354-MS

Mondal, S., Wu, C.-H., Sharma, M.M., 2016. Coupled CFD-DEM simulation of hydrodynamic bridging at constrictions. International Journal of Multiphase Flow 84, 245–263. https://doi.org/10.1016/j.ijmultiphaseflow.2016.05.001

Nasr-El-Din, H.A., Al-Anazi, H.A., Mohamed, S.K., 2000. Stimulation of Water-Disposal Wells Using Acid-in-Diesel Emulsions: Case Histories. SPE Production & Facilities 15, 176–182. https://doi.org/10.2118/65069-PA

Nordgren, R.P., 1972. Propagation of a Vertical Hydraulic Fracture. Society of Petroleum Engineers Journal 12, 306–314. https://doi.org/10.2118/3009-PA

Olson, J.E., Bahorich, B., Holder, J., 2012. Examining Hydraulic Fracture: Natural Fracture Interaction in Hydrostone Block Experiments. Presented at the SPE Hydraulic Fracturing Technology Conference, Society of Petroleum Engineers. https://doi.org/10.2118/152618-MS

Ouyang, L., Yango, T., Zhu, D., Hill, A.D., 2012. Theoretical and Experimental Modeling of Residual Gel Filter-Cake Displacement in Propped Fractures. SPE Production & Operations 27, 363–370. https://doi.org/10.2118/147692-PA

Palisch, T.T., Duenckel, R.J., Bazan, L.W., Heidt, J.H., Turk, G.A., 2007. Determining Realistic Fracture Conductivity and Understanding its Impact on Well Performance - Theory and Field Examples. Presented at the SPE Hydraulic Fracturing Technology Conference, Society of Petroleum Engineers. https://doi.org/10.2118/106301-MS

Panthi, K., Singh, R., Mohanty, K.K., 2017. Microencapsulation and Stimuli-Responsive Controlled Release of Particles Using Water-in-Air Powders. Langmuir 33, 3998–4010. https://doi.org/10.1021/acs.langmuir.7b00149

Patankar, N.A., Joseph, D.D., Wang, J., Barree, R.D., Conway, M., Asadi, M., 2002. Power law correlations for sediment transport in pressure driven channel flows. International Journal of Multiphase Flow 28, 1269–1292. https://doi.org/10.1016/S0301-9322(02)00030-7

Perkins, T.K., Kern, L.R., 1961. Widths of Hydraulic Fractures. Journal of Petroleum Technology 13, 937–949. https://doi.org/10.2118/89-PA

Pirker, S., Kahrimanovic, D., Kloss, C., Popoff, B., Braun, M., 2010. Simulating coarse particle conveying by a set of Eulerian, Lagrangian and hybrid particle models. Powder Technology 204, 203–213. https://doi.org/10.1016/j.powtec.2010.07.033

Raufaste, C., Dollet, B., Cox, S., Jiang, Y., Graner, F., 2007. Yield drag in a two-dimensional foam flow around a circular obstacle: Effect of liquid fraction. The European Physical Journal E 23, 217–228. https://doi.org/10.1140/epje/i2006-10178-9

Reidenbach, V.G., Harris, P.C., Lee, Y.N., Lord, D.L., 1986. Rheological Study of Foam Fracturing Fluids Using Nitrogen and Carbon Dioxide. SPE Production Engineering 1, 31–41. https://doi.org/10.2118/12026-PA

Ribeiro, L.H., Sharma, M.M., 2013. A New 3D Compositional Model for Hydraulic Fracturing With Energized Fluids. SPE Production & Operations 28, 259–267. https://doi.org/10.2118/159812-PA

Ribeiro, L.H., Sharma, M.M., 2012. Multiphase Fluid-Loss Properties and Return Permeability of Energized Fracturing Fluids. SPE Production & Operations 27, 265–277. https://doi.org/10.2118/139622-PA

Rickards, A.R., Brannon, H.D., Wood, W.D., 2006. High Strength, Ultralightweight Proppant Lends New Dimensions to Hydraulic Fracturing Applications. SPE Production & Operations 21, 212–221. https://doi.org/10.2118/84308-PA

Roy, D.M., Linnehan, S.K., 1974. Hydroxyapatite formed from Coral Skeletal Carbonate by Hydrothermal Exchange. Nature 247, 220–222. https://doi.org/10.1038/247220a0

Sahai, R., Miskimins, J.L., Olson, K.E., 2014. Laboratory results of proppant transport in complex fracture systems, in: SPE Hydraulic Fracturing Technology Conference, 23 - 25 Jan, The Woodlands, Texas, USA, SPE-168579-MS; 2014. Society of Petroleum Engineers.

Sassoni, E., Naidu, S., Scherer, G.W., 2011. The use of hydroxyapatite as a new inorganic consolidant for damaged carbonate stones. Journal of Cultural Heritage 12, 346–355. https://doi.org/10.1016/j.culher.2011.02.005

Schramm, L.L., 1994. Foam Sensitivity to Crude Oil in Porous Media, in: Foams: Fundamentals and Applications in the Petroleum Industry, Advances in Chemistry. American Chemical Society, pp. 165–197. https://doi.org/10.1021/ba-1994-0242.ch004

Shiozawa, S., McClure, M., 2016. Simulation of proppant transport with gravitational settling and fracture closure in a three-dimensional hydraulic fracturing simulator. Journal of Petroleum Science and Engineering 138, 298–314. https://doi.org/10.1016/j.petrol.2016.01.002

Singh, R., Mohanty, K.K., 2017. Foam flow in a layered, heterogeneous porous medium: A visualization study. Fuel 197, 58–69. https://doi.org/10.1016/j.fuel.2017.02.019

Singh, R., Mohanty, K.K., 2016. Foams with Wettability-Altering Capabilities for Oil-Wet Carbonates: A Synergistic Approach. SPE Journal 21, 1126–1139. https://doi.org/10.2118/175027-PA

Singh, R., Mohanty, K.K., 2015. Synergy between Nanoparticles and Surfactants in Stabilizing Foams for Oil Recovery. Energy Fuels 29, 467–479. https://doi.org/10.1021/ef5015007

Singh, R., Mohanty, K.K., 2014. Synergistic Stabilization of Foams by a Mixture of Nanoparticles and Surfactants, in: SPE Improved Oil Recovery Symposium. Society of Petroleum Engineers. https://doi.org/10.2118/169126-MS

Singh, R., Panthi, K., Mohanty, K.K., 2017. Microencapsulation of Acids by Nanoparticles for Acid Treatment of Shales. Energy Fuels 31, 11755–11764. https://doi.org/10.1021/acs.energyfuels.7b02003

Singh, R., Tong, S., Panthi, K., Mohanty, K., 2018. Nanoparticle-Encapsulated Acids for Stimulation of Calcite-Rich Shales, in: Unconventional Resources Technology Conference, Houston, Texas, 23-25 July 2018. Society of Petroleum Engineers, pp. 1464–1478. https://doi.org/10.15530/urtec-2018-2897114

Sivakumar, M., Kumar, T.S.S., Shantha, K.L., Rao, K.P., 1996. Development of hydroxyapatite derived from Indian coral. Biomaterials 17, 1709–1714. https://doi.org/10.1016/0142-9612(96)87651-4

Snider, D.M., 2001. An Incompressible Three-Dimensional Multiphase Particle-in-Cell Model for Dense Particle Flows. Journal of Computational Physics 170, 523–549. https://doi.org/10.1006/jcph.2001.6747

Sun, Z., Espinoza, D.N., Balhoff, M.T., 2016. Discrete element modeling of indentation tests to investigate mechanisms of CO2-related chemomechanical rock alteration. J. Geophys. Res. Solid Earth 121, 2016JB013554. https://doi.org/10.1002/2016JB013554

Taylor, K.C., Nasr-El-Din, H.A., 2003. Laboratory Evaluation of In-Situ Gelled Acids for Carbonate Reservoirs. SPE Journal 8, 426–434. https://doi.org/10.2118/87331-PA

Tomac, I., Gutierrez, M., 2013. Numerical Study of Horizontal Proppant Flow and Transport in a Narrow Hydraulic Fracture. Presented at the 47th U.S. Rock Mechanics/Geomechanics Symposium, American Rock Mechanics Association.

Tong, S., Gu, M., Singh, R., Mohanty, K., 2018. Simulation of Proppant Transport in Foam Fracturing Fluid Based on Experimental Results, in: Unconventional Resources Technology Conference, Houston, Texas, 23-25 July 2018, Society of Petroleum Engineers, pp. 4064–4080. https://doi.org/10.15530/urtec-2018-2901054

Tong, S., Mohanty, K., 2017. Proppant Placement in Secondary Fractures, in: SPE/AAPG/SEG Unconventional Resources Technology Conference, 24-26 July, Austin, Texas, USA, URTEC-2671549-MS; 2017.

Tong, S., Mohanty, K.K., 2016. Proppant transport study in fractures with intersections. Fuel 181, 463–477.

Tong, S, Singh, R., Mohanty, K.K., 2018. A visualization study of proppant transport in foam fracturing fluids. Journal of Natural Gas Science and Engineering 52, 235–247. https://doi.org/10.1016/j.jngse.2018.01.030

Tong, S., Singh, R., Mohanty, K.K., 2017. Proppant Transport in Fractures with Foam-Based Fracturing Fluids, in: SPE Annual Technical Conference and Exhibition, 9 - 11 Oct, San Antonio, Texas, USA, SPE-187376-MS; 2017. Society of Petroleum Engineers. https://doi.org/10.2118/187376-MS

Tripathi, D., Pournik, M., 2014. Effect of Acid on Productivity of Fractured Shale Reservoirs. Presented at the Unconventional Resources Technology Conference, Unconventional Resources Technology Conference. https://doi.org/10.15530/URTEC-2014-1922960

Tsai, K., Fonseca, E., Degaleesan, S., Lake, E., 2013. Advanced Computational Modeling of Proppant Settling in Water Fractures for Shale Gas Production. SPE Journal 7.

Vecchio, K.S., Zhang, X., Massie, J.B., Wang, M., Kim, C.W., 2007. Conversion of bulk seashells to biocompatible hydroxyapatite for bone implants. Acta Biomaterialia 3, 910–918. https://doi.org/10.1016/j.actbio.2007.06.003

Verbist, G., Weaire, D., Kraynik, A.M., 1996. The foam drainage equation. J. Phys.: Condens. Matter 8, 3715. https://doi.org/10.1088/0953-8984/8/21/002

Vikingstad, A.K., Skauge, A., Høiland, H., Aarra, M., 2005. Foam–oil interactions analyzed by static foam tests. Colloids and Surfaces A: Physicochemical and Engineering Aspects 260, 189–198.

Voorhees, P.W., 1985. The theory of Ostwald ripening. J Stat Phys 38, 231–252. https://doi.org/10.1007/BF01017860

Wang, J., Joseph, D.D., Patankar, N.A., Conway, M., Barree, R.D., 2003. Bi-power law correlations for sediment transport in pressure driven channel flows. International Journal of Multiphase Flow 29, 475–494. https://doi.org/10.1016/S0301-9322(02)00152-0

Wanniarachchi, W. a. M., Ranjith, P.G., Perera, M.S.A., Lashin, A., Arifi, N.A., Li, J.C., 2015. Current opinions on foam-based hydro-fracturing in deep geological reservoirs. Geomech. Geophys. Geo-energ. Geo-resour. 1, 121–134. https://doi.org/10.1007/s40948-015-0015-x

Warpinski, N.R., 2009. Stress Amplification and Arch Dimensions In Proppant Beds Deposited by Waterfracs. Presented at the SPE Hydraulic Fracturing Technology Conference, Society of Petroleum Engineers. https://doi.org/10.2118/119350-MS

Warpinski, N.R., Mayerhofer, M.J., Vincent, M.C., Cipolla, C.L., Lolon, E.P., 2009. Stimulating unconventional reservoirs: maximizing network growth while optimizing fracture conductivity. Journal of Canadian Petroleum Technology 48, 39–51.

Weaire D., Hutzler S., Verbist G., Peters E., 2007. A Review of Foam Drainage. Advances in Chemical Physics. https://doi.org/10.1002/9780470141618.ch5

Wei, W., Varavei, A., Sepehrnoori, K., 2017. Modeling and Analysis on the Effect of Two-Phase Flow on Wormhole Propagation in Carbonate Acidizing. SPE Journal 22, 2,067-2,083. https://doi.org/10.2118/186111-PA

Weng, X., Kresse, O., Cohen, C.E., Wu, R., Gu, H., 2011. Modeling of Hydraulic Fracture Network Propagation in a Naturally Fractured Formation. Presented at the SPE Hydraulic Fracturing Technology Conference, Society of Petroleum Engineers. https://doi.org/10.2118/140253-MS

Woodworth, T.R., Miskimins, J.L., 2007. Extrapolation of Laboratory Proppant Placement Behavior to the Field in Slickwater Fracturing Applications, in: SPE Hydraulic Fracturing Technology Conference. 29-31 Jan, College Station, Texas, USA, SPE-106089-MS. https://doi.org/10.2118/106089-MS

Wu, K., Olson, J.E., 2015. Simultaneous Multifracture Treatments: Fully Coupled Fluid Flow and Fracture Mechanics for Horizontal Wells. SPE Journal 20, 337–346. https://doi.org/10.2118/167626-PA

Wu, W., Sharma, M.M., 2017a. Acid Fracturing in Shales: Effect of Dilute Acid on Properties and Pore Structure of Shale. SPE Production & Operations 32, 51–63. https://doi.org/10.2118/173390-PA

Wu, W., Sharma, M.M., 2017b. A Model for the Conductivity and Compliance of Unpropped and Natural Fractures. SPE Journal 22, 1,893-1,914. https://doi.org/10.2118/184852-PA

Xu, B., Hill, A.D., Zhu, D., Wang, L., 2011. Experimental Evaluation of Guar-Fracture-Fluid Filter-Cake Behavior. SPE Production & Operations 26, 381–387. https://doi.org/10.2118/140686-PA

Xu, K., Zhu, P., Colon, T., Huh, C., Balhoff, M., 2016. A Microfluidic Investigation of the Synergistic Effect of Nanoparticles and Surfactants in Macro-Emulsion-Based Enhanced Oil Recovery. SPE Journal.

Yang, H., Balhoff, M.T., 2017. Pore-network modeling of particle retention in porous media. AIChE J. 63, 3118–3131. https://doi.org/10.1002/aic.15593

Yekeen, N., Padmanabhan, E., Idris, A.K., 2018. A review of recent advances in foam-based fracturing fluid application in unconventional reservoirs. Journal of Industrial and Engineering Chemistry 66, 45–71. https://doi.org/10.1016/j.jiec.2018.05.039

Yoshimura, M., Sujaridworakun, P., Koh, F., Fujiwara, T., Pongkao, D., Ahniyaz, A., 2004. Hydrothermal conversion of calcite crystals to hydroxyapatite. Materials Science and Engineering: C 24, 521–525. https://doi.org/10.1016/j.msec.2004.01.005

Zeng, J., Li, H., Zhang, D., 2019. Numerical simulation of proppant transport in propagating fractures with the multi-phase particle-in-cell method. Fuel 245, 316–335. https://doi.org/10.1016/j.fuel.2019.02.056

Zhang, J., Dunn-Norman, S., 2015. Computational Fluid Dynamics (CFD) Modeling of Proppant Transport in a Plug and Perf Completion with Different Perforation Phasing, in: Unconventional Resources Technology Conference, San Antonio, Texas, 20-22 July 2015. pp. 1561–1574. https://doi.org/10.15530/urtec-2015-2169184

Zhang, J., Kamenov, A., Hill, A.D., Zhu, D., 2014. Laboratory Measurement of Hydraulic-Fracture Conductivities in the Barnett Shale. SPE Production & Operations 29, 216–227. https://doi.org/10.2118/163839-PA

Zhou, J., Carman, P., Sun, H., Wheeler, R., Brannon, H., Gupta, D.V.S., Starks, R., 2015. Superior Proppant Placement and Fracture Conductivity by Soft Particle Fracturing

Fluid, in: SPE Production and Operations Symposium. 1-5 Mar, Oklahoma City, Oklahoma, USA, SPE-173621. https://doi.org/10.2118/173621-MS